

Stratospheric chemical-dynamical ensemble data assimilation

Thomas Milewski

Doctor of Philosophy

Department of Atmospheric and Oceanic Sciences

McGill University

Montréal, Québec

June 2012

A thesis submitted to McGill University in partial fulfillment of the requirements
for the degree of Doctor of Philosophy

©Thomas Milewski 2012

DEDICATION

Je voudrais dédier cette thèse à tous ceux qui, au long des années, ont su stimuler mon intérêt pour la science et le monde. En particulier mes parents, grand-parents, oncles et tantes qui ont su chacun à leur manière planter en moi avec amour et attention ces graines qui m'ont mené jusqu'ici. Je vous en suis éternellement reconnaissant. J'espère pouvoir à mon tour être une telle source d'inspiration pour mes enfants Alicja et Nathaniel.

ACKNOWLEDGEMENTS

My sincere gratitude goes to my thesis supervisor, Michel Bourqui, for introducing me to this fascinating research project that combines so elegantly stratospheric dynamics and chemistry, numerical methods and ensemble data assimilation. I greatly appreciate the given opportunity to investigate unexplored scientific grounds with a fully functional and adapted apparatus: the IGCM-FASTOC chemistry-climate model. Along the years, Michel Bourqui has offered the necessary latitude for me to conduct this research at a pace optimal for thorough investigation and understanding of the system in hand, and I thank him for that. His guidance was instrumental in the smooth evolution of this study and his points of view always insightful. His scientific vision and rigor were precious examples for me.

I wish to acknowledge the impact that the participants in the C-SPARC and SPARC-DA community have had on my growing interest and understanding of stratospheric dynamics, chemistry and data assimilation. It has been a pleasure to discuss periodically with Saroja Polavarapu, Richard Ménard, Jean de Grandpré, Simon Chabrilat, Kazuyuki Miyazaki, to name a few. My years at McGill University would not have been so pleasant and fruitful without the friendships. Great moments with my Katabatikillerz hockey fellows Louis-Philippe, Jean-Francois and Jan, as well as Stratospheric Dynamics and Chemistry Group doctorate colleagues Barbara and Farid. Peter Houtekamer, Herschel Mitchell and William Sacher have also provided helpful hints in the initial steps of my research.

I also want to express my gratefulness to my wife Karolina for her love and support. Even through the difficult juggling between parenthood and doctoral studies, she has always responded with encouragement. Karolina is an everyday source of energy for me and has the incredible aptness to keep me focused.

On a lighter note, I would like to thank Hydroxyl, Methane, Bumblebee and Twister for not letting me down too often. And when they did let me down, Michael Havas was always there to operate his magic and mysteriously solve any computer problem almost instantly. I would also like to thank Ornella Cavaliere for bureaucratic help, advice and directions.

Last and not least, I would like to thank William Lahoz (external examiner), Yi Huang (internal examiner) and Yves Rochon (external defense committee member) for having willingly accepted to evaluate this thesis and for the enriching comments.

ABSTRACT

Ensemble data assimilation uses Monte-Carlo methods to estimate flow-dependent error covariances which allow the transfer of information from observed variables to correlated ones. As the winds are largely unobserved in the stratosphere and models have biases there, the possibility to constrain the dynamical analysis from temperature or ozone observations is attempted using ensemble data assimilation.

The applicability of coupled chemical/dynamical ensemble data assimilation in the stratosphere is tested in idealized perfect model observation system simulation experiments with the IGCM-FASTOC chemistry-climate model. Covariance localization is found to be necessary for stability of the Ensemble Kalman Filter (EnKF) data assimilation system and optimal localization parameters yield a strong constraint on the global dynamical state of the model when assimilating synthetic limb-sounding stratospheric temperature or ozone observations only. The multivariate coupling between ozone, temperature and winds is investigated in the optimized EnKF system. Stratospheric temperature and ozone observations induce valuable dynamical analysis increments during the analysis step. There is additional feedback during the forecast steps in the ensemble data assimilation system, further constraining the global dynamical and ozone states.

The potential impact of assimilating observations posterior to analysis time in multivariate mode was estimated with an Ensemble Kalman Smoother (EnKS). Assimilation of additional asynchronous observations up to 48 hours posterior to

analysis time provided improvements on the EnKF analysis nearly similar to the ones obtained from the assimilation of a same amount of additional synchronous observations. The EnKS assimilation showed beneficial impacts on the unobserved variables analysis state but mixed impacts on the observed variable analysis state.

The capacity to constrain the unobserved stratospheric winds by assimilating ozone observations is demonstrated in the ensemble data assimilation system with the EnKF and EnKS. The chemical-dynamical error covariances are critical to reduce the wind error in the model analysis state particularly through the ozone-wind covariances effective in the upper-troposphere lower-stratosphere region. Additional tests with strongly-biased initial forecasts, within a stratospheric sudden warming experiment, confirm the ability of the EnKF to efficiently propagate information from ozone observations to the dynamical model state.

ABRÉGÉ

L'assimilation d'ensemble utilise une méthode de Monte-Carlo pour estimer les covariances d'erreur du moment qui permettent le transfert d'information des variables observées aux variables corrélées à celles-ci. Puisque les vents sont très peu observés dans la stratosphère et que les modèles y présentent des biais, la possibilité de contraindre l'état dynamique du modèle par l'assimilation d'observations de température et d'ozone par la technique d'ensemble est tentée.

L'applicabilité de l'assimilation d'ensemble dans un système chimique/dynamique couplé est testé lors d'une expérience idéalisée (modèle parfait) de simulation de système d'observation avec le modèle de chimie-climat IGCM-FASTOC. La localisation des covariances est indispensable à la stabilité du système d'assimilation avec filtre de Kalman d'ensemble (EnKF) et les paramètres optimaux offrent une forte contrainte sur l'état dynamique global du modèle lorsque l'on assimile des observations satellites synthétiques de température et d'ozone stratosphériques uniquement. Le couplage entre l'ozone, la température et les vents est étudié dans le système EnKF optimisé. Les observations de température et d'ozone stratosphériques créent des incréments dynamiques bénéfiques lors des phases d'analyses. Il y a également une rétroaction lors de la phase de prédiction du système d'assimilation de données, qui aide à contraindre davantage les états chimiques et dynamiques globaux.

L'impact potentiel de l'assimilation de données postérieures au temps d'analyse en mode multivarié est estimé avec un lisseur d'ensemble de Kalman

(EnKS). L'assimilation d'observations additionnelles asynchrones, ayant jusqu'à 48 heures d'écart avec le temps d'analyse, offre des améliorations aux analyses de l'EnKF presque équivalentes à celles obtenues par assimilation d'une quantité égale d'observations additionnelles synchrones. L'EnKS présente des impacts bénéfiques sur l'état d'analyse des variables non observées mais des impacts mitigés sur l'état analysé des variables observées.

La capacité de contraindre les vents stratosphériques non-observés grâce à l'assimilation d'observations d'ozone est démontrée dans le système d'assimilation d'ensemble avec l'EnKF et l'EnKS. Les covariances d'erreurs chimiques-dynamiques sont essentielles à la réduction de l'erreur de vents dans l'état analysé du modèle, en particulier les covariances ozone-vent qui font effet dans la haute troposphère et basse stratosphère. Des expériences additionnelles avec un état initial fortement biaisé, en l'occurrence un réchauffement stratosphérique soudain, confirment l'abilité de l'EnKF à transférer de façon efficace l'information depuis les observations d'ozone vers l'état dynamique du modèle.

CONTRIBUTIONS OF AUTHORS

My thesis supervisor Professor Michel Bourqui has provided the initial research project idea of attempting ensemble data assimilation on a chemistry-climate model. He also supplied the source code for the IGCM-FASTOC chemistry climate model jointly developed at the University of Reading and at McGill, as well as scripts for launching model simulations and for post-processing of the model data. The rest of the research was conducted by myself. This includes the numerical coding of the Ensemble Kalman Filter based on available scientific literature and the development of ensemble diagnostics. Topics for the three papers are based on my own ideas. Frequent discussions with Prof. Bourqui have helped shape the study and his comments and editing of the manuscripts have been valuable inputs. All three manuscripts in this doctoral thesis have been written by myself, with Prof. Michel Bourqui as co-author. The first manuscript, included entirely in Chapter 2, has been accepted and published in *Monthly Weather Review* following minor corrections based on comments from three anonymous reviewers. Dr. Saroja Polavarapu also reviewed the initial version of the manuscript and provided helpful comments. The second manuscript was edited by Prof. Bourqui and has been submitted to *Tellus A* in April 2012. The third manuscript is in its preliminary form as it has not been edited by Prof. Bourqui as of yet.

TABLE OF CONTENTS

DEDICATION	ii
ACKNOWLEDGEMENTS	iii
ABSTRACT	v
ABRÉGÉ	vii
CONTRIBUTIONS OF AUTHORS	ix
LIST OF TABLES	xiii
LIST OF FIGURES	xiv
1	Introduction	1
	1.1 Representing of the Stratosphere	3
	1.1.1 Basic Phenomena	3
	1.1.2 Observing the Stratosphere	9
	1.1.3 Modeling the Stratosphere: Chemistry Climate Models	12
	1.1.4 The Stratosphere in Global NWP Forecasts and Reanalyses	16
	1.2 Stratospheric Data Assimilation	20
	1.2.1 Data Assimilation Basics	20
	1.2.2 Ensemble Kalman Filter	28
	1.2.3 Stratospheric Applications	46
	1.3 Methodology and Aim of Thesis	54
	1.3.1 IGCM-FASTOC Model	54
	1.3.2 EnKF Filter Configurations	57
	1.3.3 Aim of the Thesis	58
2	Assimilation of Stratospheric Temperature and Ozone with an Ensemble Kalman Filter in a Chemistry-Climate Model	63
	2.1 Introduction	66

2.2	A Short Review of Ensemble Kalman Filtering	71
2.3	Experimental Setup and Diagnostics	76
2.3.1	Experimental Setup	76
2.3.2	EnKF Parameters	79
2.3.3	Diagnostics	81
2.4	Sensitivity Studies	84
2.4.1	Assimilation of Temperature	85
2.4.2	Assimilation of Ozone	90
2.5	Multivariate Covariances	91
2.5.1	Temperature Assimilation	93
2.5.2	Ozone Assimilation	96
2.5.3	Ozone-Dynamical Covariances	99
2.6	Conclusion	100
3	Potential of an Ensemble Kalman Smoother for Stratospheric Chemical- Dynamical Data Assimilation	105
3.1	Introduction	108
3.2	The Ensemble Kalman Smoother	112
3.3	Experimental Setup	114
3.3.1	Assimilation Setup	114
3.3.2	Experiments	116
3.3.3	Initial Conditions	117
3.4	Assimilation Impact on Analyses	121
3.4.1	Synchronous Assimilation Impact	121
3.4.2	Time-lagged Assimilation Impact	124
3.4.3	Ensemble Kalman Smoother Assimilation Impact	127
3.5	Conclusions	135
4	Constraining a Stratospheric Sudden Warming with Ensemble Kalman Filter Ozone assimilation	139
4.1	Introduction	141
4.2	Self-generated Stratospheric Sudden Warming Event	145
4.3	Ozone Assimilation	148
4.3.1	Assimilation Starting Prior to Wind-reversal Time	149
4.3.2	Assimilation Starting at Wind-reversal Time	151
4.4	Conclusion	152
5	Conclusions	154

Appendix A: Kalman Filter and Extended Kalman Filter Equations	164
Appendix B: Sparse Matrix Treatment	171
Appendix C: Index of Vectors and Parameters	173

LIST OF TABLES

<u>Table</u>	<u>page</u>
1-1 Table of the main operational NWP models, reanalyses and ensemble prediction systems with their resolutions and data assimilation schemes.	17
2-1 Results with assimilation of temperature: (top left) time-averaged α (in %), (bottom left) β (in %), (top right) SPREAD (in m s^{-1}) and (bottom right) RMSE (in m s^{-1}) diagnostics applied on TE, with corresponding 1σ uncertainty, for the various horizontal and vertical localization decorrelation lengths. Time averages and standard deviations are calculated over the last 45 days of assimilation. Minimum absolute values for the different diagnostics are highlighted in bold.	89
2-2 Results with assimilation of ozone: (top left) time-averaged α (in %), (bottom left) β (in %), (top right) SPREAD (in m s^{-1}) and (bottom right) RMSE (in m s^{-1}) diagnostics applied on TE, with corresponding $1\text{-}\sigma$ uncertainty, for the various horizontal and vertical localization decorrelation lengths. Time averages and standard deviations are calculated over the last 45 days of assimilation. Minimum absolute values for the different diagnostics are highlighted in bold.	90

LIST OF FIGURES

<u>Figure</u>	<u>page</u>
1-1 Schematic of upward-propagating waves (orange wiggly arrows) and the Brewer-Dobson circulation (black arrows) superposed on March 2004 OSIRIS ozone number density observations. Tropopause is indicated with the dashed black line. Figure taken from Shaw and Shepherd (2008).	4
1-2 Latitude-pressure plot of methane (CH ₄) concentrations. Figure taken from the website: http://www.ccpo.odu.edu/lizsmith/SEES/ozone/class/Chap_6/6 Js/6-04a.jpg	4
1-3 Vertical temperature bias relative to ERA-40 reanalyses for 13 chemistry-climate models. Figure from Eyring et al. (2006).	15
1-4 The top figure shows the initial bimodal background PDF (black line) and the 5000 ensemble members populating it (gray histogram). The second row shows the three observation scenarios. The last two rows show respectively the stochastic and deterministic filter ensemble updates (gray histogram) and the Bayes' rule expected PDF (black lines). Figures 1(b) and 3 of Lawson and Hansen (2004).	33
1-5 Analysis, background and observation distributions in 2D space for (a) a control state, and two special cases of (b) insufficient variance and (c) overestimated covariances. Figure 3 of Hamill et al. (2001).	37
1-6 Double Ensemble Kalman filter assimilation scheme where one ensemble is updated using the statistics obtained from another. Figure 2 of Houtekamer and Mitchell (1998).	40

1–7	Vertical temperature error covariances with respect to the reference grid point at 0°E, 60°N and 30 km altitude with three levels of localization : an unlocalized case (red), a weakly-localized case where vertical decorrelation is set at 10 scale heights (green) and a severely-localized case where vertical decorrelation is set at 2 scale heights (blue). Covariances sampled from the IGCM-FASTOC model.	42
1–8	Horizontal temperature covariance surface map with respect to the same reference grid point as in Fig 1–7 for an unlocalized case (top figure) and a severely-localized case with horizontal decorrelation set at 2800 km (bottom figure). Covariances sampled from the IGCM-FASTOC model.	42
2–1	RMSE (solid lines) and SPREAD (dashed lines) of the square root of the TE norm (m s^{-1}) for the temperature assimilation scenarios with (a) fixed $C_h = 2800$ km and varying C_v and (b) fixed $C_v = 2$ and varying C_h	85
2–2	Evolution of the \mathbf{P}_e^f and $\tilde{\mathbf{R}}$ discrepancy coefficients α (solid line, in %) and β (dotted line, in %) for the temperature assimilation scenarios with (a) fixed $C_h = 2800$ km and varying C_v and (b) fixed $C_v = 2$ and varying C_h	88
2–3	Results with assimilation of temperature: time-averaged RMSE (solid lines) and SPREAD (dashed lines) by σ levels, for (a) temperature (K), (b) ozone relative to true state (% of true value), (c) zonal wind speed (m s^{-1}), and (d) specific humidity(g kg^{-1}). Black curves represent climatology, blue curves the Control temperature assimilation and red curves the NoChem temperature assimilation (i.e., without dynamical-chemical covariances). For reference, the temperature observation error is shown in (a) as a green dotted line, and the vertical range of the observations by the thin horizontal dotted lines in (a)-(d). The vertical axis is the log-sigma approximate height (km). Time averages are performed over the last 45 days of assimilation.	94

2–4	Same as Fig. 2–3 except that blue curves are results from the Control ozone assimilation and the red curves are for the NoDyn ozone assimilation (without chemical-dynamical covariances). (b) For reference, the ozone observation error is shown as a green dotted line.	97
2–5	Schematic describing the information flow between variables during a data assimilation cycle, for our (top) temperature assimilation experiments and (bottom) ozone assimilation experiments. Curved arrows show the effect of cross covariances. Straight vertical arrows embedded in the “Forecast” box show the effect of model balancing. Note that ozone (O_x , blue arrows) can only affect the temperature (T, red arrows) and winds (u, green arrows) during the ozone assimilation, as observed in Section 2.5.	98
2–6	Time-averaged, σ -level-averaged RMSE (solid lines) and SPREAD (dashed lines) of (a) zonal wind speed ($m s^{-1}$) and (b) temperature (K) for various scenarios of ozone assimilation. Black curves represent the climatological ensemble, blue curves are the Control ozone assimilation experiment, pink curves and green curves are the NoWinds and NoTemp ozone assimilation experiments where ozone-winds or ozone-temperature covariances have been switched off, respectively. The vertical axis is the log-sigma approximate height (km). Time averages are performed over the last 45 days of assimilation.	100
3–1	Time evolution of the root-mean-square error (RMSE, solid line) and ensemble spread (SPREAD, dashed line) of the square root of the total energy norm ($m.s^{-1}$). Black lines: climatological ensemble; blue lines: ozone assimilation cycle; red lines: temperature assimilation cycle. Horizontal and vertical localization length parameters (C_h and C_v) are given in the legend.	118
3–2	10-day time-averaged zonal-mean forecast root-mean-square error (RMSE) for (top row) zonal wind ($m.s^{-1}$), (middle row) temperature (K) and (bottom row) ozone (ppmv). Left and right columns show forecast RMSE from the CONTROL MIPAS temperature and ozone assimilation experiments, respectively.	119

3–3	20-day-average analysis-minus-forecast RMSE changes (in %) for (left column) EnKF MIPAS temperature assimilation and (right column) EnKF MIPAS ozone assimilation. Top row: zonal-mean zonal wind; middle row: zonal-mean temperature; bottom row: zonal-mean ozone. Zero-line of RMSE changes contoured with solid black line.	122
3–4	30-day average of zonal-mean zonal wind analysis-minus-forecast RMSE changes (in %) for MIPAS ozone assimilation with (top row) an EnKF (middle row) an EnKS with 24-hour lag between observation and analysis time and (bottom row) an EnKS with 48-hour lag. Left and right columns show forecast RMSE from the CONTROL MIPAS temperature and ozone assimilation experiments, respectively.	125
3–5	Zonal-mean zonal wind Δ RMSE difference (in %) between the EnKS MIPAS and the EnKF MIPAS (top row) and between the EnKF 3 \times MIPAS and the EnKF MIPAS (bottom row) for temperature assimilation (left column) and ozone assimilation (right column). Purple (orange) colors indicate improvement (degradation) of the EnKS MIPAS or EnKF 3 \times MIPAS over the EnKF MIPAS. Statistically significant differences at the 95% confidence level are enclosed by the black lines.	129
3–6	Same as Figure 3–5 but for the zonal-mean temperature Δ RMSE differences	132
3–7	Same as Figure 3–5 but for the zonal-mean ozone mixing ratio Δ RMSE differences	133
4–1	Time evolution of the 12-hPa zonal-mean (a) zonal wind at 58°N and (b) polar cap temperature (area-averaged from 50 to 85°N) for the 128 climatological ensemble members (grey curves) and the stratospheric sudden warming true state (red curve). The zero-wind line is in green in panel (a).	145
4–2	Evolution of the 10-hPa geopotential height field for the stratospheric sudden warming case in polar stereographic view between 30 and 90°N. Latitudes circles are marked in green every 10° starting from 30°N. Geopotential height contours intervals are set to 200m. . . .	147

4-3	Same as Fig. 4-1 but for the ensemble of zonal-mean (a) zonal wind and (b) polar cap temperature analyses from the Ensemble Kalman Filter daily assimilation of synthetic MIPAS ozone retrieval starting on day 1.	149
4-4	Latitude-height cross-section of the climatological ensemble ozone deviation with respect to the true state (a) prior to stratospheric sudden warming (day 1) and (b) at time of Polar Vortex wind reversal (day 21), normalized by the climatological ensemble spread (in standard deviations).	150
4-5	Same as Fig. 4-1 but for the ensemble of zonal-mean (a) zonal wind and (b) polar cap temperature analyses from the Ensemble Kalman Filter daily assimilation of synthetic MIPAS ozone retrieval starting on day 21.	152

CHAPTER 1 Introduction

[...] *dévorant tout, le manque de méthode rendait l'assimilation très lente, une telle confusion se produisait, qu'il finissait par savoir des choses qu'il n'avait pas comprises.*

Emile Zola, *Germinal*

The geophysical properties of the stratosphere can metaphorically represent its historical importance and evolution in atmospheric research. The vertical distance from the surface and low air density have tended, at first, to put it far and away from the mind of atmospheric researchers. Its radiant power has nonetheless fascinated the brilliant minds of a minority of atmospheric dynamicists, physicists and chemists altogether, fueling a lot of scientific questions and debates over the last 50 years. Since then, thanks to the clairvoyance of a few, the stratosphere has gained important recognition as an influence on the tropospheric dynamics. The atmospheric operational centers have now caught the wave and joined forces in dealing with remaining problems in stratospheric modeling, observation and obtention of a reliable estimate of the its state.

It is essential to pinpoint the main forces and phenomena driving the stratospheric system to see how well they are represented in models. It will help us understand the various timescales on which the stratosphere evolves and show the progression of stratospheric research efforts from a climatic long-term perspective to an increasing participation in short-term Numerical Weather Prediction (NWP) products. Notwithstanding the improvements that have been achieved in the last decades on climate models focusing on the stratosphere [i.e., Chemistry-Climate Models (CCM)], an optimization of stratospheric representation on short timescales requires the assimilation of observations. Accordingly, the main focus of this doctoral thesis is the constraining the model state with stratospheric observations using a contemporary data assimilation (DA) technique that exploits well the properties of the flow. In that respect, it is important to reconcile how long large-scale dynamical mechanisms affect the flow characteristics on scales relevant to the NWP analysis problem to be able to understand how variables, chemical or dynamical, influence each other.

The data assimilation concept and properties need to be overviewed to motivate our choice of a stochastic Ensemble Kalman Filter (EnKF) as system estimator in this study. This choice is particularly sensitive to the relatively low amount of observations available in the stratosphere. It is in fact a unique first attempt to apply ensemble data assimilation to a stratospheric coupled chemistry-dynamics model. This experiment needs to be situated with respect to other stratospheric data assimilation systems to determine the potential improvements or inherent dangers. The setup used in the investigation is obviously central to its

success or failure, and the appropriate bounds within which it operates need to be properly defined.

1.1 Representing of the Stratosphere

1.1.1 Basic Phenomena

The stratosphere is situated above the tropopause, roughly between 10 km and 50 km above Earth's surface (corresponding to atmospheric pressures between 200 hPa and 1 hPa approximatively). From its high altitude, one might intuitively expect the stratospheric dynamics to be driven from above by the strong incoming solar radiation. However, the radiative heating from ultraviolet (UV) absorption by ozone instead induces staticity, not dynamism, to the stratosphere. The 1930 Chapman model describes how the high-energy solar rays destroy the oxygen molecule (O_2) into a pair of oxygen atoms (O), each combining with an oxygen molecule to form ozone (O_3) (Jacob, 1999). Ozone in turn absorbs lower-energy UV solar rays, warming the stratosphere and inducing a negative temperature lapse rate (increase of temperature with height). The resulting stable stratification in the stratosphere damps vertical motion through convection and promotes a temperature state close to radiative equilibrium (A good overview of the radiative properties and vertical structure of the stratosphere is given in the book by Andrews et al., 1987).

Interestingly, observations show high concentrations of ozone in the polar winter hemisphere, far from the tropical source region which exhibits relatively low concentrations (see Fig. 1–1), indicating tropic-to-pole transport. The conceptual model for this transport has been proposed by Brewer (1949) from an initial idea

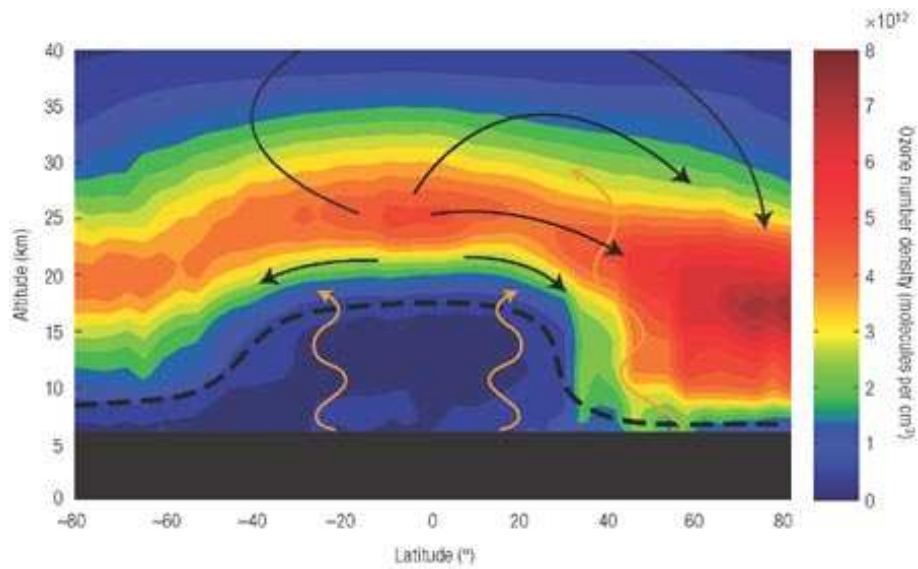


Figure 1-1: Schematic of upward-propagating waves (orange wiggly arrows) and the Brewer-Dobson circulation (black arrows) superposed on March 2004 OSIRIS ozone number density observations. Tropopause is indicated with the dashed black line. Figure taken from Shaw and Shepherd (2008).

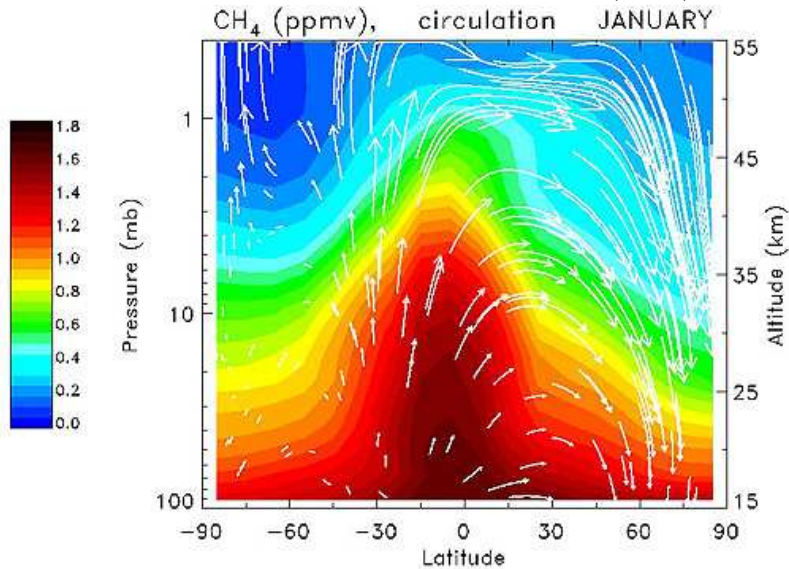


Figure 1-2: Latitude-pressure plot of methane (CH_4) concentrations. Figure taken from the website: http://www.ccpo.odu.edu/liz-smith/SEES/ozone/class/Chap_6/6-Js/6-04a.jpg.

by Dobson et al. (1929) and describes the slow meridional overturning circulation transporting chemical tracers, including ozone, from the tropics to the winter pole. It was only in the late 1970's that this picture was verified by Andrews and McIntyre (1976) with their “transformed Eulerian mean” framework where a slow residual circulation happening on monthly to yearly timescales appeared, otherwise invisible in conventional Eulerian averaging.

The driving mechanism for this Brewer-Dobson (B–D) circulation indicates that stratospheric dynamics are actually powered from the troposphere below. Large-scale westward planetary Rossby waves are allowed to permeate through the tropopause in the presence of a slow, westerly background flow (criterion defined by Charney and Drazin, 1961). As planetary Rossby waves are mostly generated in the troposphere by orography and land-sea thermal contrast, they are much more present in the Northern Hemisphere than the Southern Hemisphere. These waves propagate upwards and eventually break (schematized by the orange wiggly arrow at 50°N in Figure 1–1), depositing their westward momentum (Shepherd, 2000). To conserve angular momentum, tropical air masses are transported upward in the stratosphere, towards the poles and downward (black arrows in Figure 1–1).

The deposition of momentum as the waves break also produces a large midlatitude region of quasi-isentropic mixing and chaotic advection: the *Surf Zone* (McIntyre and Palmer, 1984). Its northern limit is defined by the *Polar Vortex*, this cold winter air mass formed by radiative cooling, which sustains strong westerly flow through thermal-wind balance. The Polar Vortex air mass is isolated from the Surf Zone by this zonal flow, but it can be weakened both by

the adiabatic warming of the downward branch of the B–D circulation and the westward momentum deposition from planetary waves. In special cases where the westward momentum deposition is anomalously strong and poleward, it may further decelerate the Polar Vortex zonal flow and stratospheric sudden warmings (SSW) may be witnessed (Matsuno, 1971). SSWs are rapid breakdowns of the polar vortex, where the cold temperature air mass is either displaced from the pole or split in two (Charlton and Polvani, 2007). In major events, the pole has a rapid increase in temperature over the course of a few days and reversal of the mid-stratospheric (10 hPa) Polar Vortex zonal winds from westerlies to easterlies is witnessed. Arctic SSWs occur on average six times per decade, while only a single Antarctic SSW has been witnessed, in 2002 (Roscoe et al., 2005). These are the most intense dynamical events in the stratosphere, with repercussions on the tropospheric weather on daily and weekly timescales (Charlton et al., 2005).

Another example of wave-mean flow interaction appears in the tropics as eastward Kelvin waves can also propagate upward into the tropical stratosphere. The well-mixed upwelling tropospheric air is strongly isolated from the subtropical Surf Zone air mass and forms the *Tropical Pipe* (Plumb, 1996) air mass located between 30°S and 30°N. Within the Tropical Pipe, Kelvin waves in conjunction with westward Rossby-gravity waves and small-scale internal gravity waves are responsible for the quasi-biennial oscillation (QBO). This oscillation manifests itself in the tropical zonal winds switching from westerlies to easterlies on an average period of 28 months (Baldwin et al., 2001). The (easterly or westerly) phase of the QBO influences the latitude at which planetary waves are allowed to propagate

upwards into the stratosphere and therefore modulates the strength of the Polar Vortex.

Wave-mean flow interaction and radiation are responsible for the large-scale dynamical properties of the stratosphere and influence the transport, as seen in long-lived tracers distributions such as methane (CH_4) in Fig 1–2. The signature of the upward branch of the B–D circulation is recognized from the tracer-rich tropical bulge. Methane oxidation in the upper stratosphere explains its lower concentration in the downward branch, when compared to the high polar ozone concentrations brought by the B–D circulation. Methane distribution also shows important meridional gradients (forming a three-step staircase) distinguishing the three main latitudinal regions of the stratosphere previously described. Within each of the regions, tracer concentrations are homogenized by shorter-timescale quasi-isentropic mixing in the Surf Zone (Waugh and Hall, 2002) and chemical processes changing the tracer concentrations along their path.

Ozone is the most important chemical species, radiatively, in the stratosphere and reacts chemically on timescales comparable to transport in certain regions. Chemically, the ozone concentration is a balance between the ozone production from the Chapman mechanism and the ozone loss from the different catalytic cycles. The main catalysts are OH and HO_2 , grouped together as the hydrogen oxide radicals family HO_x (further details on stratospheric chemistry can be found in Jacob, 1999; Dessler, 2000). Another family of catalysts are nitrogen oxides NO_x (also called odd nitrogen), composed principally of NO and NO_2 . Note that these species can be grouped together into families because the chemical cycling

between its components happens very fast with respect to other reactions. For example, NO is converted back and forth to NO₂ on timescales of minutes, whereas the family NO_x reacts chemically with ozone on longer timescales. The destruction of ozone by HO_x or NO_x has the same net effect, as two molecules of O₃ are converted to three molecules of O₂ in the catalytic process. However the amount of ozone destruction from both catalysts have specific dependencies on temperature, pressure, solar radiation and tracer concentration, resulting in different effective regions and magnitudes. For example, NO_x concentrations depends strongly on the solar influence as it is converted to its reservoir species HNO₃ during daytime and N₂O₅ at nighttime. The overall result from both catalytic cycles is that photochemical lifetime of ozone decreases with altitude, from years in the lower stratosphere to minutes in the upper stratosphere. Consequently, ozone concentrations are essentially determined by transport in the lower stratosphere and by chemistry in the upper stratosphere. This explains the more homogeneous ozone concentration in the upper stratosphere in Figure 1–1 compared to the strong gradients observed lower down.

There is also a special case of ozone chemistry in the polar stratosphere, happening under threshold temperatures where chlorine and bromine heterogeneous chemistries are activated. These low temperatures are typically experienced in the Antarctic and an “Ozone Hole” is formed almost every winter. We will not focus in details on this phenomenon as it has been widely documented since the discovery by Rowland and Molina (1975) of the role that anthropogenic sources of chlorofluorocarbons (CFC) play and their ban following the Montreal Protocol

in 1987. Also, our study is restricted to Northern Hemisphere winter conditions as the chemistry scheme of the model used (IGCM-FASTOC) does not represent heterogeneous ozone chemistry¹ .

1.1.2 Observing the Stratosphere

The conceptual model of the B–D circulation , the first description of SSW or the Chapman mechanism described in the previous section date from the first half of the 20th century and their genesis is remarkable considering the very limited amount of observations on which they relied. Before the 1950’s, the stratospheric observations were restricted to measurements from episodic aircraft or rubber-balloon launching campaigns. The daily radiosonde launching initiative from Berlin started in 1951 the continuous monitoring of stratospheric climate, and quickly yielded outstanding discoveries, like the SSW of 1952 (Labitzke and Loon, 1999). The satellite era, beginning in 1979, has brought new possibilities to observe the stratosphere but the sparseness of data in terms of variables observed and geographical disposition remains a strong characteristic of the stratospheric observing network.

Nowadays, in-situ observations such as radiosondes, ozonesondes or aircraft measurements represent only a marginal proportion of the available stratospheric data. They are restricted to localized regions around the globe and only sample

¹ An Arctic Ozone Hole has been witnessed for the first time in 2011 (Manney et al., 2011), but the extreme cold temperatures involved were unprecedented and are not reached in any of the model simulations used in this study.

the lower part of the stratosphere, typically below 10 hPa. Satellite observations represent the other kind of available data sources and can be categorized as having either a nadir, solar-occultation or limb viewing geometry (see Part II of Lahoz et al., 2010, for a good overview of observations assimilated in data assimilation systems). These observations are generally passive, meaning that they sense the radiation signal from the atmospheric molecules whose concentrations can then be deduced with a retrieval algorithm.

Nadir-viewing instruments are sensing the atmosphere by looking straight down at the Earth surface, but the radiances they observe have more sensitivity in the lower atmosphere and the retrieved profiles from these radiances thus have low vertical resolution in the stratosphere. They represent the majority of *Operational* stratospheric data, available in near real-time, for NWP. They include for example the radiance observations from the Advanced Microwave Sounding Unit temperature (AMSU-A) and humidity (AMSU-B) instruments placed on various polar-orbiting satellites.

Instruments with solar-occultation, as the name indicates, look directly at the Sun's radiation passing through layers of the atmosphere. HALOE and SAGE missions were terminated in 2005 and ACE-FTS is now the dominant source of solar-occultation measurements. They offer very good vertical resolution and accuracy for a high variety of trace species but only yield a maximum of 30 profiles a day distributed evenly on two latitudes (Manney et al., 2007).

Limb-viewing instruments are sensing layers of the atmosphere parallel to the Earth's surface. This geometry makes these instruments optimal for observing the

stratosphere. The retrieved (level 2) data from passive limb-viewing instruments have good vertical resolution, but relatively poor horizontal resolution (200 to 300 km). Examples of such instruments include the Michelson Interferometer for Passive Atmospheric Sounding (MIPAS) onboard the Envisat satellite or the Microwave Limb Sounder (MLS) on the Aura satellite. The retrievals from these sources include temperature, humidity and ozone profiles as well as profiles of trace species (e.g., HNO_3 , CH_4). These data products are typically called *Research* data as they are not commonly available in near real-time and consequently can not be assimilated for NWP purposes. They still offer excellent products in data assimilation experiments for climate studies or past weather reconstitution. The MIPAS instrument characteristic measurement coverage and errors are taken in this study as basis for the generation of the synthetic data to be assimilated.

Note that there is an interesting recent addition in the category of limb-viewing instruments: Global Positioning System Radio-Occultations (GPS-RO). They are active instruments as they emit a signal and sense the reflected or re-emitted signal from the atmosphere. GPS-RO provide high-quality temperature profiles and have been recently incorporated into operational NWP systems.

One of the major absentee in terms of stratospheric operational or research observations is wind data. Operationally, winds from Atmospheric Motion Vectors (AMV) are derived from cloud movement (as perceived by infrared satellite instruments) but only in the troposphere. Radiosondes are the only source of wind vectors used in assimilation that extends to the stratosphere but, as mentioned, they provide a limited amount of data. One of the most important

middle atmosphere research missions was with the Upper Atmosphere Research Satellite (UARS) which had a high variety of instruments, including the High Resolution Doppler Imager (HRDI) to infer winds. However, the UARS mission stopped in 2005. Since then, no other instruments have taken the relay, although some missions with wind-infering instruments are planned, like the Stratospheric Wind Interferometer For Transport studies (SWIFT; Lahoz et al., 2005) or the Atmospheric Dynamics Mission Aeolus (ADM-Aeolus; Tan et al., 2008).

If the observing system can not provide a regular, fine-resolution, overall view of the stratosphere, numerical models need to supply high-precision simulations for a complete and accurate stratospheric representation.

1.1.3 Modeling the Stratosphere: Chemistry Climate Models

Stratospheric variability is a complex interplay between dynamics, chemistry and radiation on many spatiotemporal scales. Most of the stratospheric phenomena shortly described above have been first investigated with toy models, but as computational power has increased with time, general circulation model (GCM) simulations of the stratospheric climate with comprehensive chemistry, radiation and physics parametrization have become feasible. This is achieved with Chemistry-Climate Models (CCM), now reaching good accuracy when trying to replicate the climate (long-time averaged) state of the stratosphere, as concluded from the two Chemistry-Climate Model Validation campaigns (CCMVal; Eyring et al., 2005).

Details of the CCMVal participating models can be found in Table 1 of Eyring et al. (2006). The common characteristic among CCMs is to include numerous

vertical levels ($\mathcal{O}(50 - 100)$) generally ranging up to 0.01 hPa (80 km altitude) or even higher. This allows to include a full stratosphere free of spurious non-physical effects caused by sponge layers numerically implemented to prevent wave reflection at the model top. Another necessary property of CCMs is the active coupling between chemistry and climate. Here, the chemical tracer concentrations are calculated from an interactive chemical model involving numerous reactions and a transport model. The resulting chemical concentrations can influence the dynamics via the radiative scheme that inputs modeled ozone and water vapor fields. Other input tracers such as CH_4 or CFCs may be specified from climatology. CCMs operate on relatively low spatial resolutions, typically rougher than 2° in the horizontal, implying that they do not explicitly resolve a wide spectrum of gravity waves, essential in obtaining reasonable strength in the B–D circulation. There is a necessity in parametrizing the orographic or non-orographic gravity-wave drag (GWD). In general, the type and complexity of chemical, radiation and advection schemes vary a lot and physical parametrization are less complex than in operational NWP models. These characteristics allow CCMs to sustain simulations over long time periods, which is instructive for past or future climate studies and for understanding the sensitivity of the stratosphere to certain components of the system. To perform studies of future climate, the quality of CCMs must be evaluated beforehand and regular assessments have actually been performed (Pawson et al., 2000; Austin et al., 2003; Eyring et al., 2006; Butchart et al., 2011).

Butchart et al. (2011) find that except for a few notable exceptions, the mean climate states of the modeled stratosphere are generally well reproduced by CCMs without excessive spread between models. The main difficulties in stratospheric modeling regard polar temperature and equatorial winds biases. The temperature problem can be seen in Figure 1–3, in which the long-term climatology of different CCMs are compared to the ERA-40 reanalysis. Most CCMs agree with the ERA-40 reanalysis for the Northern Hemisphere winter (DJF, top left panel) and spring (MAM, top right) polar temperature under 10 hPa. Above 10 hPa, there is a clear warm bias in all models. For the Southern Hemisphere winter (JJA, bottom left) and spring (SON, bottom right) polar temperatures, there is a large multimodel spread with a propensity towards a cold bias, particularly in spring, below 10 hPa. This is often referred to as the “cold-pole problem” (Garcia and Boville 1994) and arises from difficulties in parametrizing sub-grid scale inertial gravity waves appropriately with GWD schemes. These biases have however been improved since previous CCM inter-comparisons (such as Pawson et al., 2000; Austin et al., 2003), notably for the Northern Hemisphere, thanks to improvement in the resolved and parametrized gravity wave drag. The better gravity wave budget in CCMs has reduced the overestimated strength of the B–D circulation and transport barriers leakage, which can be seen from better mean age of air (average residence time of a particle entering the stratosphere (Hall and Plumb, 1994)) in the poles (Eyring et al., 2006). This partly adjusted the temperature bias in the polar vortex. Note that it is difficult to assess the bias with certainty as the reanalyses on which they are calculated also suffer from inaccuracies (Uppala et al., 2005).

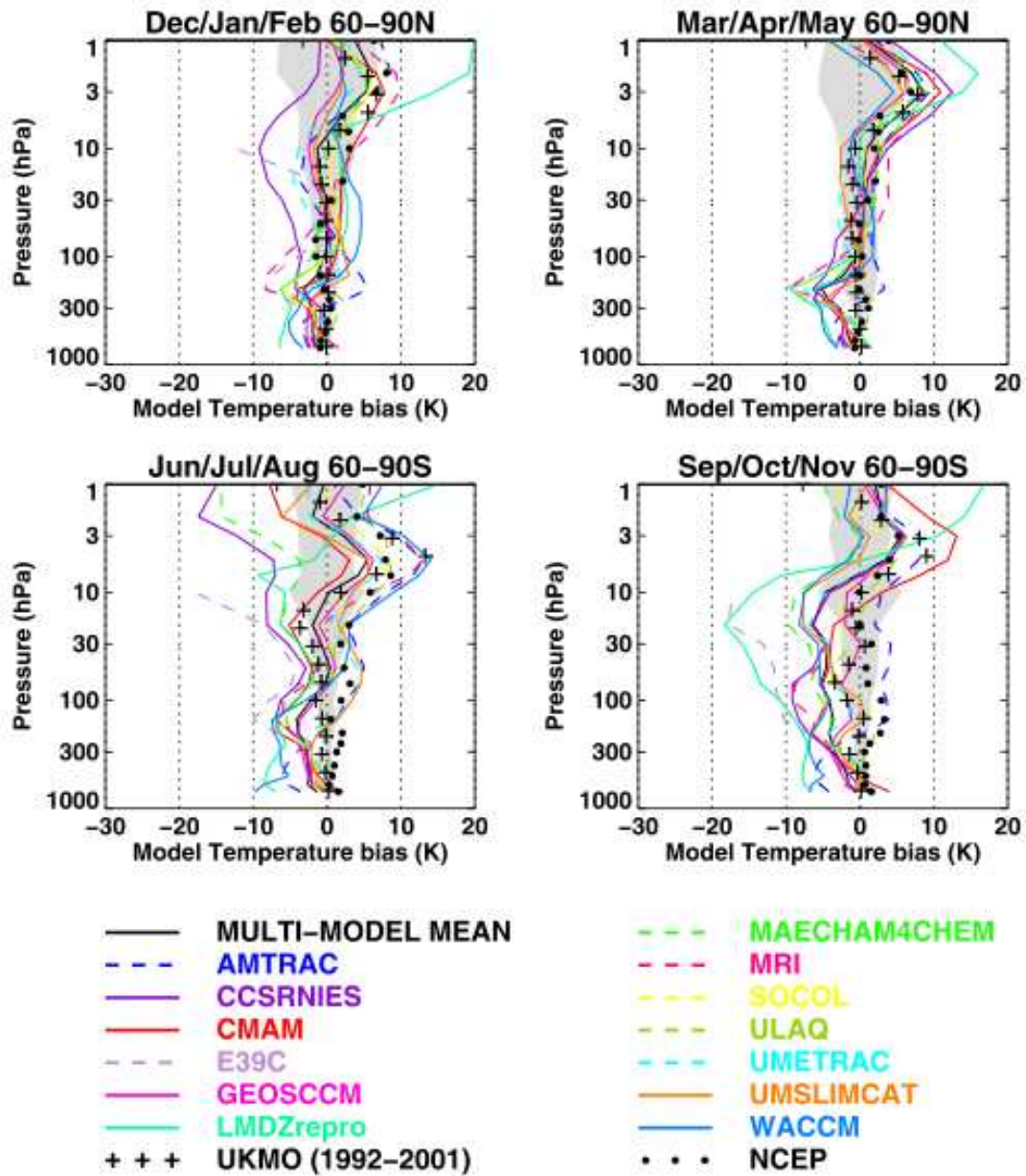


Figure 1-3: Vertical temperature bias relative to ERA-40 reanalyses for 13 chemistry-climate models. Figure from Eyring et al. (2006).

The other main diagnosed problem in CCMs is the lack of QBO in a majority of models (Eyring et al., 2006). A high vertical resolution in lower stratosphere as well as sufficient parametrized wave driving seem to be the necessary ingredients to have an internally generated QBO. As the majority of CCMs produce permanent tropical easterlies, modelers are artificially forcing a QBO from actual stratospheric observations (Giorgetta et al., 2002).

These aspects focus on a climatic view of the stratosphere, but interannual and intraseasonal variability is much less accurate (Butchart et al., 2011). When trying to represent the stratosphere on such timescales, data assimilation might start providing a solution to reduce the errors. The example of the “nudging” technique used for generating a QBO in CCMs points in the direction of incorporating data to improve the estimate of the stratospheric state.

1.1.4 The Stratosphere in Global NWP Forecasts and Reanalyses

Guided by the increasing performance of CCMs, operational NWP centers have raised the lid of their global forecast models over the last few years to include the whole extent of the stratosphere (see the “Resolution [model lid]” column for the main global operational NWP models in Table 1–1). The motivations are multiple, but the main one regards the improvement to medium and long-range tropospheric forecasts, witnessed in operational centers when testing differences between high-lid and low-lid models (Charron et al., 2012). There are some premises explaining these NWP improvements. Stratosphere-on-troposphere influence has first been studied by Boville (1984) and Kodera et al. (1990), but the stratospheric “harbingers” of Baldwin and Dunkerton (1999, 2001) have opened

Table 1–1: Table of the main operational NWP models, reanalyses and ensemble prediction systems with their resolutions and data assimilation schemes.

Operational center (reference)	Model (version)	Resolution [model lid]	Data assimilation scheme [ensemble size]
ECMWF (cited 2012)	IFS (37r3)	T1279 L91[0.01 hPa]	4D-Var
GMAO (cited 2012)	GEOS (5.7.2)	0.25° L72[0.01 hPa]	4D-Var
JMA (cited 2012)	GSM (2007)	T959 L60[0.1 hPa]	4D-Var
NCEP (cited 2012b)	GFS (9.0.1)	T574 L64[0.3 hPa]	3D-Var (GSI)
EC (cited 2012)	GDPS (2.2.0)	66km L80[0.1 hPa]	4D-Var
ECMWF (Dee et al., 2011)	ERA-INTERIM	T255 L60[0.1 hPa]	4D-Var
JMA (Kazutoshi et al., 2007)	JRA-25/JCDAS	T106 L40[0.4 hPa]	3D-Var
GMAO (Rienecker et al., 2011)	MERRA	0.66° L72[0.01 hPa]	3D-Var
NCEP (Saha et al., 2010)	CFSR	T382 L64[0.26 hPa]	3D-Var
NOAA (Compo et al., 2011)	20CR	T62 L28[10 hPa]	EnSRF [56]
JMA (Takemasa et al., 2007)	ALERA	T159 L48[10 hPa]	LETKF [40]
EC (cited 2012)	GEPS (2.0.2)	66km L40[2 hPa]	EnKF[4 × 48]
NCEP (cited 2012a)	GEFS	T190 L28[3 hPa]	3D-Var (GSI) + ETR
MET OFFICE (cited 2012)	MOGREPS	N216 60km L70[0.01 hPa]	4D-Var + LETKF[24]
KMA (cited 2012)	GDAPS	N320 40km L70 [0.01 hPa]	4D-Var + LETKF[24]

the eyes of the forecasting community on the potential impact of the stratosphere on the troposphere.

Another reason to include the stratosphere is to have a prognostic ozone field, instead of relying only on ozone climatologies. This allows for NWP centers to extend their mission to producing increasingly reliable UV forecasts, important for public health reasons. Moreover, an improved ozone field can also be input into the radiation scheme and improve the medium-range forecasts (de Grandpré et al., 2009). However, comprehensive chemistry schemes such as in CCMs have an important computational cost and no operational centers can yet afford to implement them. The European Centre for Medium-Range Weather Forecasts (ECMWF) has implemented a simplified interactive ozone scheme using the modified linearized scheme by Cariolle and Teyssèdre (2007). Other linearized ozone schemes include LINOZ (McLinden et al., 2000) and CHEM2D-OPP (McCormack et al., 2006) which have been used in research contexts and are all reviewed and compared in Geer et al. (2007). They show reasonable agreement with independent observations, outside the upper stratosphere and the Southern Hemisphere polar regions where they display biases. The other option to forecast stratospheric ozone is to drive an external offline chemistry-transport model (CTM) using the modeled winds, as done at the Global Modeling and Assimilation Office (GMAO). CTMs use chemistry schemes with varying degrees of complexity and a transport model driven by winds and temperatures from an external source. The main difference between NWP models with linearized ozone chemistry (or CCMs) and CTMs is in the chemical-dynamical coupling, as the prognostic tracer

concentrations can not feedback to the dynamics via the radiation. In this study an integrated approach on ozone is applied and the ozone-dynamics coupling is investigated during the data assimilation process.

Another important and useful product of operational centers are reanalyses as they provide a consistent climatic view on the atmospheric system, but not exclusively on long-time averages. They are actually long-term reconstitutions of the past weather with sub-daily temporal resolution. Reanalyses use a fixed model and assimilation system to obtain a smooth and coherent temporal evolution of the atmospheric estimate. They have added value over an archive of past NWP analyses as these exhibit occasional “jumps” associated with changes in model resolution, parameter settings or data assimilation schemes (Dee et al., 2011). As noticed in Table 1–1, recent reanalysis projects incorporate the stratosphere, but very few evaluations of their stratospheric products have been published. Exceptions include an inter-comparison of polar vortex warmings by Martineau and Son (2010) and an evaluation of the quality of ERA-INTERIM ozone by Dragani (2011). Stratospheric reanalyses evaluation was a strong recommendation made at the Stratospheric Processes and their Role in Climate Data Assimilation (SPARC-DA, an initiative of the World Meteorological Organization) workshop held in Brussels in 2011.

We have seen that advancement in stratospheric modeling has motivated the NWP centers to include the stratosphere in their products. Conversely, the inclusion of the stratosphere in NWP models stirs up the stratospheric research community to evolve from an exclusive climate perspective to a view that includes

shorter-timescale representation as well. Within NWP and reanalysis is the fundamental aspect of obtaining the most optimal analysis of the atmospheric state, used as initial conditions for forecasting. This is achieved through data assimilation. Whereas troposphere data assimilation has been studied and implemented for a few decades now, stratospheric data assimilation is still at its first steps.

This study seeks to promote the advancement of stratospheric data assimilation by investigating its properties and implication when used with a CCM and when it incorporates chemical-dynamical coupling. Results would likely be directly applicable for future reanalyses. It could also give guidance for NWP suites, which are increasingly looking to exploit the stratosphere and all its components. Considering the specific goals of this study, details on stratospheric data assimilation systems are necessary, with an overview of data assimilation theory and a particular focus on the Ensemble Kalman Filter, chosen for this study.

1.2 Stratospheric Data Assimilation

1.2.1 Data Assimilation Basics

Since the pioneering work of Lorenz (1963) on the chaotic nature of nonlinear dynamical systems, the importance of assessing precise initial conditions is understood to be essential to increase the short and medium-range predictability of the modeled atmosphere. Atmospheric forecasts, with their numerous degrees of freedom, display a strong sensitivity to initial states, such that slight initial differences are likely to diverge exponentially as the system evolves in time. Assuming that a model is perfect, an unconstrained (i.e., without assimilation of observational data) simulation will follow a possible state of the atmosphere

but certainly not the real one. In order to mimic the real atmosphere, the model needs to be directed along the actual flow. This is done by incorporating real but noisy and sometimes biased atmospheric observations to the model which also exhibits errors and biases. An objective technique is needed to find the optimal combination of both sources of information, by properly estimating their uncertainties. This is, in quick terms, the problematic of data assimilation in modeling chaotic systems.

The general data assimilation update, for a given assimilation time window (period over which observations are assimilated to obtain the analysis), can best be described with a Bayesian formulation. The state vector \mathbf{x} seeks to estimate the true atmospheric state \mathbf{x}^t and has a probability density function (PDF) $f(\mathbf{x})$ giving the probability of all its possible values, and therefore the uncertainty. The atmosphere is sampled by the observations \mathbf{y} having PDF $f(\mathbf{y})$. Bayes' theorem states that:

$$f(\mathbf{x}|\mathbf{y}) = \frac{f(\mathbf{y}|\mathbf{x})f(\mathbf{x})}{f(\mathbf{y})} \propto f(\mathbf{y}|\mathbf{x})f(\mathbf{x}) \quad (1.1)$$

where $f(\mathbf{x}|\mathbf{y})$ is the joint probability distribution of the state \mathbf{x} given observations \mathbf{y} . It is also called the *posterior* or *analysis* PDF: the output calculated in the data assimilation procedure. Essentially, the posterior PDF is a product of the *prior* PDF $f(\mathbf{x})$ of the state \mathbf{x} and the *observation* PDF $f(\mathbf{y}|\mathbf{x})$, which gives the likelihood of an observation taking a given value of the state \mathbf{x} it samples. Note that $f(\mathbf{y}) = \int f(\mathbf{y}|\mathbf{x})f(\mathbf{x})d\mathbf{x}$ is generally not analytically solvable and is simply a normalization factor, hence the proportional sign (\propto) in Eqn. (1.1).

NWP is a repetitive process of forecast and analysis. The forecast (prior) state \mathbf{x}_k^f at an arbitrary discrete time t_k is the result of a forward integration in time by the nonlinear model of the atmosphere \mathcal{M} from the analysis (posterior) state at a previous timestep \mathbf{x}_{k-1}^a , subject to model noise η :

$$\mathbf{x}_k^f = \mathcal{M}_{k-1}(\mathbf{x}_{k-1}^a) + \eta_{k-1} \quad (1.2)$$

which in terms of Bayesian formulation can be written as $f(\mathbf{x}_k^f|\mathbf{x}_{k-1}^a)$, the conditional PDF of the forecast given the previous analysis. In the data assimilation step at time t_k , the estimation of the analysis PDF $f(\mathbf{x}_k^a|\mathbf{y}_k)$ with (1.1) requires the forecast distribution $f(\mathbf{x}_k^f|\mathbf{x}_{k-1}^a)$ which in turn depends on the analysis distribution at the previous analysis timestep $f(\mathbf{x}_{k-1}^a|\mathbf{y}_{k-1})$. One can realize that this is a sequential process that originates at the initial conditions $f(\mathbf{x}_0)$ integrated until the first observations \mathbf{y}_1 are available. After algebraic manipulation, we can obtain the expression for analysis state PDFs at all times subject to all assimilated observations:

$$f(\mathbf{x}_{1:k}^a|\mathbf{y}_{1:k}) \propto f(\mathbf{x}_0) \left(\prod_{i=1}^k f(\mathbf{y}_i|\mathbf{x}_i^f) \right) \left(\prod_{i=1}^k f(\mathbf{x}_i^f|\mathbf{x}_{i-1}^a) \right) \quad (1.3)$$

Eqn (1.3) expresses the aggregate data assimilation problem. In NWP, the process is approached sequentially with the analysis PDF calculated at time k from the product of the observation conditional PDF and the forecast conditional PDF:

$$f(\mathbf{x}_k^a|\mathbf{y}_k) \propto f(\mathbf{y}_k|\mathbf{x}_k^f) f(\mathbf{x}_k^f|\mathbf{x}_{k-1}^a) \quad (1.4)$$

For a more complete overview of Bayesian formalism of time-dependent assimilation schemes, we refer to Lewis et al. (2006).

Using this Bayesian approach with full forecast and observation PDFs is not feasible considering the NWP models state and observation vector sizes of $n \approx 10^7$ variables and $p \approx 10^5 - 10^6$ measurements, respectively. Discretizing the PDFs for each variable and measurement would further increase the computer memory requirements. The usual approximation to simplify the problem is to assume that all PDFs can be approximated as Gaussian PDFs, so that they can be completely specified by the first two statistical moments of the distribution: the mean and covariance. This way, it is possible to obtain a simple formulation for the analysis estimate. The following derivations are based on the reference book by Daley (1991). The model forecast state vector $\mathbf{x}^f \in \mathbb{R}^n$ and the observations state vector $\mathbf{y} \in \mathbb{R}^p$ can be related to the unknown true state \mathbf{x}^t :

$$\mathbf{x}^f = \mathbf{x}^t + \mathbf{e}^f \tag{1.5}$$

$$\mathbf{y} = \mathcal{H}(\mathbf{x}^t) + \varepsilon \tag{1.6}$$

where \mathbf{e}^f and ε are the forecast and observation errors, respectively. \mathcal{H} is the nonlinear operator mapping the observation onto the model space. The forecast- and observation-error covariance matrices are by definition:

$$\mathbf{P}^f = \langle (\mathbf{e}^f)(\mathbf{e}^f)^T \rangle = \langle (\mathbf{x}^f - \mathbf{x}^t) (\mathbf{x}^f - \mathbf{x}^t)^T \rangle \in \mathbb{R}^{n \times n} \tag{1.7}$$

$$\mathbf{R} = \langle (\varepsilon)(\varepsilon)^T \rangle = \langle (\mathbf{y} - \mathcal{H}(\mathbf{x}^t)) (\mathbf{y} - \mathcal{H}(\mathbf{x}^t))^T \rangle \in \mathbb{R}^{p \times p} \tag{1.8}$$

where the angle brackets $\langle \cdot \rangle$ represent the expectation value. The error covariance matrices hold the variance of all state variables in their diagonal entries and the covariances between each pair of variables in their off-diagonal entries. Note that the covariance between two variables is equal to the correlation between them multiplied by the standard deviation of each.

The forecast and observation PDFs can be expressed as a function of a model state vector $\mathbf{x} \in \mathbb{R}^n$ predicting the true atmospheric state \mathbf{x}^t in their multivariate Gaussian form:

$$f(\mathbf{x}) = \frac{1}{(2\pi)^{n/2} |\mathbf{P}^f|^{1/2}} \exp \left[-\frac{1}{2} (\mathbf{x}^f - \mathbf{x})^T (\mathbf{P}^f)^{-1} (\mathbf{x}^f - \mathbf{x}) \right] \quad (1.9)$$

$$f(\mathbf{y}|\mathbf{x}) = \frac{1}{(2\pi)^{p/2} |\mathbf{R}|^{1/2}} \exp \left[-\frac{1}{2} (\mathbf{y} - \mathcal{H}(\mathbf{x}))^T (\mathbf{R})^{-1} (\mathbf{y} - \mathcal{H}(\mathbf{x})) \right] \quad (1.10)$$

and the expression for the posterior distribution can be set up using Bayes' theorem (Eqn. (1.1)):

$$f(\mathbf{x}|\mathbf{y}) \propto \exp \left[-\frac{1}{2} \left((\mathbf{x}^f - \mathbf{x})^T (\mathbf{P}^f)^{-1} (\mathbf{x}^f - \mathbf{x}) + (\mathbf{y} - \mathcal{H}(\mathbf{x}))^T (\mathbf{R})^{-1} (\mathbf{y} - \mathcal{H}(\mathbf{x})) \right) \right] \quad (1.11)$$

There are two approaches to solving for the analysis state vector $\mathbf{x} = \mathbf{x}^a$, leading to the *variational* data assimilation methods and the *Kalman filter* data assimilation methods. Interestingly, both approaches yield initial analysis equations which can be written in the same form when background and observation errors are uncorrelated and have Gaussian PDFs.

The first approach seeks the maximum-likelihood analysis by finding the maximum value of $f(\mathbf{x}|\mathbf{y})$, hence the minimum value of the gradient of the cost-function \mathcal{J} with respect to the state \mathbf{x} :

$$\frac{d}{d\mathbf{x}}(\mathcal{J}(\mathbf{x})) = \frac{d}{d\mathbf{x}} \left(\frac{1}{2} (\mathbf{x}^f - \mathbf{x})^T (\mathbf{P}^f)^{-1} (\mathbf{x}^f - \mathbf{x}) + \frac{1}{2} (\mathbf{y} - \mathcal{H}(\mathbf{x}))^T (\mathbf{R})^{-1} (\mathbf{y} - \mathcal{H}(\mathbf{x})) \right) = 0 \quad (1.12)$$

The second approach directly applies a least-square perspective: the analysis state \mathbf{x}^a minimizes the analysis error variance, held in the diagonal part of the analysis-error covariance matrix \mathbf{P}^a . The derivation is presented in Appendix A and involve two fundamental assumptions: (i) the forecast and observations are unbiased (ii) the forecast and observation errors are uncorrelated. It yields the following analysis equations:

$$\mathbf{x}^a = \mathbf{x}^f + \mathbf{K} (\mathbf{y} - \mathcal{H}(\mathbf{x}^f)) \quad (1.13)$$

$$\mathbf{P}^a = (\mathbf{I} - \mathbf{K}\mathbf{H}) \mathbf{P}^f \quad (1.14)$$

with the Kalman Gain

$$\mathbf{K} = \mathbf{P}^f \mathbf{H}^T (\mathbf{H} \mathbf{P}^f \mathbf{H}^T + \mathbf{R})^{-1} \quad (1.15)$$

\mathbf{H} is the linearized version of the measurement operator \mathcal{H} . The variational solution equation of (1.12) can also be written in the form of the Kalman filter analysis equation (1.13) but a static forecast-error covariance matrix \mathbf{P}^f is used in the Kalman Gain (1.15).

Equation (1.13) can be rewritten as:

$$\delta\mathbf{x} = \mathbf{K}\mathbf{d} \quad (1.16)$$

to express the data assimilation step as a simple input-output operation, where the input *observation innovations* $\mathbf{d} = \mathbf{y} - \mathcal{H}(\mathbf{x}^f)$ are converted to *analysis increments* $\delta\mathbf{x} = \mathbf{x}^a - \mathbf{x}^f$ by the operator \mathbf{K} .

The optimality of the analysis \mathbf{x}^a and its error covariance matrix \mathbf{P}^a relies explicitly on the proper specification of the error covariance matrices \mathbf{P}^f and \mathbf{R} . The specification of the observation-error covariance matrix \mathbf{R} involves finding the accurate instrumental errors. A common assumption is that errors between observations are not correlated, yielding a diagonal \mathbf{R} matrix. It is however recognized that retrieved profiles from satellite radiances have some correlation between levels (Garand et al., 2007). The specification of the forecast-error covariance matrix \mathbf{P}^f involves both obtaining accurate magnitude of the forecast error for each variable and appropriate correlations between the errors of each variables. This last task is particularly difficult to specify analytically, and many techniques have been developed to obtain reasonable estimates, such as the Hollingsworth and Lönnberg (1986) method, the NMC method (Parrish and Derber, 1992) or the analysis-ensemble approach (Belo Pereira and Berre, 2006).

Historically, different data assimilation schemes have been elaborated for the assimilation of observations in atmospheric models, usually increasingly complex as computational power is less and less of a constraint. On the one hand, the maximum-likelihood approach to solving for the analysis gave rise to the variational type of data assimilation filters, namely the three-dimensional variational assimilation (3D-Var, Parrish and Derber 1992) and the four-dimensional variational assimilation (4D-Var, Talagrand and Courtier 1987). These variational methods

are commonly used in operational NWP settings (c.f. the “data assimilation scheme” column of Table 1–1) and use a minimization algorithm to find the most likely analysis state \mathbf{x}^a . On the other hand, the least-square minimum-variance estimate has produced the first historical application of a data assimilation filter, the optimal interpolation (OI, Gandin 1963, although the equations were first derived by Eliassen 1954) analysis scheme and later on, its extension to nonlinear dynamics, the Extended Kalman Filter (EKF; derivation in Appendix A). OI and EKF solve the analysis equations (1.13 - 1.15) explicitly instead of using a minimization algorithm. However, this is usually done sequentially using subsets of observations instead of assimilating all observations simultaneously. We will not focus on OI or 3D-Var as they can be seen as simplifications of the EKF and 4D-Var which have an added temporal aspect in the assimilation process.

EKF has the added aspect of explicitly propagating error covariances in time. This is done with the tangent linear model (TLM) \mathbf{M} of the full nonlinear model \mathcal{M} such that:

$$\mathbf{P}_{k+1}^f = \mathbf{M}_k \mathbf{P}_k^a \mathbf{M}_k^T + \mathbf{Q}_k + \text{higher order terms} \quad (1.17)$$

where $\mathbf{Q} = \langle \eta\eta^T \rangle$ is the model-error covariance matrix. The derivation is provided in Appendix A. In 4D-Var, the error covariance matrix is static but the adjoint \mathbf{M}^T to the TLM is used to propagate analysis increments from the observation time backwards to the analysis time. This represents an implicit variation of the background-error covariances within the time window of the assimilation step. Then, a forecast may be launched from the newly-obtained analysis to perform a new minimization of the cost-function, which is computationally

expensive. Indeed, the cost related to the time propagation of model-space error covariance matrices having size $n \times n$ is enormous. A reduced-resolution version of the TLM is often used to minimize the computational cost. Note also that both filters are suboptimal as they use a linearized version of the nonlinear model with a closure scheme neglecting third- and higher-order moments in the error statistics prediction (see Appendix A). Particularly, the EKF can have issues with its error variance evolution and in the consequent proper estimation of the analysis (Evensen, 1992).

The adopted specification technique for the forecast error covariances in EKF and 4D-Var is therefore to produce an initial generic \mathbf{P}^f and to let it evolve with time explicitly using a TLM propagation or implicitly with the TLM adjoint. An alternative to this approach has been developed, using a Monte-Carlo method, and is presented in the following section.

1.2.2 Ensemble Kalman Filter

EnKF Formulation. An alternative to the EKF was developed by Evensen (1994) and named the Ensemble Kalman Filter (EnKF). The single major difference is the estimation of forecast error statistics using a Monte-Carlo method in the EnKF instead of the time propagation of the forecast-error covariance matrix with the TLM in the EKF. In the EnKF, the time-dependent forecast-error covariance matrix is calculated from an ensemble of nonlinear model forecasts initialized from random initial model states. The analysis equations remain similar to (1.13 - 1.15), except for the ensemble of model states \mathbf{x}_j with $j = 1, 2, \dots, m$ indexing the different model realizations. m is the ensemble size. This yields the ensemble of

analysis states \mathbf{x}_j^a , the ensemble-based (or sample) analysis-error covariance matrix \mathbf{P}_e^a and the ensemble Kalman Gain \mathbf{K}_e :

$$\mathbf{x}_j^a = \mathbf{x}_j^f + \mathbf{K}_e (\mathbf{y}_j - \mathcal{H}(\mathbf{x}_j^f)) \quad (1.18)$$

$$\mathbf{P}_e^a = (\mathbf{I} - \mathbf{K}_e \mathbf{H}) \mathbf{P}_e^f \quad (1.19)$$

$$\mathbf{K}_e = \mathbf{P}_e^f \mathbf{H}^T (\mathbf{H} \mathbf{P}_e^f \mathbf{H}^T + \mathbf{R}) \quad (1.20)$$

with the ensemble-based (or sample) forecast-error covariance matrix \mathbf{P}_e^f :

$$\mathbf{P}_e^f = \langle (\mathbf{x}_j^f - \langle \mathbf{x}^f \rangle) (\mathbf{x}_j^f - \langle \mathbf{x}^f \rangle)^T \rangle = \frac{1}{m-1} \sum_{j=1}^m (\mathbf{x}_j^f - \langle \mathbf{x}^f \rangle) (\mathbf{x}_j^f - \langle \mathbf{x}^f \rangle)^T \quad (1.21)$$

Comparing the forecast-error covariances of equations (1.7) and (1.21), the unknown true state \mathbf{x}^t is approximated in the EnKF scheme by the forecast ensemble average $\langle \mathbf{x}^f \rangle = (\sum_{j=1}^m \mathbf{x}_j^f) / m$. The forecast error covariances are therefore derived from the spread of the nonlinear model forecasts about the ensemble average. The EKF closure problem is prevented here, as the full nonlinear model is used for the ensemble of forecasts. However, the EnKF still solves for the KF equations that only take into account the first two statistical moments of the PDFs.

The EnKF equation (1.18) can be practically formulated with ensemble matrices holding in its columns the model state or observation vector from each ensemble member (Evensen, 2003), provided that the observation operator \mathbf{H} is linear.

$$\mathbf{X}^a = \mathbf{X}^f + \mathbf{K}_e (\mathbf{Y} - \mathbf{H} \mathbf{X}^f) \quad (1.22)$$

Uppercase letters are used to differentiate matrices from vectors.

Note, for completeness, that an ensemble of model states (analogous to $f(\mathbf{x}_0)$ of equation (1.3)) is required to initialize the first ensemble of forecasts up to the first observation time. Ensembles can be initiated by generating random perturbations specified from a given error covariance matrix and adding them to a single forecast state. Care must be taken to have dynamically-balanced perturbations to obtain reasonable initial model states (Evensen, 2003).

The formulation of the EnKF is simple but its implementation raises a few noteworthy considerations discussed below. These should help the reader understand some necessary choices made for the development of the ensemble data assimilation system in this study.

Deterministic and Stochastic Ensemble Updates. In equation (1.18), the observations \mathbf{y}_j are treated as random variables and have an ensemble index j . This is necessary in the EnKF formulation for the analysis-error covariance matrix equation (1.19) and the Kalman Gain (1.20) to retain their KF formulations, as explained in Burgers et al. (1998). Otherwise, the analysis-error covariance matrix (Eqn. (5.18) in Appendix A) loses the $\mathbf{K}\mathbf{R}\mathbf{K}^T$ term, a possible direction of error growth, spuriously reducing the \mathbf{P}^a variance. If all ensemble members are updated with the same observation set, the analysis-error covariance matrix can keep its KF formulation (1.19) if the Kalman Gain (1.20) becomes:

$$\tilde{\mathbf{K}} = \left(1 + \sqrt{\frac{\mathbf{R}}{\mathbf{H}\mathbf{P}^f\mathbf{H}^T + \mathbf{R}}} \right)^{-1} \mathbf{K} \quad (1.23)$$

This “square-root” transformation of the Kalman Gain marks the theoretical difference between the two major categories of ensemble data assimilation filters: the stochastic EnKF and the deterministic Ensemble Square-Root Filters (EnSRF) (Lawson and Hansen, 2004). The random variable or scalar treatment of observations induces specificities in the ensemble data assimilation update procedure.

In the stochastic EnKF, unbiased Gaussian random perturbations with standard deviations equal to the instrumental error standard deviations are added to the assimilated observations to create an ensemble of observations. The update procedure is purely stochastic as each random forecast member is combined, using (1.18), to a randomized version of the assimilated observations to obtain an analysis member. The stochastic EnKF is also referred to as “perturbed-observations” EnKF.

The deterministic EnSRF is non-unique and different algorithms have been developed yielding similar solutions such as the Ensemble Adjustment Kalman Filter (EAKF; Anderson, 2001) or the Ensemble Transform Kalman Filter (ETKF; Bishop et al., 2001), as analyzed by Tippett et al. (2003). Each EnSRF updates the forecast ensemble mean vector and the forecast-error covariance matrix with a single realization of the observations. The EnSRF update produces an analysis mean vector and analysis-error covariance matrix from which the analysis members are randomly generated to initiate the next forecast phase. This contrasts with the stochastic EnKF where the ensemble of forecasts is updated with the ensemble of

observations yielding directly an ensemble of analysis states, so that the analysis-error covariance matrix is not explicitly calculated.

Few theoretical arguments have been formulated to motivate the use of one type of filter versus the other. The EnSRF has the advantage of bypassing the sampling error introduced in the EnKF by perturbing the observations, broadening the \mathbf{P}^a distribution (Whitaker and Hamill, 2002). Lawson and Hansen (2004) tested the filters in models ranging from 1D to 3D, and in regions with different degrees of normality. They found that deterministic filters start losing quality as the model nonlinearity increases, which is much less the case for stochastic filters. Their 1D nonlinear model results are particularly probing. They update, with the EnKF and EnSRF, a bimodal PDF with an observation tending toward one of the two peaks and compare the analyses to the distribution expected from Bayes' rule. The results are shown in Figure 1–4 for three levels of uncertainty in the observations. Whereas the linear case (not shown) with an initial Gaussian distribution produces similar results for both filters, the nonlinear one does not. No matter how certain is the observation, the EnSRF produces an updated bimodal distribution and can not determine which peak is the most probable. Consequently, a large portion of ensemble members lies outside the expected error standard deviation, especially for cases with smaller observation errors. The retained bimodality is indicative of the deterministic filter property to *linearly* transform the prior PDF into the posterior PDF, thereby keeping the same shape. Contrarily, the stochastic combination between the Gaussian-perturbed observation PDF and the bimodal prior PDF permits to populate the space in-between the

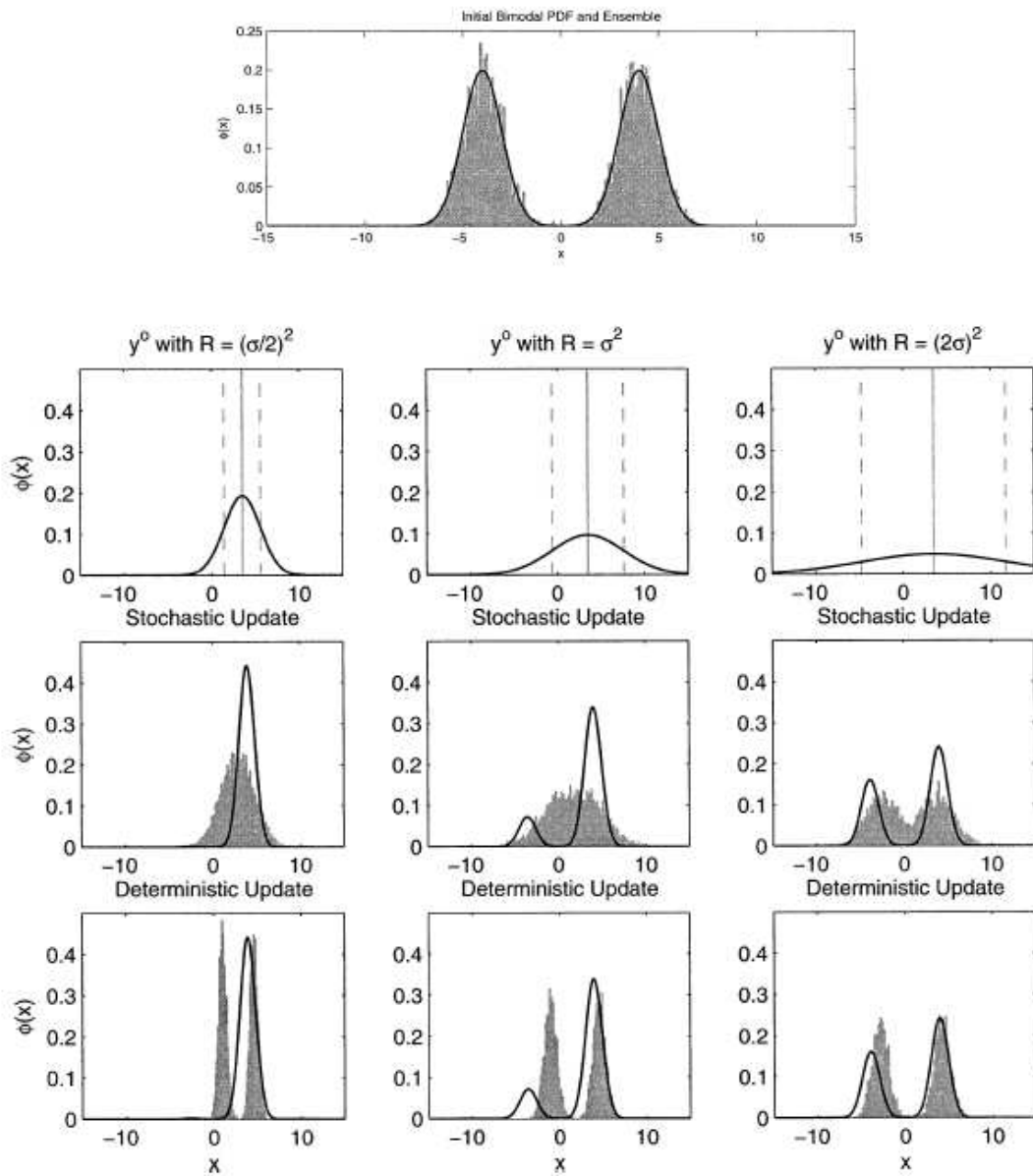


Figure 1–4: The top figure shows the initial bimodal background PDF (black line) and the 5000 ensemble members populating it (gray histogram). The second row shows the three observation scenarios. The last two rows show respectively the stochastic and deterministic filter ensemble updates (gray histogram) and the Bayes' rule expected PDF (black lines). Figures 1(b) and 3 of Lawson and Hansen (2004).

peaks. The observation PDF allows to broaden and make more Gaussian the posterior PDF, preventing high likelihood in regions deemed unlikely by the observations. The better behavior of stochastic filters as nonlinearity grows in models is also encountered in higher-dimensioned cases, such as the 2D Ikeda system or the Lorenz 95 latitude circle model (Lawson and Hansen, 2004).

The choice of filter depends on the properties of the model on which it is applied. The deterministic filters produce decent results with smaller ensembles (Figure 2 in Whitaker and Hamill, 2002), a crucial point considering that computational cost is a major criterion for the choice of a filter. However, no matter how beneficial is the time gain, the EnSRF behavior in the nonlinear context is worse. Despite the Lawson and Hansen (2004) study, EnSRFs are common in NWP applications and achieve good results. For example, the EnSRF outperformed a 3D-Var scheme in a reduced-resolution version of the NCEP Global Forecasting System (GFS) (Whitaker et al., 2008). It is also used in the National Oceanic and Atmospheric Administration (NOAA) 20th century reanalysis (20CR Compo et al., 2011, see Table 1–1 for details). The Stochastic EnKF was tested against 3D-Var and similar performances were witnessed (Houtekamer et al., 2005).

However, considering the importance of nonlinearities linked to wave-breaking and chemistry in the stratosphere, the stochastic EnKF has been chosen in this study. In the remainder of this introductory chapter, the term “EnKF” is generic and can apply to both stochastic or deterministic filters, unless specified otherwise.

Finite ensembles. The EnKF has the advantage of offering a convenient technique of estimating the forecast error covariances, but it does suffer from a

suboptimality that need to be compensated appropriately. It regards the finite ensemble size m used to calculate the error covariances. In using a Monte-Carlo approach to estimate the forecast error statistics, the ensemble must capture realistically the variances and correlations of the nonlinear model. Even for linear dynamics, the EnKF solution will only equate the KF solution if the ensemble size approaches infinity (Burgers et al., 1998). In practice, limited computational power forces the maximum ensemble size m to a finite and relatively small value of $\mathcal{O}(50 - 100)$. The forecast-error covariance matrix \mathbf{P}_e^f has a maximum rank of $m - 1$ and suffers from rank-deficiency, as $m - 1 \ll n$. The analysis is only corrected in the error subspace spanned by the ensemble members (Nerger et al., 2005). In other words, having a number of ensemble members smaller than the model degrees of freedom, the model forecasts can not capture all the directions of error growth, affecting the amount of variability (spread) in the ensemble. The difference between the sample analysis error covariance matrix \mathbf{P}_e^a (1.19) and its KF equivalent \mathbf{P}^a (1.14) is of order of $m^{-1/2}$ with a tendency to underestimate the sample error covariances (Burgers et al., 1998). Another consequence of finite ensemble size on forecast-error covariance matrices is the pollution of error correlations by sampling noise, producing spurious values between far-away grid points (Houtekamer and Mitchell, 1998). An increased number of ensemble members can partially reduce these effects but compensation mechanisms are still necessary to reduce sampling error and increase the rank of \mathbf{P}_e^f . In doing so, an optimal balance between analysis quality and computational efficiency must be found.

Filter divergence. Both the underestimation of variances and the spurious correlations brought on by the finite ensemble size lead to a common problem in ensemble data assimilation: filter divergence. Figure 1–5 gives a visual example of how these affect the analysis and lead to this problem.

All three panels of the figure show the background PDF (thick lines) of variables x_1 and x_2 in their respective state spaces as well as the two-dimensional $x_1 - x_2$ state space. Only variable x_1 is observed and its observation PDF is shown (thin lines). The updated analysis PDFs (dashed lines) are shown both in x_1 and $x_1 - x_2$ space. The effect of specifying \mathbf{P}_e^f from a small ensemble can be understood by comparing the insufficient-variance case of Fig. 1–5b to the true background and analysis control case of Fig. 1–5a . The insufficient-variance background PDF produces an analysis PDF more confined in state space than the true analysis PDF. It therefore has a lower analysis variance which should imply more certainty in the analysis solution, in a minimum-variance scheme such as the EnKF. However the average analysis state differs from the true average analysis. The concept of filter divergence arises from that. The filter gives certainty to a biased analysis value, which in turn is the initial condition for the following forecast phase. The next forecast PDF is likely to be too narrow as well, producing again a lower-variance estimate for the analysis. After a few iterations, the forecast variance becomes very small compared to the observation variance and the minimum-variance filter discredits the observation in favor of the forecast, even though the forecast state may be biased with respect to the truth.

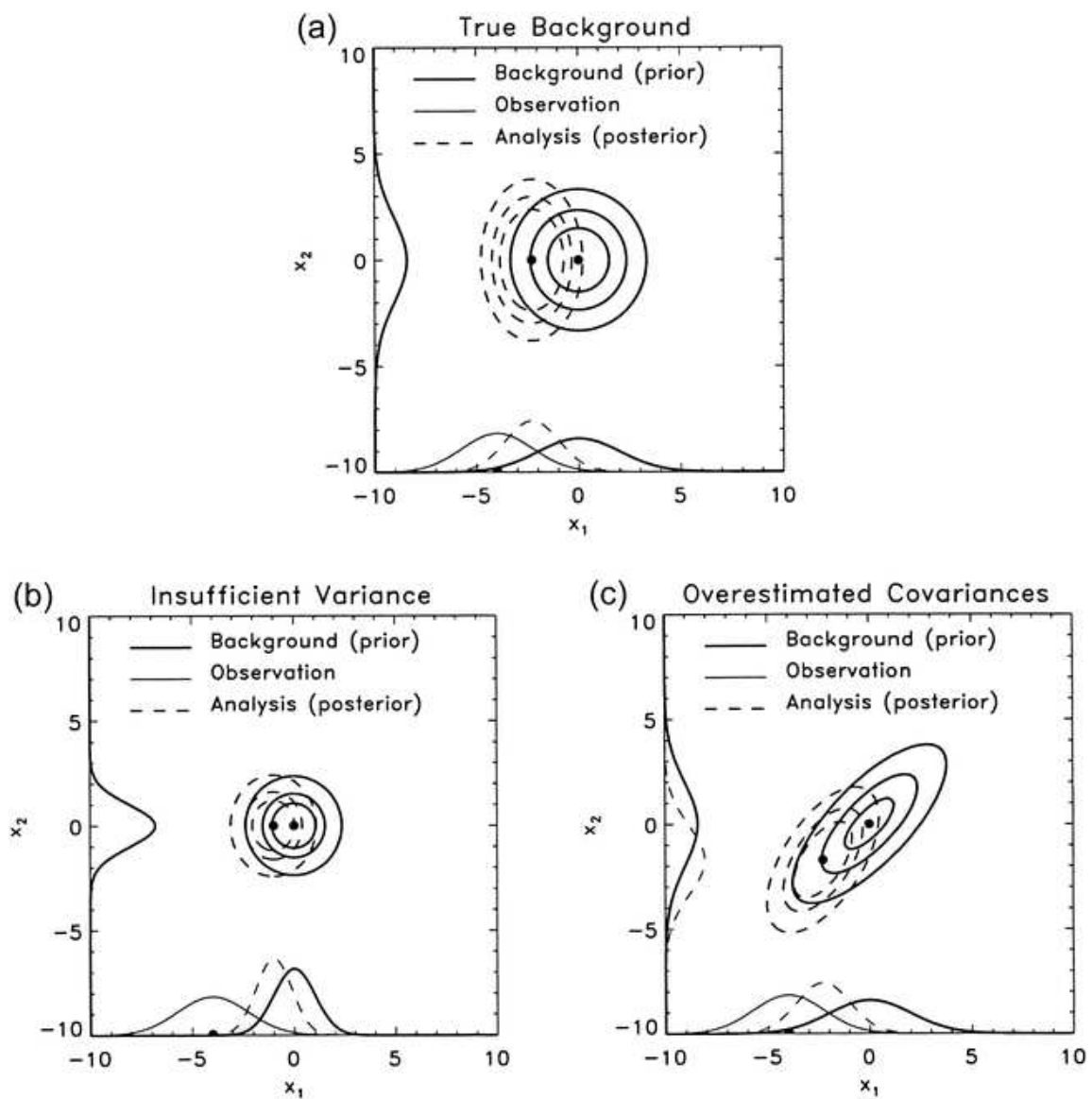


Figure 1-5: Analysis, background and observation distributions in 2D space for (a) a control state, and two special cases of (b) insufficient variance and (c) overestimated covariances. Figure 3 of Hamill et al. (2001).

Filter divergence can also be witnessed from spurious correlations. Horizontal correlation between two variables are expected to decrease sharply with distance so sampling error in covariances between distant grid points induces a very high noise-to-signal ratio, which is likely to damage the analysis (Hamill et al., 2001). This is illustrated when comparing Figures 1–5a and 1–5c. In the true and overestimated-covariance cases, the variances are equal for all background PDFs, the difference lies in the spurious correlation between x_1 and x_2 in the background error covariance matrix \mathbf{P}^f , as seen from the slanted background PDF in the 2D state space of Fig. 1–5c. The spurious covariances produce analysis increments in x_2 from assimilating observation in x_1 space, although there should not be any cross-variable effect, as seen in the control case (Fig. 1–5a). The resulting x_2 analysis is not the best estimate but its analysis variance has been reduced in the assimilation process. This may again lead to filter divergence.

From this simple 2D example, another fundamental aspect of error covariances is perceived: they allow for the transfer of information from the observed variable to correlated variables. These error covariances are double-edged swords, as they might be very beneficial in order to constrain unobserved variables, but might also prove detrimental if not correctly specified. In the case of the stratosphere where observations are relatively sparse and some variables (e.g., winds) are not observed, correct error covariances become essential in producing beneficial and balanced analysis increments for the whole domain.

Increasing the variance. Two important strategies of mitigation have been elaborated to counter the insufficient forecast variance, potentially leading to

filter divergence. One of them, the double-EnKF (DEnKF), is a more fundamental approach, while the other, covariance inflation, is more ad hoc.

The DEnKF increases the error variances underestimated due to calculating the Kalman Gain from the same forecast members that are updated (Houtekamer and Mitchell, 1998). The DEnKF technique of Houtekamer and Mitchell (1998) uses the members of a first ensemble of size $m/2$ to calculate the Kalman Gain error covariance statistics and update the members of the second ensemble of size $m/2$. The first ensemble is then updated using the Kalman Gain calculated from the second forecast ensemble. The process is schematized in Figure 1–6. The DEnKF achieves boosting up the variance, and even overestimates the real variance, as hypothesized by van Leeuwen (1999) and verified experimentally by Whitaker and Hamill (2002). Note that the DEnKF has been further extended to a Quadruple-EnKF for the ensemble prediction system at Environment Canada (EC) (see Table 1–1).

The other common technique to increase the forecast error variances is using a tunable parameter to inflate the error covariances (Anderson and Anderson, 1999). Inflation can either be multiplicative, where each member’s departure from the ensemble average is multiplied by a constant coefficient (Hamill et al., 2001; Pham, 2001) or additive, where a random vector with specified error covariance is added to each forecast member (Houtekamer et al., 2005; Whitaker et al., 2008). In the cases of multiplicative inflation, some offline estimation techniques have been developed to determine an optimal inflation parameter (Anderson, 2007a; Li et al., 2009). A relatively small inflation coefficient of a few percents is usually

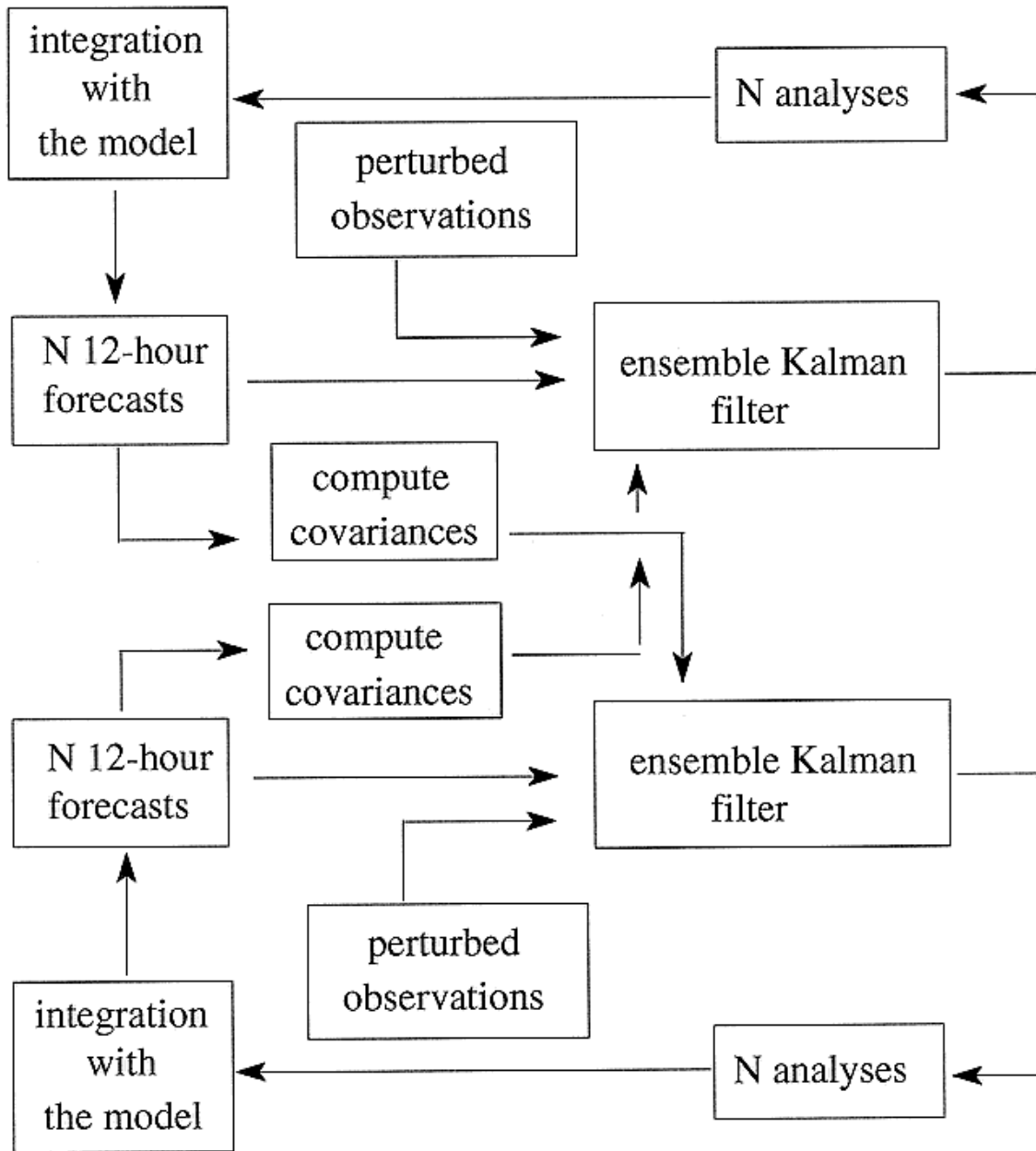


Figure 1-6: Double Ensemble Kalman filter assimilation scheme where one ensemble is updated using the statistics obtained from another. Figure 2 of Houtekamer and Mitchell (1998).

sufficient to obtain stable performances by the filter. Optimal inflation depends on the ensemble size and on the observation network density. Therefore a uniform coefficient is not optimal and the inflation should ideally be region-dependent (Miyoshi et al., 2010). In the case of additive inflation, some knowledge is required on the optimal shape and magnitude of the random vector to be added.

Correcting the correlations. To ensure that sampling noise does not pollute error covariances and to increase the subspace spanned by the ensemble, a technique of covariance localization has been developed by Houtekamer and Mitchell (2001). Covariance localization is a refinement on the concept of the “radius of influence” of an observation, where the error covariances were set to zero beyond a certain distance (Houtekamer and Mitchell, 1998). This however produced discontinuities at the edge of the radius, producing unbalanced analysis increments. In covariance localization, the forecast error covariances are multiplied with a correlation function ρ by Schur (element-wise) product. ρ is usually a function that resembles a Gaussian, monotonically decreasing with distance, most of the time a fifth-order autoregressive function (Gaspari and Cohn, 1999). It smoothes the covariances as a function of physical distance between model variables, up to a specified decorrelation length scale beyond which all covariances are zero. The localized covariance in the Kalman Gain is applied this way:

$$\mathbf{K} = [(\rho \circ \mathbf{P}^f)\mathbf{H}^T] [\mathbf{H}(\rho \circ \mathbf{P}^f)\mathbf{H}^T + \mathbf{R}]^{-1} = [\rho \circ (\mathbf{P}^f\mathbf{H}^T)] [\rho \circ (\mathbf{H}\mathbf{P}^f\mathbf{H}^T) + \mathbf{R}]^{-1} \quad (1.24)$$

where the \circ denotes the element-wise product. Covariance localization has been tested statistically by Hamill et al. (2001) who argued that it offers a more

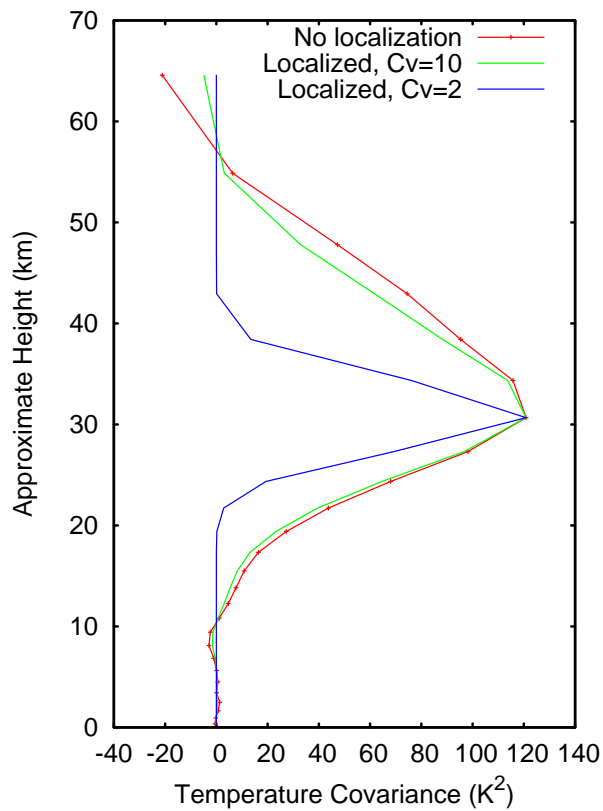


Figure 1-7: Vertical temperature error covariances with respect to the reference grid point at $0^\circ E$, $60^\circ N$ and 30 km altitude with three levels of localization : an unlocalized case (red), a weakly-localized case where vertical decorrelation is set at 10 scale heights (green) and a severely-localized case where vertical decorrelation is set at 2 scale heights (blue). Covariances sampled from the IGCM-FASTOC model.

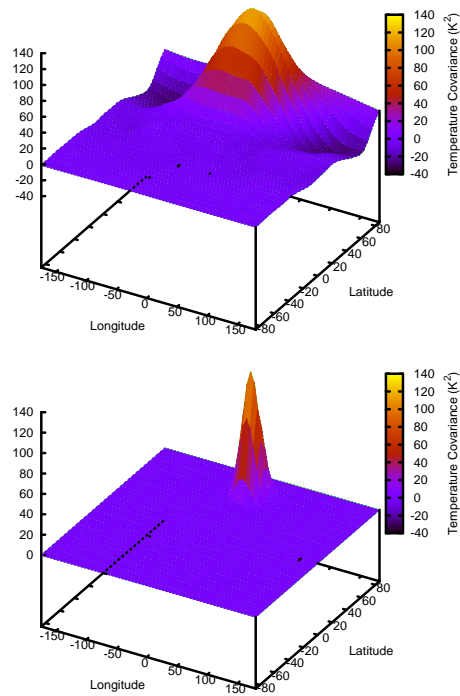


Figure 1-8: Horizontal temperature covariance surface map with respect to the same reference grid point as in Fig 1-7 for an unlocalized case (top figure) and a severely-localized case with horizontal decorrelation set at 2800 km (bottom figure). Covariances sampled from the IGCM-FASTOC model.

practical solution than increasing the number of ensemble members, in terms of tradeoff between analysis quality and computational cost. Covariance localization is generally applied separately in the horizontal and vertical directions. Anderson (2007b) argued that a covariance localization based only on physical distance is quite ad hoc, and a single decorrelation length parameter for all types of covariances is probably not appropriate. Different autocovariances may have specific decorrelation lengths (e.g., temperature-temperature versus ozone-ozone covariances in the stratosphere; Liu et al., 2009). Cross covariances may not have a decreasing value with distance (e.g., wind-geopotential height covariances), and applying covariance localization in such cases creates imbalances in the analysis (Kepert, 2009). Imbalances due to imposed covariance localization have also been witnessed by Mitchell et al. (2002) and explained in Lorenc (2003). A way to reduce these imbalances is to provide a decorrelation length parameter longer than the actual variable decorrelation length (Oke et al., 2007). This may be seen in Figure 1–7 where imposing severe vertical localization (2 scale heights in the vertical, blue curve) changes the sample covariance structure (red curve), whereas a more relaxed localization (10 scale heights, blue curve) smoothes out far away grid points while retaining the general covariance function shape reflected by the covariances. The same can be witnessed in Figure 1–8 for the two-dimensional horizontal plane, where the localized error covariances (bottom figure) are confined to a small radius of effect, compared to the sample error covariance structure (top figure). Other, less ad hoc, methods of localization have been proposed, like the hierarchical ensemble filter of Anderson (2007b) or the ensemble covariances

raised to a power (ECO-RAP) of Bishop and Hodyss (2007, 2009a,b). However, the computational cost of these methods is still prohibitive for implementation in high-dimensional models.

In EnSRFs, another approach is usually adopted, called “local analysis” (Ott et al., 2004). It consists in obtaining the analysis at every grid point individually, by assimilating all observations within a physical volume around the grid point. The rationale behind this is that the local error is evolving in an error subspace much smaller than the full model space. By confining the analysis to this reduced error subspace, the ensemble subspace is more likely to capture the full error growth, the local error covariance matrix will therefore be near or at full-rank. The local analysis has been tested in a idealized setting (Szunyogh et al., 2005) and also showed good results when the local Ensemble Transform Kalman Filter (LETKF) was implemented with the NCEP GFS model (Szunyogh et al., 2008). As in covariance localization, the local analysis technique requires proper specification of the local volume dimensions to obtain accurate results. Sakov and Bertino (2010) actually expect similar performances by covariance localization and local analysis from their analytical study.

Based on the choice of the stochastic EnKF for this study, covariance localization will be applied. The related necessary sensitivity study on the localization parameters is presented in Chapter 2.

Time extension. Observations are not uniquely available at synoptic times (00Z, 06Z, 12Z, 18Z) where NWP analyses are calculated. Satellite observations are an example as they are continuously produced.

In 4D-Var, the TLM implicitly propagates error covariances up to the observation time and its adjoint propagates analysis increments from the diverse observation times back to the analysis time. The EnKF is instead strictly a sequential process with each observation set at a new time requiring a new update. This obviously can prove extremely impractical and costly. It is therefore convenient to extend the instantaneous assimilation time window in the EnKF to be able to assimilate *asynchronous* observations (i.e., measured at times other than the analysis time). This is possible by using a Smoother approach that uses time-lagged error covariances. Error covariances are calculated from an ensemble of background states at analysis and observation time and can consequently propagate the information from an (asynchronous) observation at a posterior time to the analysis. Assimilation of (asynchronous) posterior observations can then be implemented to constrain the analysis. For linear error growth and a perfect model, the analysis obtained from the assimilation of asynchronous observations with time-lagged error covariances and synchronous observations with regular (EnKF) error covariances are equivalent (Sakov et al., 2010). In such conditions, the Smoother is also equivalent to 4D-Var but does not necessitate the TLM and its adjoint. Assimilation of asynchronous observations has notably been successfully tested on the NCEP reduced-resolution GFS model with the 4D-LETKF (Hunt et al., 2007).

Model errors. Another suboptimality of the EnKF arises from the fact that model errors (η in Eqn. (1.2) and their error covariances \mathbf{Q}) are generally not well known and not well represented in \mathbf{Q} . Only forecast errors originating

from misspecification in initial conditions are explicitly considered in this study. In other words, the EnKF only accounts for the internal variability of the model and not the real capacity of the model to portray the system replicated. As seen in Section 1.1.3, models have biases in the stratosphere which need to be accounted for or compensated, or else the variance in the background-error covariance is likely to be underestimated. Different techniques to account for model errors in an EnKF are described and compared in Houtekamer et al. (2009). Another possibility is to use bias-removal approaches as explained by Baek et al. (2006). In this specific study, the model is perfect by experimental design and therefore does not suffer from any model error. This is a typical assumption for idealized studies to test the quality and potential of a data assimilation system.

1.2.3 Stratospheric Applications

Stratospheric ensemble data assimilation is currently implemented in only a few NWP ensemble prediction systems (see Table 1–1). Whereas the traditional technique to initialize the EPS was to perturb the analysis state with singular or bred vectors (Kalnay, 2006), ensemble data assimilation analyses are proving increasingly useful. 24-member deterministic LETKFs are used both at the United Kingdom Meteorological Office (Met Office; Bowler and Mylne, 2009) and at the Korean Meteorological Agency (KMA), with model having lids at 0.01 hPa. Environment Canada (EC) uses a stochastic EnKF with 4 subensembles of 48 members to provide initial conditions for the EPS having a model lid at 2 hPa. The inclusion of the stratosphere in these operational systems is however still quite recent and no peer-reviewed evaluations of the stratospheric products have been

published. Arguably, though, the implementation of stratospheric ensemble data assimilation in operational settings requires that a certain quality and success must first be achieved during the pre-implementation research.

Ensemble data assimilation is also used in the ALERA and NOAA-20CR reanalyses. They respectively use a 40-member LETKF and a 56-member EnSRF, but the model lids at 10 hPa in both reanalyses is too low to reach meaningful conclusions about the stratospheric state. We really wish to point out the fascinating NOAA-20CR project, where high-accuracy reanalyses of the atmosphere are achieved from the sole assimilation of surface observations (Compo et al., 2011). This shows that the 56-member EnSRF is able to efficiently transfer the information from the surface to the whole modeled atmosphere through its forecast-error covariances. As pointed out previously, there is a lack of intercomparison studies evaluating the quality of the stratospheric dynamics in the various reanalyses. The task is complicated by the insufficient source of in-situ unbiased data in the stratosphere for proper validation of stratospheric ensemble data assimilation products.

No interactive ozone is included in any of these operational ensemble data assimilation systems. To the best of the author's knowledge, no other projects have attempted stratospheric chemical-dynamical ensemble data assimilation, except for this study. Guidance in this project must then be extrapolated from other (non-ensemble) data assimilation systems having specific focus on the stratosphere.

Stratospheric Dynamical Data Assimilation. Few assimilation experiments have been attempted with middle atmosphere models that include interactive chemistry (i.e., CCMs). The first notable one was performed with the the Canadian Middle Atmosphere Model Data Assimilation System using a 3D-Var system (CMAM-DAS; Polavarapu et al., 2005a). The assimilation of operational in-situ and satellite dynamical data (no ozone assimilation) produced analysis temperature and wind products that compared on average to within 1 K and 2 m.s^{-1} with radiosondes at 70 hPa. They also had similar accuracy than EC operational analyses, which is surprising considering the difference in model complexity. The analyzed temperatures and winds adjust the ozone field during the forecasts through chemistry and transport, but ozone column values still present biases. From this experiment, conclusions on the challenges that stratospheric data assimilation incurs were drawn (Polavarapu et al., 2005b).

Multivariate (temperature-wind) error covariances are essential to obtain wind analysis increments in the stratosphere. In the absence of flow-dependent error covariances, “balance operators” are often implemented instead in data assimilation systems but represent only the time-averaged large-scale dynamical balances. Model errors may also impair the quality of multivariate dynamical error covariances. Satellite instrument biases are also present but hard to remove considering the lack of independent unbiased observations (e.g., radiosondes). Both the biased stratospheric temperature observations and the misspecified temperature-wind error covariances are likely to produce spurious wind increments and create unbalanced analyses. The next model forecast starting from those

unbalanced initial conditions will try to bring the state back to dynamical balance either through a smooth decay or by converting the excess energy into a fast mode, with gravity-wave excitation (Anderson and Anderson, 1999; Neef et al., 2006). Gravity waves can be a significant source of spurious noise in the modeled stratosphere, in fields like divergence and vertical velocity (Polavarapu et al., 2005b). Note that Polavarapu et al. (2005a) use a stationary background error covariance matrix calculated from a technique called “6-hour time differences”. Flow-dependent ensemble forecast-error covariances might generate less imbalance (even when ignoring the impact of model errors).

The topic of vertical propagation of information in stratospheric data assimilation systems is interestingly seen from a comparison of the Navy Global Atmospheric Prediction Operational System Advanced Level Physics and High Altitude (NOGAPS-ALPHA; Hoppel et al., 2008) and the CMAM-DAS (Ren et al., 2011) simulations of the 2006 stratospheric sudden warming. They both obtain a similar analysis of the stratopause evolution, but the CMAM-DAS does not assimilate any observations above 1 hPa, whereas NOGAPS-ALPHA assimilate limb-sounding MLS and SABER temperature data up to 0.01 hPa. Vertical correlation in the background error covariances are the only way to constrain the upper regions during the data assimilation step if no data are assimilated. However, the static and noisy vertical correlations along with the increasing variances with decreasing pressure in the middle atmosphere may not transfer information upwards appropriately (Polavarapu et al., 2005a). Also, the temperature variability increases exponentially above 40 hPa from the predominance of (real) gravity waves

and so the model forecast will be highly uncertain. A trade-off needs to be made between either transferring spurious increments to the upper stratosphere or setting the covariances to zero and relying on a highly variable forecast unconstrained by observations. The vertical covariances are actually set to zero in CMAM-DAS but the analyzed lower stratospheric winds allow the non-orographic GWD to improve the stratopause region during the forecast step (Ren et al., 2008, 2011). The CMAM-DAS example shows that in addition to corrections to dynamical fields during the analysis step, the forecast step can also improve the stratospheric ozone or dynamical fields. The separate impact of the forecast and analysis steps to constrain stratospheric state is a topic of interest in Chapters 3 and 4.

Stratospheric Chemical Data Assimilation. Stratospheric chemical data assimilation has generally been attempted in CTMs to constrain the tracer concentration fields with satellite observations. Variants of the sequential KF have often been the filters of choice (Ménard et al., 2000; Khattatov et al., 2000; Chipperfield et al., 2002; Baier et al., 2005) but require simplified formulations of the background error covariances considering the high number of chemical species represented in CTMs. The specification of correlations can either be simply isotropic or anisotropic if a dependence on the background field is included in the correlation model (Riishøjgaard, 1998). In the case of isotropic correlations, their propagation with the TLM introduces flow-dependence and anisotropy, but there is spurious loss of variance and increase in correlation lengths with successive propagation and assimilation steps (Ménard et al., 2000). Tunable error growth, correlation length and observation error parameters can be implemented

to retain reasonable background and observation error covariances (Ménard et al., 2000; Khattatov et al., 2000). Another simplification for most CTM data assimilation schemes is the use of univariate covariances. However, as stated by Chipperfield et al. (2002), the constraint on a given observed variables should not be detrimental to the overall state of the system. In chemical weather, that implies keeping intact the “compact correlations” between long-lived tracers (Plumb and Ko, 1992) following assimilation and also respect the overall abundance of each species. To preserve correlations between species, Chipperfield et al use calculated pre-assimilation compact relationships between different tracers (e.g., CH₄ and NO₂) and constrained the unobserved tracers (e.g., NO₂) from those analyzed (e.g., CH₄) post-assimilation. Good accuracy in observed and unobserved species was obtained when compared to independent observations. This technique is very similar to the multivariate constraint in the EnKF, except that the correlations in the EnKF are obtained from a sample of forecasts, as opposed to a single forecast in Chipperfield et al. A better statistical confidence in the correlations is thus achieved in the EnKF technique, further supporting its use.

The use of CTMs to forecast ozone is sometimes the strategy adopted operationally. For example, GMAO opted for an offline CTM driven by the GEOS-5 analysis winds to forecast ozone. They assimilate ozone columns from SBUV/2 and TOMS, and profiles from MIPAS (Stajner et al., 2001; Wargan et al., 2005). Again, only autocovariances are used when assimilating ozone observations. Even in cases where ozone fields are coupled to meteorological fields, chemical-dynamical multivariate balances are hard to specify analytically. A possibility is to use a

4D-Var setup, keep univariate background error covariances and let the adjoint of the TLM propagate analysis increments from the observed variable to unobserved ones. The first of such setups was developed by Fisher and Lary on a trajectory box model with assimilation of O_3 and NO_2 (Fisher and Lary, 1995). Generally, 4D-Var for chemical data assimilation is much more time-consuming than the KF filters described above, but it does permit to constrain unobserved species from observed ones if they interact chemically on timescales shorter than the assimilation window (Lahoz et al., 2007). The ECMWF has adopted this approach in their NWP models coupled to linearized ozone scheme (Dee et al., 2011).

Stratospheric Chemical-Dynamical Data Assimilation. Stratospheric dynamical data assimilation and chemical data assimilation have all been attempted independently, but the intersection of both is still rare. The properties of ensemble data assimilation make it a powerful tool to attempt and possibly achieve stratospheric chemical-dynamical data assimilation. The case of ozone assimilation impacting dynamical variables is particularly interesting. It has occasionally appeared in the data assimilation literature beginning in the mid-1990's and has been largely untreated afterwards, until very recently. The first instances were with Daley (1995) and Riishøjgaard (1996), who both separately looked at the possibility of determining the wind flow from tracer concentrations during the data assimilation step. Daley worked with a simple 1D advection model and EKF assimilation of passive tracer observations. He concluded that it is possible to determine the flow provided that observations are accurate and not too sparse in space and time. Riishøjgaard (1996) tested the assimilation of ozone column data

in a 4D-Var and found similar results in terms of data requirements. A much more recent experiment by Semane et al. (2009) found noticeable wind improvement in the lower stratosphere when assimilating MLS ozone profiles in a complex NWP 4D-Var system coupled to a CTM. All these experiments have in common that the coupling between the ozone and wind is done through the TLM and its adjoint rather than through explicit specification of the tracer-wind error covariances. The 4D-Var system of Semane et al. (2009) has univariate ozone covariances therefore ozone analysis increments can only be transferred to the winds during the backward propagation by the TLM adjoint. An example of successful tracer-wind relation through error covariances has been achieved in an LETKF system by Miyazaki (2009). It is however in the reverse direction that it has been achieved as the meteorological assimilated observations are shown to provide a good constraint on the long-lived CO₂ field through the wind-CO₂ cross-variable error covariances. This indicates that some transport information can be adequately captured in ensemble error covariances.

Based on knowledge of stratospheric dynamics and chemistry, a few comments may be given regarding the possibility of deducing the wind field from tracer transport. The first one is the necessity to have gradients in the tracer field, as pointed out by both Daley (1995) and Riishøjgaard (1996). The task is likely to be difficult in the upper stratosphere where the short chemical lifetime of ozone tends to homogenize the concentrations. It is more likely in regions of shorter-timescale chaotic advection, provided that tracer gradients do not align with wind field (i.e., be orthogonal to wind gradient) (Shepherd, 2000). Zagar et al. (2004) also point

out that recovery of one variable from observations of another may be difficult in the tropics, where the statistical coupling between mass and wind fields is weak due to the low Coriolis force. These considerations are based mostly on a pure advection perspective, it would be interesting to see if ensemble covariances can capture some more complex relation involving photochemistry as well in regions where the chemical and dynamical timescales are of the same order of magnitude. The purely photochemical temperature-ozone correlations could also permit a multivariate constraint in the upper stratosphere (Polavarapu et al., 2005b).

1.3 Methodology and Aim of Thesis

1.3.1 IGCM-FASTOC Model

A description of the CCM used in this study, the Intermediate General Circulation Model (IGCM) coupled to the FAsT STratospheric Ozone Chemistry schemes (FASTOC) (Taylor and Bourqui, 2005), is provided here. The dynamical part of the model is based on the spectral core of Hoskins and Simmons (1975), with centered-difference time-stepping. The particular version of the CCM used in this study has horizontal truncation at wavenumber 21 with 26 vertical levels and a model lid at 0.1 hPa (T21L26[0.1 hPa]), and 64 daily timesteps. This represents a horizontal resolution of about 5.6° . The model is discretized into terrain-following vertical σ levels, such that the pressure P at a given level σ is $P = \sigma \times P_s$, where P_s is the surface pressure variable. Of the 26 vertical levels, 15 of them are above the 200 hPa pressure level. The general spacing between stratospheric levels is between 2.5 km near the tropopause to 4 km near the stratopause. The physical parametrization does not include any orographic or non-orographic gravity-wave

drag. Instead, Rayleigh friction is imposed in the top five levels of the model, above 4 hPa.

While the dynamical part of the CCM presents simple configurations compared to other CCM (see Section 1.1.3) it still presents acceptable long-time averaged performances (Bourqui et al., 2005). Its particular advantage is its simulation speed, even when including the FASTOC chemistry scheme. The FASTOC uses a technique called Fully Equivalent Operational Models (FEOM) with cut High Dimensional Model Representations (cut-HDMR) developed by Rabitz and Alis (1999) (details in Taylor and Bourqui, 2005). It essentially represents the chemical nonlinear ordinary differential equations for each specie in terms of series of correlation functions with other variables, centered around a reference point in state space. The functions are calculated by sampling the state space of a full chemical box model and stored in look-up tables. The technique retains the nonlinear aspect of the reference box model, in our case the one by Fish and Burton (1997). In that respect, it is closer in nature to a comprehensive box model, as in other CCMs, than it is to a linearized ozone scheme like the one by Cariolle and Teyssèdre (2007) used in the ECMWF models. The FASTOC calculates the chemical increments explicitly for the following chemical tracers and families of tracers: the ozone family (or odd oxygen) $O_x = O_3 + O(^1D) + O(^3P)$, odd nitrogen $NO_x = NO + NO_2 + NO_3 + HONO$ and its reservoir species N_2O_5 and HNO_3 . In addition to the Chapman mechanism for O_x , and the NO_x catalytic cycle, the FASTOC also implicitly calculates the HO_x catalytic cycle. The input variables to the FASTOC include H_2O , N_2O , CH_4 , CO , CO_2 , CFC – 11 and CFC – 12, all

prescribed from climatology, as well as temperature T , pressure P and the four active chemical tracers. The chemical increments are calculated in twelve different stratospheric regions (reference points; see Table 1 of Taylor and Bourqui, 2005) to provide good stability for the FASTOC. As previously mentioned, chlorine and bromine heterogenous chemistries responsible for polar ozone depletion are not calculated. Methane oxidation is not represented implying that upper stratospheric water vapor fields have a low bias and are not reliable. FASTOC produces diurnally-averaged daily chemical increments for the four active tracers at 00Z and adds them linearly at each timestep over the next 24 hours. Overall, FASTOC achieves a speedup of about 10^3 with respect to the original box model.

The interactive ozone is advected according to a spectral multilayer horizontal Euler scheme and is an input to the Morcrette radiation scheme (Morcrette, 1991). The other input gases for the radiation scheme are prescribed from climatology: H_2O , N_2O , CH_4 , CO_2 , CFC – 11 and CFC – 12. The radiative increments are also calculated every 24 hours at 00Z and added at every timestep based on the prescribed radiative timescales.

All model simulations were performed on Hydroxyl: a cluster of 32 Itanium 2 64-bit architecture CPUs with 1.5 GHz and 96 GB shared memory. For reference, an ensemble of 128 24-hour forecasts simulated in parallel on 16 processors is performed in a wall-clock time of about 6 minutes.

1.3.2 EnKF Filter Configurations

The state vector in the IGCM-FASTOC EnKF assimilation system is the following:

$$\mathbf{x} = (\mathbf{u}, \mathbf{v}, \mathbf{T}, \mathbf{q}, \mathbf{O}_x, \mathbf{N}_2\mathbf{O}_5, \mathbf{NO}_x, \mathbf{HNO}_3, \mathbf{P}_s)^T$$

consisting of nine subvectors representing the nine variables output by the model, each containing all the model grid points. The variables are respectively the three-dimensional zonal wind, meridional wind, temperature, specific humidity, odd oxygen, dinitrogen pentoxide, odd nitrogen, nitric acid and the two-dimensional surface pressure. Pressure (or geopotential height) is not included in the state vector considering that pressure can be easily derived at a given σ level from the surface pressure. Each 3D vector of variables holds 64 longitudes, 32 latitudes and 26 levels (owing to the T21L26 model resolution) and the surface pressure vector is on a single level and therefore only holds 64 longitudes and 32 latitudes. The total amount of model state grid variables is $n = 8 \times 64 \times 32 \times 26 + 1 \times 64 \times 32 = 428032$.

The stochastic version of the EnKF has been chosen based on the arguments by Lawson and Hansen (2004) that it has a better behavior in nonlinear contexts. The Double-EnKF technique of Houtekamer and Mitchell (1998) is used with 2 ensembles of 64 members (based on the results by Mitchell et al., 2002). No covariance inflation is imposed based on posterior diagnostics seen in Chapter 2. Covariance localization based on physical distance is applied in this study and optimal parameters are obtained from a sensitivity study, to remove spurious sampling noise and increase the rank of the error covariance matrix.

The total duration of an assimilation of the 7392 daily stratospheric observations (corresponding to the MIPAS network in this study) with 16-processor parallelization of computationally-expensive matrix manipulations is about 75 minutes.

1.3.3 Aim of the Thesis

The choice of testing Ensemble Kalman Filter data assimilation with the IGCM-FASTOC CCM is motivated by the absence of precedence, and in that respect the application of an EnKF to a CCM is a breakthrough. The possibility to develop such a system is circumstantial, as it requires the availability of a CCM fast enough to simulate large ensemble of forecasts. It is also permitted by the relative ease in implementation of the EnKF. This allowed to construct a full data assimilation system from scratch over the course of a doctoral study. These conditions provided the opportunity to profit from the EnKF property of estimating flow-dependent error covariances to study the interaction between chemistry and dynamics in the stratosphere.

This study consists in a first attempt at performing ensemble data assimilation with a CCM. As this is a newly developed system, it is essential to follow a rigorous sequence of tests to make sure that the data assimilation system is robust. To achieve this task, an Observation System Simulation Experiment (OSSE) is designed. It allows to test the stability and basic performance of the data assimilation system in a controlled environment. The first step involves performing a perfect-model (or identical-twin) OSSE (e.g., Houtekamer and Mitchell, 1998; Liu and Kalnay, 2007). This implies the assumption that the model is perfect ($\eta = 0$

in Eqn. (1.2) and $\mathbf{Q} = \langle \eta\eta^T \rangle = 0$) and the process for such an experiment is as follows. A model simulation represents the true state of the atmosphere, from which observations are sampled. These artificial observations can be assimilated to a different forecast (or ensemble of forecasts in the case of ensemble data assimilation systems) from the same model as if they were real observations. The advantage of OSSEs is that, unlike in assimilation experiments with real observations, the truth is known therefore it is possible to evaluate if the analysis converges towards the right solution. In ensemble data assimilation systems, this is typically done by calculating the root-mean-square error (RMSE) of the ensemble mean with respect to the true state. The RMSE diagnostic expresses the *accuracy* of the EnKF solution and should be compared to the root-mean square difference between the ensemble members and the ensemble mean (SPREAD) to estimate the *reliability* of the EnKF solution (Sacher and Bartello, 2009). The SPREAD is essentially the standard deviation of the ensemble and equality between the SPREAD and the RMSE must be witnessed for the EnKF solution to be consistent. An accurate and reliable EnKF solution would imply that suboptimalities linked to sampling error or nonlinearities in the prior distribution are suitably accounted for and do not overwhelmingly degrade the analysis. A small SPREAD in conjunction with a large RMSE is a typical example of potential filter divergence. The reverse case expresses an overly dispersive ensemble and therefore the inability of the EnKF to determine its real accuracy. As a consequence, observations would receive too much weight at the expense of the model.

If successful behavior is obtained from the assimilation filter in a perfect-model OSSE, the next step is to perform imperfect-model (non-identical twin) experiments, where the true state is again known, but is now a simulation from a different version of the model (fraternal-twin OSSE) or preferably an altogether different model. This introduces model errors in the assimilation system that need to be accounted for. The ultimate step is the assimilation of real observations. Note however that the objective of this study is not to evaluate the assimilation impact of a future observation source as is often the goal in OSSEs. The infrastructure in such OSSEs is more complex and are attempted with already calibrated data assimilation systems (see for example the OSSE evaluating the potential of assimilating Doppler Wind Lidar data in the NCEP system of Masutani et al., 2010). The intent of the OSSE in this study is rather to calibrate the ensemble data assimilation filter and study its properties.

In ensemble data assimilation systems, error covariances between all possible pairs of state variables are calculated statistically. Through these, an observation can influence any state variable (except in the unlikely case where the calculated error covariance is exactly zero) during the analysis step. This includes impacting the observed variable spatially through autocovariances, as well as impacting other unobserved variables spatially and multivariately through cross covariances. Even after localization, a certain proportion of error covariances remain non-zero and it is possible to investigate how the information from given observations constrain the model state. As many stratospheric data assimilation systems are very complex and assimilate a large amount of observations, it is difficult to sense

the impact of a particular kind of observation. Techniques such as “observations impact” (Lupu et al., 2011) give the relative impact of a type of observations in the observing system, but it hardly illustrates its spatial and physical impact. At the other end of the spectrum, single-observation experiments achieve this task (see for example Buehner et al., 2010a), but do not realistically present the global impact of an observation type. In this study, only a single type of observation, either limb-viewing satellite ozone or temperature retrievals, is assimilated during an experiment to determine its effect on other variables. No conventional data are assimilated so as to look only at the absolute impact of the assimilated observation type and not the impact relative to the rest of the observing system. In particular, following the pioneering work of Daley (1995) and Riishøjgaard (1996), the possibility of constraining the stratospheric winds when assimilating ozone observations is a main focus of investigation.

The studies in this thesis are restricted to perfect-model OSSEs because, in addition to testing the stability of a filter (Chapter 2), this type of experiment also provides an overview of the maximum potential of the filter to constrain the atmosphere given an observing system. The specific focus of this study is to determine the ability of ensemble-calculated background multivariate error covariances, including chemical-dynamical ones, to transfer information from observations to the model state, in a variety of contexts. In particular, the relation between the assimilation of stratospheric ozone observations and their effect on the dynamical and chemical model variables is investigated in Chapter 2, and conversely the assimilation of stratospheric temperature observations

and their effect on the chemical and dynamical variables. This includes both the direct impact during the analysis step and the corrections to the analysis increments in the ensuing forecast. Further analysis/forecast dissection in the inter-variable relations is investigated in Chapter 3 to characterize the specific impact of assimilating different types of observations during the analysis step. Also, imposing a true state by experimental construct allows to further test the assimilation filter in order to investigate its possibilities and limits. Experiments in Chapter 2 are exclusively attempted with synchronous observations regularly available every 24 hours, even if the observation sequence in the real atmosphere is much more complex. Consequently, Chapter 3 answers some questions regarding the treatment of observations spread over time and particularly the potential of asynchronous observations to further constrain the analysis. We may also test the EnKF response to various true states of the atmosphere. A self-generated stratospheric sudden warming is chosen as true state in Chapter 4 to determine if strong initial forecast deviations prevent the filter from behaving appropriately. Chapter 4 also allows to verify the potential of obtaining an accurate wind analysis from the assimilation of stratospheric ozone observations, which is the main objective of this doctoral thesis.

CHAPTER 2

Assimilation of Stratospheric Temperature and Ozone with an Ensemble Kalman Filter in a Chemistry-Climate Model

The second chapter of this study describes the implemented ensemble data assimilation system that includes atmospheric dynamics and stratospheric ozone chemistry. In particular, the Ensemble Kalman Filter assimilation of synthetic ozone or temperature data mimicking limb-sounding satellite retrievals into the IGCM-FASTOC chemistry-climate model is performed in a perfect model observation system simulation experiment context. A sensitivity study on the covariance localization is accomplished to determine optimal parameters needed for ozone and temperature assimilation to reduce the global model state error. With an optimized EnKF system, the interaction between the chemical and dynamical model states is investigated during the forecast and the assimilation steps.

This chapter is based on the following paper: Milewski, Thomas and Michel S. Bourqui, 2011, Assimilation of Stratospheric Temperature and Ozone with an Ensemble Kalman Filter in a Chemistry-Climate Model. *Monthly Weather Review*, **139**, 3389–3404. doi: <http://dx.doi.org/10.1175/2011MWR3540.1>

©American Meteorological Society. Reprinted with permission.

Assimilation of Stratospheric Temperature and Ozone with an Ensemble Kalman Filter in a Chemistry-Climate Model

Thomas Milewski and Michel Bourqui

Department of Atmospheric and Oceanic Sciences, McGill University

Montréal, Qc, Canada

Abstract

A new stratospheric chemical-dynamical data assimilation system was developed, based upon an Ensemble Kalman filter coupled with a Chemistry-Climate Model [i.e., the intermediate-complexity general circulation model with Fast Stratospheric Ozone Chemistry (IGCM-FASTOC)], with the aim to explore the potential of chemical-dynamical coupling in stratospheric data assimilation. The system is introduced here in a context of a perfect-model Observing System Simulation Experiment. The system is found to be sensitive to localization parameters and in the case of temperature (ozone) assimilation yields its best performance with horizontal and vertical decorrelation lengths of 14 000 km (5600 km) and 70 km (14 km). With these localization parameters, the observation-space background-error covariance matrix is under-inflated by only 5.9% (over-inflated by 2.1%) and the observation-error covariance matrix by only 1.6% (0.5%), which makes artificial inflation unnecessary. Using optimal localization parameters, the skills of the system in constraining the ensemble-average analysis error with

respect to the true state is tested when assimilating synthetic Michelson Interferometer for Passive Atmospheric Sounding (MIPAS) retrievals of temperature alone, and ozone alone. It is found that in most cases background-error covariances produced from ensemble statistics are able to usefully propagate information from the observed variable to other ones. Chemical-dynamical covariances, and in particular ozone-wind covariances, are essential in constraining the dynamical fields when assimilating ozone only, as the radiation in the stratosphere is too slow to transfer ozone analysis increments to the temperature field over the 24-h forecast window. Conversely, when assimilating temperature, the chemical-dynamical covariances are also found to help constrain the ozone field, though to a much lower extent. The uncertainty in forecast/analysis, as defined by the variability in the ensemble, is large compared to the analysis error, which likely indicates some amount of noise in the covariance terms, while also reducing the risk of filter divergence.

2.1 Introduction

Stratospheric ozone is a major component of the atmospheric system. Its radiative budget shapes the vertical temperature profile in the middle-atmosphere and affects the wind patterns seasonally and regionally. The modeling and assimilation of stratospheric ozone in atmospheric General Circulation Models (GCM) is essential. It can produce better UV or ozone hole forecasts (Brasseur et al., 1997), help improve satellite retrieval algorithms (Stajner et al., 2001) and allow for a better representation of the stratospheric dynamics, which eventually influence the tropospheric weather (Charlton et al., 2004). In addition, long-term ozone reanalysis are useful to help improve our knowledge of the (chemical) climate.

Most meteorological centers now include the whole stratosphere and part of the mesosphere in their operational models [e.g., the European Centre for Medium-Range Weather Forecasts (ECMWF) and the National Aeronautics and Space Administration (NASA) Goddard Global Modeling and Assimilation Office have their model lid at 0.01 hPa (ECMWF : European Centre for Medium-Range Weather Forecasts, cited 2012; Rienecker et al., 2008), and Environment Canada at 0.1hPa (EC : Environment Canada, cited 2012)], but including a complete ozone chemistry with assimilation of the chemical species on top of the standard dynamical assimilation is still computationally too expensive. Currently, stratospheric chemical-dynamical data assimilation is being investigated on board research models, like three-dimensional Chemistry-Transport Models (CTMs; e.g., Miyazaki, 2009), or with Chemistry-Climate Models (CCM; Lahoz et al., 2007).

Most current stratospheric chemical-dynamical data assimilation schemes use variational schemes (Polavarapu et al., 2005a). Such schemes are able to constrain the ozone analysis and moderately improve the following temperature or wind forecasts, either through the radiation scheme [as in the three-dimensional variational data assimilation (3D-Var) setup of de Grandpré et al. (2009)] or through the tangent-linear tracer-advection equation and its adjoint during the four-dimensional variational data assimilation (4D-Var) iterations (Semane et al., 2009). However, there is potential during the data assimilation analysis step for constraining the dynamics from ozone observations directly through the background-error covariances.

Ensemble data assimilation schemes, like the Ensemble Kalman Filter (EnKF; Evensen, 1994), have the particularity of producing along-the-flow background-error covariances. These include the forecast random errors at a given time and location (variance part), as well as information on how errors covary spatially (autocovariance), among different variables (cross covariance) and even temporally (if the state vector includes more than one time step). Recently, ensemble data assimilation schemes have been applied to several atmospheric models. Houtekamer et al. (2005) were the first to implement EnKF data assimilation on an operational numerical weather prediction suite. Their low 10 hPa model top makes it difficult, however, to reach meaningful conclusions about their stratospheric analyses. Szunyogh et al. (2008) and Whitaker et al. (2008) tested their ensemble data assimilation filters [the local ensemble transform Kalman filter (LETKF) and a variant with serial processing of observations, respectively, both being flavors

of ensemble Kalman square root filters, described in Section 2.3] with a reduced-resolution version of the National Centers for Environmental Predictions (NCEP) Global Forecasting System (GFS) with a top at 3 hPa, therefore encompassing more of the stratosphere. The systems both showed generally similar performance than the 3D-Var and Spectral Statistical Interpolation (Parrish and Derber, 1992; Derber and Wu, 1998) schemes, except for a notable improvement in data-sparse regions. This result is very interesting since it indicates the potential of ensemble covariances to transfer information from the observation to (covarying) regions, knowing that the stratosphere is sparsely observed by satellites, global positioning system (GPS) radio occultation or aircraft data. By extension, the information could also be transferred to other variables, like winds.

These high-resolution models do not include stratospheric chemistry yet. Ensemble chemical-dynamical assimilation has been applied on CTMs in the troposphere (van Loon et al., 2000; Constantinescu et al., 2007). These studies suggest that the assimilation system improves the observed chemical variables analyses but do not investigate the impact on other variables, including chemical ones. Miyazaki (2009) found that his LETKF can further improve the analysis of the long-lived tracer carbon dioxide (CO_2) in the troposphere and the stratosphere through the covariances between wind and CO_2 . However, in a CTM framework where winds are imposed by meteorological analyses, as opposed to CCMs where chemistry, radiation and dynamics interact, the transfer of information from the chemical to the dynamical variables during the EnKF analysis phase can not be achieved. Arellano Jr. et al. (2010) explored ensemble data assimilation using

a CCM, but did not investigate the full potential of chemical and dynamical interplay, only the effect of assimilating carbon monoxide observations on black carbon simulation.

This paper presents a newly-developed stratospheric system combining a CCM and ensemble data assimilation and explores its main properties. The first step of this study is to test the stability of the system in a “twin experiment” context, i.e., with a model run identified as the true state, from which the observations are derived by adding random perturbations, and to which the ensemble of forecast/analyses are compared. An important aspect of this first step is the sensitivity to covariance localization, since this parameter reduces the effects of rank deficiency and helps prevent filter divergence (Hamill et al., 2001). Furthermore, a clear understanding of how the localization affects the filter is currently lacking, particularly in a multivariate context with non-zero cross covariances. Other parameters of the EnKF are discussed in Section 2.3.2.

The second step is to explore the properties of the information transfer from the observations to the analysis through the ensemble covariances. Particular emphasis is placed on assimilation of ozone mixing ratios and its effect on temperature and winds, following the ideas of Daley (1995). Observations of winds are rare in the stratosphere. Thus a better constraint of the motion resulting from assimilating temperatures or ozone mixing ratios would be of great interest (Semane et al., 2009). The ensemble assimilation approach directly gives forecast-error covariances, which greatly reduces the underlying assumptions on the structure of the covariances, both spatially (Ménard et al., 2000) and between variables

(Chipperfield et al., 2002), and removes the dependence of statistics on climatology (Polavarapu et al., 2005a).

The feasibility of this enterprise relies on the possibility to perform $\mathcal{O}(10^2)$ ensemble forecasts with a CCM and the data assimilation over weekly time scales. Here, this is achievable thanks to the use of the intermediate-complexity general circulation model with Fast Stratospheric Ozone Chemistry (IGCM-FASTOC; Bourqui et al., 2005). The FAst STRatospheric Ozone Chemistry (FASTOC, Taylor and Bourqui, 2005) scheme represents the non-linear ozone catalytic cycles: O_x [odd oxygen family composed of ozone O_3 and single oxygen atoms $O(^1D)$ and $O(^3P)$], HO_x (hydrogen oxide radicals OH and HO_2) and NO_x (nitrogen oxide radicals NO , NO_2 , NO_3 and $HONO$). It however excludes heterogeneous chemistry of chlorine radicals Cl_x (ClO and Cl) and bromine radicals Br_x (Br and BrO). Details on the chemical mechanisms can be found in Chapter 10 of Jacob (1999). Note that this limitation allows faster computations but restrains the scope of this study to non-ozone hole conditions. The type of data assimilation experiments conducted here are perfect-model Observation System Simulation Experiment (OSSE; e.g., Lahoz et al., 2005). Synthetic observations mimic limb-viewing temperature and ozone satellite retrieval data in the stratosphere only. No model or observation biases are taken into account and the observational errors are chosen to be spatially uniform. Observations are assimilated a single variable at a time to permit the assessment of the relative success of auto and cross covariances. We also assume that observations are all taken instantaneously at the analysis time. This makes it a three-dimensional problem rather than a four-dimensional

one. This idealized setting allows one to concentrate on this study’s goals without the added complexity related to real observations and model biases, and permits more direct interpretations of the results.

The paper is structured as follows: Section 2.2 provides some details on the EnKF. Section 2.3 describes in details the data assimilation scheme and the experimental setup. Section 2.4 discusses the performance of the assimilation scheme and its sensitivity to localization parameters. The importance of multivariate covariances in propagating information between ozone, temperature and winds is analyzed in Section 2.5. Conclusions are drawn in Section 2.6.

2.2 A Short Review of Ensemble Kalman Filtering

The EnKF data assimilation cycle starts with the forecast step, where an initial condition (\mathbf{x}_k^a) is propagated forward in time for $\Delta t = t_{k+1} - t_k$ with the non-linear model \mathcal{M} , subject to some system noise η :

$$\mathbf{x}_{k+1}^f = \mathcal{M}_k(\mathbf{x}_k^a) + \eta_k \quad (2.1)$$

where \mathbf{x}^f is the model forecast state vector, and \mathbf{x}^a the analysis vector, t is the time. All vectors are of size n , the number of model state variables times the number of grid points. The system noise η is a white unbiased Gaussian noise, and is distinct from the forecast error due to misspecification in initial conditions. In practice, specification of the system noise is difficult and several techniques have been developed to account for it (e.g., stochastic perturbation of model parameters or addition of isotropic noise, Houtekamer et al., 2009). However, under our perfect-model hypothesis, η is assumed to be zero.

The data assimilation cycle is then completed by performing the update step, to produce an analysis that combines the information from the set of forecasts and assimilated observations. We can express the Kalman equations under the form:

$$\delta\mathbf{x} = \mathbf{K}\mathbf{d} \quad (2.2)$$

where

$$\mathbf{K} = \mathbf{P}^f \mathbf{H}^T (\mathbf{H} \mathbf{P}^f \mathbf{H}^T + \mathbf{R})^{-1} \quad (2.3)$$

$$\delta\mathbf{x} = \mathbf{x}^a - \mathbf{x}^f \quad (2.4)$$

$$\mathbf{d} = \mathbf{y} - \mathcal{H}(\mathbf{x}^f) \quad (2.5)$$

Equation 2.2 expresses the analysis increments $\delta\mathbf{x}$, defined as analysis \mathbf{x}^a minus forecast \mathbf{x}^f , as the transformation of the innovations \mathbf{d} by the Kalman Gain operator \mathbf{K} . Innovations are defined as the difference, in observation space, between the observations to be assimilated (\mathbf{y}) and the forecast (\mathbf{x}^f). The (potentially non-linear) observation operator \mathcal{H} maps the n -sized forecast (\mathbf{x}^f) to the p -sized observation space. In the Kalman gain formulation (Eq. 2.3), the observation operator is reduced to its linearized form \mathbf{H} . In a scalar case, the Kalman gain \mathbf{K} (Eq. 2.3) is simply the ratio of the forecast-error variance to the sum of observation- and forecast-error variances.

The observations-error covariance matrix \mathbf{R} is constructed from knowledge on instrumental random errors. Correlations between observations are usually neglected, although for satellite instruments, the broad structure of the weighting functions imply that there is some vertical correlation in the error of the retrieved

quantities. Because of this imperfect specification of \mathbf{R} , we will rather use the notation $\tilde{\mathbf{R}}$ to differentiate it from the perfect observation-error covariance matrix.

The off-diagonal covariance elements of \mathbf{P}^f provide a means for observation information to be transferred to neighboring points and to other variables. This property can only be advantageous if spatial and multivariate balances are properly represented in \mathbf{P}^f . For instance, increments in temperature and winds that are produced by an innovation in temperature need to respect thermal-wind balance, if applicable. However, constructing such a background-error covariance matrix with proper representation of thermo-dynamical balances is a challenge which Monte-Carlo approaches like the EnKF are particularly adapted to address.

In ensemble Kalman filtering, we yield m realisations of the model state and calculate the sample forecast-error covariance matrix \mathbf{P}_e^f as:

$$\mathbf{P}_e^f = \frac{1}{m-1} \sum_{j=1}^m (\mathbf{x}_j^f - \langle \mathbf{x}^f \rangle) (\mathbf{x}_j^f - \langle \mathbf{x}^f \rangle)^T \quad (2.6)$$

The chevrons $\langle \rangle$ denote ensemble average. Note that for simplicity of notation, we have dropped the time index from the model-state vectors, the forecast-error covariance in an EnKF being calculated only at a particular time. Technically, this $(n \times n)$ matrix is used only in forms that are reduced to observation space, such as the $(n \times p)$ and $(p \times p)$ matrices defined by:

$$\mathbf{P}_e^f \mathbf{H}^T = \frac{1}{m-1} \sum_{j=1}^m (\mathbf{x}_j^f - \langle \mathbf{x}^f \rangle) (\mathcal{H}(\mathbf{x}_j^f) - \langle \mathcal{H}(\mathbf{x}^f) \rangle)^T \quad (2.7)$$

$$\mathbf{H} \mathbf{P}_e^f \mathbf{H}^T = \frac{1}{m-1} \sum_{j=1}^m (\mathcal{H}(\mathbf{x}_j^f) - \langle \mathcal{H}(\mathbf{x}^f) \rangle) (\mathcal{H}(\mathbf{x}_j^f) - \langle \mathcal{H}(\mathbf{x}^f) \rangle)^T \quad (2.8)$$

The EnKF system must use perturbed observations in order to avoid losing some directions of error growth (Burgers et al., 1998). Different techniques have been elaborated to bypass observation perturbation and reduce computational cost. These were shown to be conceptually equivalent and are denoted as Ensemble Square Root Filters (EnSRF; Tippett et al., 2003). However, as argued by Lawson and Hansen (2004), the EnSRF transforms the forecast ensemble into the analysis ensemble by retaining the forecast probability density function (PDF) shape. In the presence of non-Gaussian forecast PDF, this may lead to violation of Gaussianity hypotheses of the Kalman filter after a few updates, if non-linearities act to intensify non-Gaussianity. The EnKF, with randomly perturbed observations, behaves better in non-linear situations, since it is able to “repopulate” a Gaussian analysis PDF, even if the forecast PDF is non-Gaussian. This is done thanks to the stochastic combination of forecasts with the normally-distributed unbiased perturbed observations. To allow for the strong non-linear nature of stratospheric dynamics and chemistry, this study is cast in the “perturbed-observations” EnKF framework.

In the standard EnKF, the m forecasts are used to generate \mathbf{P}_e^f and the ensemble of analyses. An improvement to this scheme consists in splitting the ensemble in two sets (or more) and updating the first set with the Kalman Gain calculated from the second set and vice-versa. This technique is called Double-EnKF (Houtekamer and Mitchell, 1998) and is applied here. It has the advantage of preventing “inbreeding” (i.e., updating an ensemble with its own statistical properties) in the filter and a subsequent underestimation of forecast errors. Such

underestimation can lead to filter divergence, a phenomenon where observations are ignored because the Kalman Gain gives more weight to low errors. The analysis becomes identical to the forecast, no matter how inaccurate it can be. This is a particular problem for ensemble Kalman filtering since low forecast errors are transferred to the analysis during the update, but also to the next forecast since analysis members are used as model initial conditions.

Another source of forecast error underestimation, possibly leading to filter divergence, are the sampling errors associated with the limited size of the forecast ensemble. The Ensemble Kalman filter solves the Kalman equations exactly in the limit where an infinite ensemble is used to sample the state space of the model. In practice, with only a limited number of ensemble members, problems of rank-deficiency may occur. An important consequence is that long-range covariances, which should be close to zero, are contaminated by sampling noise, resulting in the spurious propagation of information from the observation point to far-away, uncorrelated, regions. This adds noise to the analysis and degrades the dynamical/chemical balances. Solutions to this problem include reducing the state dimension around the observation points by performing local analysis (i.e., tiling the grid; Ott et al., 2004), or applying a localization function with an elementwise-product on the error covariance matrices (Houtekamer and Mitchell, 2001). Note that there is currently no study comparing the performance of these two methods in the literature, but in principle both of them provide an easy control of the size of the subspace. In this study, we use covariance localization following Houtekamer and Mitchell (2001).

2.3 Experimental Setup and Diagnostics

2.3.1 Experimental Setup

The model is the IGCM-FASTOC (see description in Forster et al., 2000; Taylor and Bourqui, 2005). The model is run with horizontal truncation at T21 (approximately $5.6^\circ \times 5.6^\circ$ horizontal spacing) and 26 σ -coordinate levels reaching up to 0.1 hPa. Fifteen vertical levels are located in the stratosphere, with a vertical resolution approaching 1.5 km near the tropopause and 5 km near the stratopause. The model does not have a gravity-wave drag scheme, but uses Rayleigh friction in the upper 5 levels, above 4 hPa. Note that water vapour production by methane oxidation in the upper stratosphere is not included, which makes specific humidity q merely a passive tracer in the stratosphere. The state vector is composed of eight three-dimensional variables: zonal wind u , meridional wind v , temperature T , specific humidity q , odd oxygen family O_x , nitrogen oxide radicals NO_x and its reservoir species dinitrogen pentoxide N_2O_5 and nitric acid HNO_3 . It also includes the two-dimensional surface pressure P_s . We assume that this set of variables fully describes the state of the model. Note that ozone $[O_3]$ and odd oxygen $[O_x] = [O] + [O_3]$ concentrations are quasi-identical in the stratosphere given the low single oxygen concentration $[O]$, and will be used interchangeably hereafter.

The chemistry scheme is launched every 24h at 00Z, the first dynamical timestep after the analysis (initial conditions) is produced. It calculates daily concentration increments for O_x , NO_x , N_2O_5 and HNO_3 between the tropopause and 4 hPa and applies them linearly at every dynamical timestep through the

24h. These four interactive chemical species are advected by the model and O_x is used by the radiation scheme to calculate diurnal average heating rates that are also applied linearly through the day. The chemistry scheme takes typical physical-chemical variables as input (Taylor and Bourqui, 2005), including the following ones that are of particular interest to this study: temperature, pressure and the four interactive chemical species. Above 4hPa and below the tropopause, concentrations are relaxed towards climatology, with timescales of about 2 hours above and 3 days below.

The “true state of the atmosphere” and the initial conditions for the 128 members of the ensemble are taken from a separate, 129-year free simulation of the IGCM-FASTOC. The true state is chosen among the 129 years as the central-most 0000 UTC 1 January state vector in the global stratospheric RMS temperature error sense. The remaining 128 0000 UTC 1 January state vectors are taken as initial conditions for the 128 members. The choice of setting the ensemble size to 128 members will be discussed in Section 2.3.2. This approach of defining initial conditions from a climatological ensemble allows to start with dynamically-balanced initial conditions, as opposed to synthetic initial conditions produced by randomly perturbing a single model state, which requires some time to restore its balance. The other advantage is that the climatological ensemble nearly represents the full variability of the model, except for losses accountable to sampling errors, while synthetic ensembles lose part of their variability in the balance restoration. It thereby provides a reference of the model variability which can be compared to the assimilation product.

Our observation network was generated to mimic the Michelson Interferometer for Passive Atmospheric Sounding (MIPAS) retrievals on board the *Environmental Satellite* (ENVISAT; Raspollini et al., 2006; Cortesi et al., 2007). The justification lies in the relatively good stratospheric vertical resolution, and a good horizontal coverage. Limb-viewing products such as MIPAS offer good horizontal coverage with lower accuracy than solar-occultation products, like the Atmospheric Chemistry Experiment-Fourier Transform Spectrometer (ACE-FTS; Bernath et al., 2005), that have sparse coverage at the benefit of small observation errors.

MIPAS products achieve global coverage within 3 days. On a daily basis, they have 12.5° longitudinal spacing and 5° latitudinal (along track) spacing between adjacent scans. With a horizontal resolution of the model of about $5.6^\circ \times 5.6^\circ$, we can simply locate the observations on model grid points both in the latitude (every grid point) and the longitude (every 3 grid points) directions. Although the vertical range of MIPAS is 6 to 68 km altitude, we restrict the assimilation of observations to the stratospheric range between 12 and 38 km (i.e., between 175 and 4 hPa), in order to avoid the sponge layer and the areas not covered by the chemistry scheme. The vertical resolution of MIPAS is 3 km in the vertical, roughly equivalent to the IGCM-FASTOC vertical resolution in this range. This permits one to create observations from the “true state” by simply linearly interpolating variables to a set of “observed” (constant) log-pressure levels. This implies, as mentioned above, that the measurement operator \mathcal{H} is weakly non-linear: since the model is in vertical σ -coordinates, the interpolation depends on surface pressure P_s , which is a state variable.

The perturbed observations are generated from the “true” state with a Gaussian unbiased random noise with standard deviation of 2 K in temperature and 10% in ozone mixing ratio, consistently with instrument random error estimates and other MIPAS assimilation studies above 100 hPa (Baier et al., 2005; Wargan et al., 2005; Errera et al., 2008, and references therein). In the lower stratosphere below 100 hPa, although the ozone error increases beyond 10% in MIPAS, we keep this error constant to simplify the interpretation of the results with height. We also do not take instrumentation bias into account in order to keep the system simple. But note that bias-aware data assimilation is an active research field (e.g., Dee, 2005), which we chose not to approach in this study. As mentioned above, all daily MIPAS data are assumed to be observed at the analysis time in this study.

2.3.2 EnKF Parameters

The most important parameter is the size of the ensemble, the literature suggests that around 100 members is usually sufficient for atmospheric systems, *given proper localization in the error covariances* (Mitchell et al., 2002). We have thus set our ensemble size to $m = 2^7 = 128$, and provide an analysis of the sensitivity to localization parameters. Obviously, the larger m the better the analysis, but the computational cost of raising this parameter significantly further is very large.

Following Houtekamer and Mitchell (2001), we assimilate synthetic satellite profiles in batches with a maximum of p_{\max} observations, inscribed in horizontal circles of radius r_0 . When it is impossible to include p_{\max} observations in a single

circle, another one is introduced such that the closest possible observations between the two circles be at least two decorrelation lengths C_h away. This preserves sparseness in the forecast-error covariance matrix, [i.e., ensures that observations from one circle do not affect (or covary with) the other one(s)]. This effectively increases the rank of \mathbf{P}_e^f [see discussion by Oke et al. (2007)]. The choice of p_{\max} and r_0 does not seem to affect the analysis scores (Houtekamer and Mitchell, 2001), and is made solely to optimize the speed of calculation. Here, we impose the additional constraint that the horizontal observation density stays the same in local batches as in the global observing system. Namely, we impose a constant ratio of observations per area $p_{\max}(\pi r_0^2)^{-1}$. This should ensure that the number of circles is minimized in every batch. With an Earth surface area of $5 \times 10^8 \text{ km}^2$ and, in our case, a horizontally smooth MIPAS coverage that includes about 700 observations per level, the ratio is set to 4.4×10^{-6} observations km^{-2} . In the following experiments, we will be using a value $p_{\max} = 100$ observations, which makes $r_0 \approx 4800 \text{ km}$.

Localization is applied to $\mathbf{H}\mathbf{P}_e^f\mathbf{H}^T$ and $\mathbf{P}_e^f\mathbf{H}^T$ directly, since \mathbf{P}_e^f is not stored. This requires that the observation operator \mathcal{H} be linear. In our case, there is a non-linearity due to the effect of the surface pressure P_s on the location of sigma levels. However, test assimilation with a linearized operator \mathbf{H} did not display significant differences in the analyses, motivating our use of the non-linear operator. The localization function used in this study is the fifth-order piecewise rational function of Gaspari and Cohn (1999) [their Eq. (4.10)]. It is a correlation function (i.e., the product between this function and a covariance matrix retains

the positive semi-definiteness property of the latter) which resembles a Gaussian but goes exactly to zero at the decorrelation length parameter. We apply vertical and horizontal localization sequentially, therefore needing separate horizontal and vertical decorrelation lengths. Note that localization is applied equally to autocovariances and cross covariances (except for the special case of temperature-ozone cross covariances, as will be mentioned in the beginning of Section 2.5). Houtekamer et al. (2005) used the following values for horizontal and vertical decorrelation lengths, respectively, throughout the troposphere and stratosphere: $C_h = 2800$ km and $C_v = 2$ units of log-pressure. However, Houtekamer and Mitchell (2001) found that for 128 members, the optimal horizontal decorrelation length minimizing the error and spread in the analysis ensemble was approximately 6000 km. Furthermore, the study of Oke et al. (2007) showed, from the analysis of a simple model where balances are exactly known, that too short localization can result in model imbalance. This motivates some sensitivity study on localization parameters in order to ensure optimality of the assimilation.

No covariance inflation is applied in this study. However, a diagnostic covariance inflation is estimated for monitoring purposes. As will be shown in Section 2.4, the localization parameter provides a sufficient control on this diagnostic to justify the absence of covariance inflation.

2.3.3 Diagnostics

Assessment of our ensemble assimilation system is performed using the forecast/analysis root-mean-square error (RMSE) and ensemble spread (SPREAD), as

expressed in (Anderson, 2007a):

$$\text{RMSE} = \sqrt{\frac{1}{n} \sum_{i=1}^n [\langle x_i \rangle - x_i^t]^2} \quad (2.9)$$

$$\text{SPREAD} = \sqrt{\frac{1}{n(m-1)} \sum_{i=1}^n \sum_{j=1}^m [x_{i,j} - \langle x_i \rangle]^2} \quad (2.10)$$

The superscript t denotes the “true state”, $x_{i,j}$ is the element of the forecast/analysis vector \mathbf{x} with spatial coordinate i corresponding to member j and the overbar denotes the ensemble average. n is the state vector size and m the ensemble size.

These two diagnostics are applied to the total energy (TE) norm (Ehrendorfer and Errico, 1995), which has the advantage of incorporating 4 variables of the model state space, and is often used in context of error growth analysis:

$$\text{TE} = u'^2 + v'^2 + \frac{C_p}{T_{ref}} T'^2 + \frac{R_\alpha T_{ref}}{P_{ref}^2} P_s'^2 \quad (2.11)$$

The variables that are primed represent either the error with respect to the truth in the case of the RMSE calculation, or departures from the ensemble average in the case of the SPREAD. Finally, we take the TE norm as the square root of Eq. 2.11 to obtain a convenient variable in units of meters per second. The reference pressure and temperature are $P_{ref} = 1000$ hPa and $T_{ref} = 300$ K, respectively. $C_p = 1005.7$ J K⁻¹ kg⁻¹ is the specific heat at constant pressure and $R_\alpha = 287.04$ J K⁻¹ kg⁻¹ is the gas constant of dry air.

As argued by Sacher and Bartello (2009), the RMSE and SPREAD diagnostics express the “accuracy” and “reliability” of the EnKF, respectively. A satisfactory ensemble assimilation should provide the most accurate analysis,

closest to the true solution. It also needs to be reliable: the true state must be statistically indistinguishable from a randomly-selected member of the ensemble. For second-order moment statistics, the reliability can only be measured through the variability of the ensemble (i.e., the SPREAD). To achieve consistency between the SPREAD and RMSE, we need their ratio to be close to unity. A SPREAD smaller than the RMSE is prone to filter divergence, as discussed previously, while the opposite case is “safer” but yet shows that the EnKF underestimates the quality of the system, thereby giving too much weight to the observations.

It is also instructive to perform a direct diagnostic of the success of the system. Desroziers et al. (2005) derived the following equalities, provided that \mathbf{P}^f and \mathbf{R} are well specified:

$$\left\langle [\mathcal{H}(\mathbf{x}^a) - \mathcal{H}(\mathbf{x}^f)] [\mathbf{y} - \mathcal{H}(\mathbf{x}^f)]^T \right\rangle = \mathbf{H}\mathbf{P}^f\mathbf{H}^T \quad (2.12)$$

$$\left\langle [\mathbf{y} - \mathcal{H}(\mathbf{x}^a)] [\mathbf{y} - \mathcal{H}(\mathbf{x}^f)]^T \right\rangle = \mathbf{R} \quad (2.13)$$

These expressions are true for an infinite ensemble, and deviations from equality provide an assessment of the quality of the error covariance matrices specification, particularly in a OSSE where observation errors are set. This is similar to the covariance inflation and observation error estimation technique of Li et al. (2009). Consistently, we define the two quantities:

$$\alpha = \left(\frac{\text{Tr}\left\{\left\langle [\mathcal{H}(\mathbf{x}^a) - \mathcal{H}(\mathbf{x}^f)] [\mathbf{y} - \mathcal{H}(\mathbf{x}^f)]^T \right\rangle\right\}}{\text{Tr}\{\mathbf{H}\mathbf{P}_e^f\mathbf{H}^T\}} - 1 \right) \cdot 100\% \quad (2.14)$$

$$\beta = \left(\frac{\text{Tr}\left\{\left\langle [\mathbf{y} - \mathcal{H}(\mathbf{x}^a)] [\mathbf{y} - \mathcal{H}(\mathbf{x}^f)]^T \right\rangle\right\}}{\text{Tr}\{\tilde{\mathbf{R}}\}} - 1 \right) \cdot 100\% \quad (2.15)$$

If the total error variances are perfectly specified *for the given observing system*, then both quantities α and β are exactly equal to zero. These quantities are calculated in diagnostic mode to estimate how close the $\mathbf{HP}_e^f \mathbf{H}^T$ and $\tilde{\mathbf{R}}$ error covariance matrices are from perfection, or conversely their discrepancy with respect to $\mathbf{HP}^f \mathbf{H}^T$ and \mathbf{R} , a positive value of α or β implying under-inflation, a lack of variance in the sample error covariance matrices. It is worthwhile to note that this diagnostic is computed in the observation space and only includes the trace of the matrices. However it does not totally ignore the influence of correlations, since the analysis vector \mathbf{x}^a depends on them by construction.

2.4 Sensitivity Studies

In this section, the diagnostics described in Section 2.3 are applied to determine optimal parameters for vertical and horizontal localization, for both the temperature assimilation scenario and the ozone assimilation scenario. This sensitivity study is performed for a suite of selected values of horizontal and vertical localization parameters applied equally to all covariances (i.e., auto and cross covariances of all variables), and not only to the observed variable.

The sensitivity study is performed by looking, first, at sensitivity of the assimilation experiment to vertical and horizontal localization parameters separately, and, second, at the most optimal pair of vertical and horizontal localization parameters. For the temperature-assimilation experiments, results are discussed in detail hereafter, showing the temporal evolution of the diagnostics (Figs. 2–1 and 2–2). (To avoid redundancy, the discussion for the ozone assimilation sensitivity counterpart is made on the basis of temporal averages of diagnostics, as summarized in

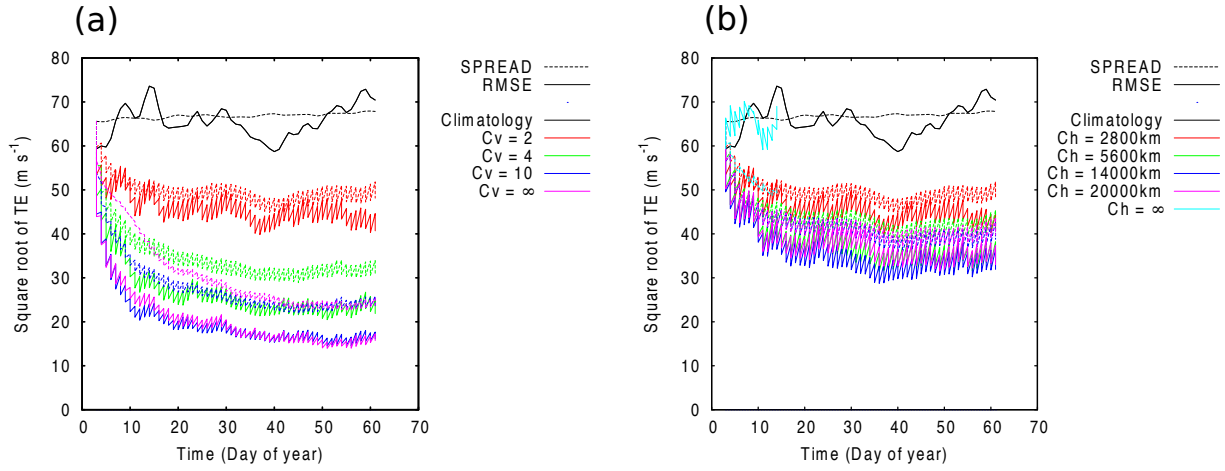


Figure 2–1: RMSE (solid lines) and SPREAD (dashed lines) of the square root of the TE norm (m s^{-1}) for the temperature assimilation scenarios with (a) fixed $C_h = 2800$ km and varying C_v and (b) fixed $C_v = 2$ and varying C_h .

Table 2–2.) For the separate horizontal and vertical sensitivity, reference values for both directions are the ones used in Houtekamer et al. (2005): $C_h = 2800$ km and $C_v = 2$ units of log-pressure.

2.4.1 Assimilation of Temperature

RMSE and SPREAD

Evolution of the RMSE and SPREAD in the square-root of the TE norm for the different temperature assimilation runs and for climatology, are displayed in Fig. 2–1. The climatological ensemble keeps a very steady SPREAD with time, while the RMSE wiggles around the SPREAD as time goes, illustrating the global non-linear nature of the system. By itself, the free-running climatological ensemble is rather inaccurate, as the error (RMSE) is very unsteady and often overshoots the general uncertainty (SPREAD) of the system. But we can also

see that since the true state is statistically undistinguishable from the ensemble members (being taken from the same climatological distribution), the values of RMSE and SPREAD remain consistent over time.

In Fig. 2-1a, the horizontal decorrelation length is set to $C_h = 2800$ km and assimilation cycles of 60 days were run with the following vertical decorrelation lengths: $C_v = 2$, $C_v = 4$, $C_v = 10$ or $C_v = \infty$ in log-pressure units (equivalent to $C_v = 14$ km, $C_v = 28$ km, $C_v = 70$ km and $C_v = \infty$, respectively), the last one being equivalent to not applying any vertical localization.

All data-assimilation runs improve the RMSE and SPREAD compared to climatology. More precisely, as the vertical localization length is increased, the SPREAD and RMSE are reduced to smaller values, the steadiness of the RMSE is increased but the ratio of SPREAD to RMSE increases. Note that it takes about 15 days for the EnKF to reach “steady state” in the SPREAD and RMSE. Hereafter, time averages will be shown from day 15 onwards.

Interestingly, the best constraints on the RMSE are obtained with $C_v = 10$ (blue curve) and $C_v = \infty$ (ie. no localization, pink curve), with both parameters yielding the same final values. However, the SPREAD in the localized ($C_v = 10$) case approaches the steady state faster. In the unlocalized ($C_v = \infty$) case, the usual sawteeth pattern of error growth/decay in the forecast/analysis SPREAD, which reflects a desired behavior, is replaced by a decay/decay cycle in the first 15 days of the cycle. The fact that the forecast does not allow errors to grow likely indicates important imbalances in the analysis as produced by non-zero remote covariances due to sampling errors. In contrast, in the localized case with $C_v = 10$,

remote covariances are damped and the forecast/analysis cycles show healthy growth/decay patterns.

In Fig. 2-1b, the vertical localization parameter is set to $C_v = 2$ and we run assimilation scenarios with $C_h = 2800$ km, $C_h = 5600$ km, $C_h = 14000$ km, $C_h = 20000$ km or $C_h = \infty$. The conclusions are different from the vertical localization cases. First of all, the reduction in RMSE when relaxing horizontal localization to larger length is weaker than what is achieved when relaxing vertical lengths. The lowest global time-averaged RMSE (with the 1σ uncertainty) obtained is 31.3 ± 1.4 m s⁻¹ in the $C_h = 14000$ km case, compared to 16.3 ± 1.4 m s⁻¹ in the $C_v = 10$ case of Fig. 2-1a. Also, there is a reduced accuracy when the localization length is too large (here $C_h > 14000$ km), as opposed to the vertical case. In terms of reliability though, the ratio of SPREAD to RMSE is closer to unity in the case with the longer decorrelation length $C_v = 20000$ km. The horizontally unlocalized ($C_h = \infty$) simulation, with the blue curve stopping at day 15 in Fig. 2-1b, is a clear case of filter divergence: it shows reasonable values of SPREAD but an RMSE close to climatology before the system explodes.

Inflation Diagnostics

The evolution of \mathbf{P}^f and \mathbf{R} discrepancy coefficients α and β (Eqs. 2.14 and 2.15) are shown in Fig. 2-2, with the same color scale and localization values as in Fig. 2-1. The α and β evolutions prove to be consistent with the square-root of the TE norm RMSE diagnostic. The cases with $[C_h, C_v] = [14\ 000\ \text{km}, 2]$ and $[2800\ \text{km}, 10]$, which minimized the time-averaged RMSE in both directions, also minimize the inflation diagnostics. The time-averaged values are $\alpha = 31 \pm 4$ % and

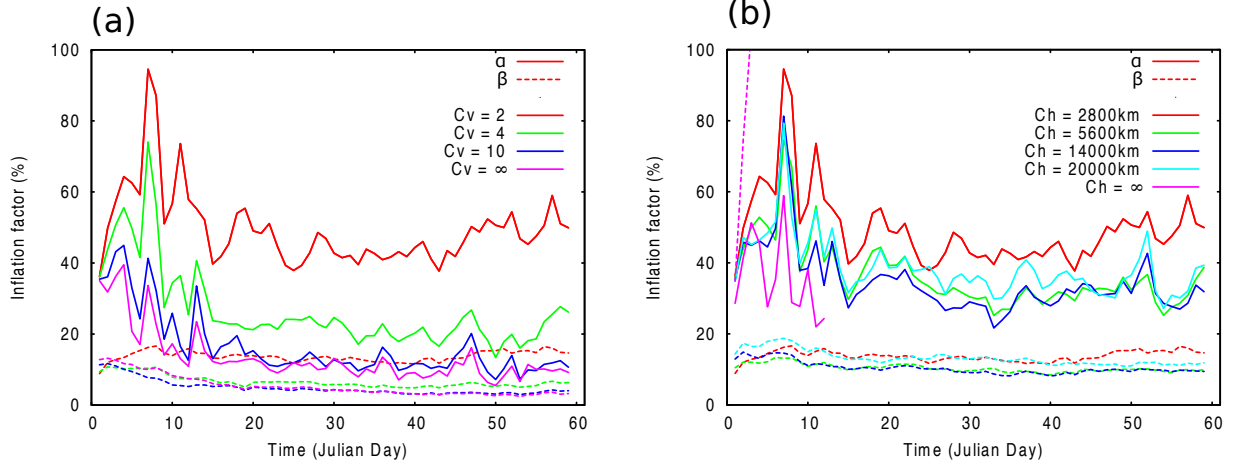


Figure 2–2: Evolution of the \mathbf{P}_e^f and $\tilde{\mathbf{R}}$ discrepancy coefficients α (solid line, in %) and β (dotted line, in %) for the temperature assimilation scenarios with (a) fixed $C_h = 2800$ km and varying C_v and (b) fixed $C_v = 2$ and varying C_h .

$\beta = 9.6 \pm 0.7$ % for the case [14 000 km, 2] and $\alpha = 12 \pm 3$ % and $\beta = 3.9 \pm 0.7$ % for the case [2800 km, 10]. In the case with [2800 km, 2], as in Houtekamer et al. (2005), the discrepancy in \mathbf{P}_e^f is as large as 46%, which may lead to eventual filter divergence.

Surprisingly, our case of filter divergence ($C_h = \infty$ and $C_v = 2$, pink curves in Fig. 2–2b) sees its β value exploding before α , and as early as the first assimilation cycle. However, Eq. 2.12 and 2.13 are only valid in the vicinity of correctly specified \mathbf{P}_e^f and $\tilde{\mathbf{R}}$ matrices, which makes the interpretation using α and β ambiguous. Note also that although our experiments are performed with a perfect model setup we do not achieve a perfectly specified $\tilde{\mathbf{R}}$ matrix, as shown in Fig. 2–2. This is due to two effects. First, although the intention is to specify $\tilde{\mathbf{R}}$ as uniform and diagonal, the ensemble of observations effectively has only m members, so that variances can be slightly misestimated and covariances between

Table 2–1: Results with assimilation of temperature: (top left) time-averaged α (in %), (bottom left) β (in %), (top right) SPREAD (in m s^{-1}) and (bottom right) RMSE (in m s^{-1}) diagnostics applied on TE, with corresponding 1σ uncertainty, for the various horizontal and vertical localization decorrelation lengths. Time averages and standard deviations are calculated over the last 45 days of assimilation. Minimum absolute values for the different diagnostics are highlighted in bold.

	$C_v = 2$		$C_v = 4$		$C_v = 10$	
$C_h = 2800$ km	45.8 ± 5.0	46.8 ± 0.9	21.4 ± 3.1	30.6 ± 1.3	12.4 ± 2.8	23.9 ± 1.7
	13.6 ± 1.3	42.6 ± 1.4	5.8 ± 0.6	22.7 ± 1.5	3.9 ± 0.7	16.3 ± 1.4
$C_h = 5600$ km	32.8 ± 4.5	40.1 ± 1.0	12.6 ± 2.2	22.1 ± 1.6	8.1 ± 1.8	16.8 ± 1.3
	9.9 ± 0.7	33.7 ± 1.6	3.0 ± 0.4	14.8 ± 1.3	1.8 ± 0.4	10.7 ± 1.2
$C_h = 14000$ km	31.1 ± 3.9	38.0 ± 1.4	8.9 ± 1.9	19.6 ± 1.6	5.9 ± 2.3	14.3 ± 1.1
	9.6 ± 0.7	31.3 ± 1.4	2.4 ± 0.5	12.2 ± 1.3	1.6 ± 0.5	9.2 ± 1.5
$C_h = 20000$ km	35.6 ± 4.2	38.6 ± 1.0	10.2 ± 0.3	20.4 ± 1.7	6.7 ± 0.3	14.2 ± 1.0
	12.3 ± 0.9	34.0 ± 1.6	3.0 ± 0.7	13.4 ± 1.6	2.0 ± 0.7	9.8 ± 1.5

observations may appear. Secondly, as Lupu et al. (2011) pointed out, the implicit dependance of β on \mathbf{P}^f through \mathbf{x}^a , can propagate a misspecification of \mathbf{P}_e^f in $\tilde{\mathbf{R}}$.

The fact that the β value varies with changing C_v and C_h values indicates that the second mechanism dominates.

Most Optimal Simulation

These results suggest that optimal horizontal and vertical temperature decorrelation lengths are located around $C_h = 14000$ km and $C_v = 10$ units of log-pressure when either C_h or C_v is held at our reference $[C_h, C_v] = [2800 \text{ km}, 2]$. Note that although these parameters minimized all diagnostic quantities studied, it should be kept in mind that they produce some inconsistency between the RMSE and SPREAD values. In order to verify that the combination of these two parameter values can be considered optimal, simulations with all the remaining pairs of parameters were performed. Time-averages and uncertainties of the diagnostics are tabulated in Table 2–1 with the optimal values highlighted in bold.

Table 2-2: Results with assimilation of ozone: (top left) time-averaged α (in %), (bottom left) β (in %), (top right) SPREAD (in m s^{-1}) and (bottom right) RMSE (in m s^{-1}) diagnostics applied on TE, with corresponding 1- σ uncertainty, for the various horizontal and vertical localization decorrelation lengths. Time averages and standard deviations are calculated over the last 45 days of assimilation. Minimum absolute values for the different diagnostics are highlighted in bold.

	$C_v = 2$		$C_v = 4$		$C_v = 10$	
$C_h = 2800$ km	10.6 ± 3.6	48.2 ± 0.9	-2.8 ± 3.7	26.6 ± 1.7	-5.3 ± 2.3	21.5 ± 2.3
	3.7 ± 0.5	41.6 ± 3.7	1.4 ± 0.4	18.2 ± 1.7	1.0 ± 0.4	14.1 ± 1.7
$C_h = 5600$ km	4.5 ± 3.0	39.6 ± 1.5	-2.1 ± 3.0	17.3 ± 2.3	-6.8 ± 2.0	13.8 ± 2.3
	2.4 ± 0.5	31.8 ± 2.5	0.5 ± 0.4	10.9 ± 1.8	0.5 ± 0.4	8.9 ± 1.9
$C_h = 14000$ km	5.7 ± 3.4	33.7 ± 1.7	-4.9 ± 4.7	13.3 ± 1.9	-23.5 ± 4.0	10.1 ± 1.7
	2.0 ± 0.4	28.8 ± 2.4	0.5 ± 0.4	9.5 ± 2.4	0.8 ± 0.6	8.6 ± 3.1
$C_h = 20000$ km	5.2 ± 3.0	33.7 ± 1.7	-69.6 ± 4.8	14.0 ± 2.3	-67.2 ± 1.5	12.0 ± 2.5
	2.7 ± 0.4	32.5 ± 2.3	7.0 ± 1.6	13.7 ± 3.5	2.0 ± 0.5	14.9 ± 4.9

For all RMSE, α and β diagnostics, the combination of optimal vertical parameter ($C_v = 10$) and optimal horizontal parameter ($C_h = 14000$ km) is also optimal as a pair, reaching values for the three diagnostics of 9.2 ± 1.5 m s^{-1} , $5.9 \pm 2.3\%$ and $1.6 \pm 0.5\%$, respectively, since none of these diagnostics take significantly lower values in any other combination. As for the SPREAD diagnostic, the smallest value of 14.2 m s^{-1} is actually witnessed for $[C_h, C_v] = [20000 \text{ km}, 10]$, but the extreme closeness to the $[14000 \text{ km}, 10]$ SPREAD value of 14.3 m s^{-1} , can not counter the choice of $[14000 \text{ km}, 10]$ as the most optimal pair of localization parameters for the temperature assimilation experiment.

2.4.2 Assimilation of Ozone

The fact that localization parameters are optimal for the assimilation of temperature does not guarantee that they are optimal for the assimilation of ozone. Time-averages of RMSE, SPREAD, α and β diagnostics for the similar

sensitivity study but with the assimilation of ozone are displayed in Table 2–2, with the minimum absolute values highlighted in bold. The choice is more ambiguous here than in the temperature assimilation study, since four pair of $[C_h, C_v]$ parameters obtain at least one minimum value of the time-averaged diagnostics. It is arguably the pair [5600 km, 4] which provides the most optimal diagnostics, since it has the best α and β values of -2.1% and 0.5%, respectively. We choose to give priority to the α and β diagnostics here because they are calculated in observation space and therefore represent only variables included in the observation vector (O_x concentration in this case). Conversely, the RMSE and SPREAD in the square-root of the TE norm are dynamical diagnostics and do not take into account chemical variables. Nevertheless, the RMSE and SPREAD are quite similar among the four simulations offering minimal values. Noteworthy though is the fact that the best ozone analysis produces the most inconsistent dynamical ensemble SPREAD versus RMSE values (17.3 m s⁻¹ versus 10.9 m s⁻¹).

The optimal values of localization lengths found here for temperature and ozone assimilations, $[C_h = 14000 \text{ km}, C_v = 10]$ and $[C_h = 5600 \text{ km}, C_v = 4]$ respectively, are used in the rest of the paper.

2.5 Multivariate Covariances

In this section, we assimilate either the temperature or the ozone observations and investigate its effect on the time-averaged analysis of temperature, zonal wind, ozone and specific humidity. The response will result from the interaction between (i) increments in the analysis where information is transferred from the observed variable to other variables by the cross covariance terms of the background-error

covariance matrix, and (ii) increments in the forecast step, where information from the observation as reflected in the analysis is transferred to other variables by model balancing. Note that the cross covariances can only represent a balance in a linearized form, whereas the model balancing includes non-linear components as well.

To separate the effects of these two channels of information transfer, a simple approach is to nullify selected covariances during the update phase. When assimilating temperature, nullifying temperature-chemistry covariances effectively keeps the chemistry unaffected by the analysis increments. Conversely, when assimilating ozone, nullifying ozone-dynamics covariances ensures that only the chemical part of the state vector is updated during the assimilation.

In order to investigate the transfer of information between temperature (and winds) and ozone, we consider the following two pairs of experiments:

- Temperature assimilation “Control” experiment: All variables are updated.
- Temperature assimilation “NoChem” experiment: Only the dynamical variables u , v , T and q as well as P_s are updated.
- Ozone assimilation “Control” experiment: All variables are updated.
- Ozone assimilation “NoDyn” experiment: Only the chemical variables O_x , NO_x , N_2O_5 and HNO_3 as well as P_s are updated.

Note that the surface pressure P_s is retained in both the “NoChem” and “No-Dyn” simulations so that both analyses can have some control on the height of the σ -levels. Note also that in the two temperature assimilation cases, the temperature-ozone cross covariances were localized based on the (short) ozone

optimal decorrelation lengths, because it produced better balance in the evolution of the ozone analyses (not shown).

2.5.1 Temperature Assimilation

Figure 2–3 displays the time-averaged global RMSE and SPREAD for the temperature (Fig. 2–3a), ozone (Fig. 2–3b), zonal wind speed (Fig. 2–3c) and specific humidity (Fig. 2–3d) analyses from the pair of temperature assimilation scenarios, with the climatology as reference. Note that results for the meridional wind are similar to those for zonal wind and are not shown. The ozone analysis is here normalized by the true value, in order to make analysis errors directly comparable to the observation’s relative error of 10% and remove vertical dependance of ozone mixing ratios. A minimum threshold was applied when normalizing by the truth to avoid division by zero, and we made sure that the number of points rejected never exceeded 5% on a given level. Note also that specific humidity is shown in a logarithmic scale.

The Control temperature assimilation cycle constrains the ensemble to a low RMSE and SPREAD inside the observation vertical range (horizontal dotted lines) for both wind and temperature, as compared to climatology. The accuracy of EnKF is therefore improved, but, consistently with the square-root of the TE norm diagnostics (Section 2.4), the SPREAD (dashed lines) is higher than the RMSE (solid lines). Outside the vertical range of observational data, the RMSE is reduced as well, but to a lesser extent, which is expected considering that the analysis relies only on correlations there, and that they expectedly decrease with vertical distance. As for the specific humidity analysis, the same

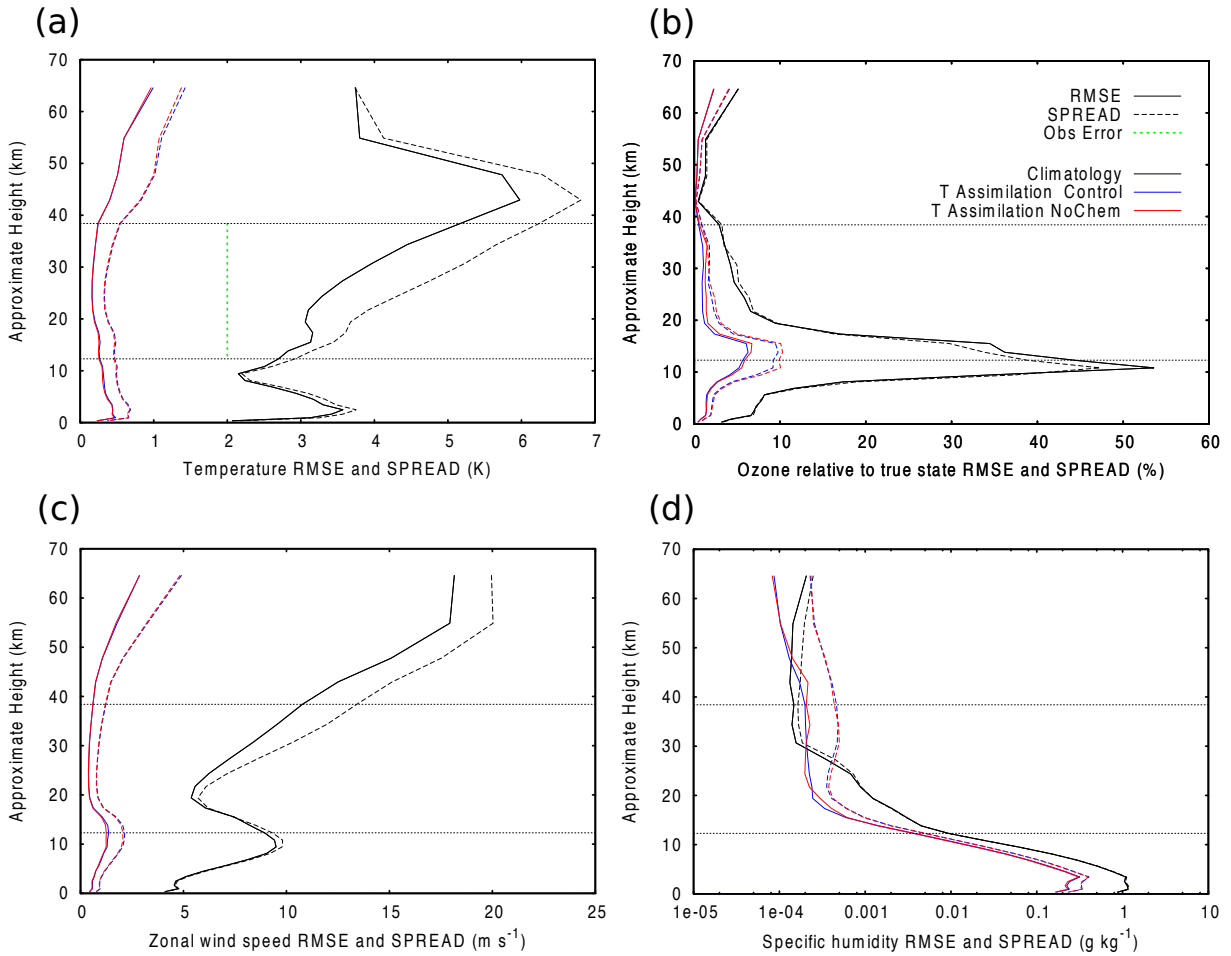


Figure 2-3: Results with assimilation of temperature: time-averaged RMSE (solid lines) and SPREAD (dashed lines) by σ levels, for (a) temperature (K), (b) ozone relative to true state (% of true value), (c) zonal wind speed (m s^{-1}), and (d) specific humidity (g kg^{-1}). Black curves represent climatology, blue curves the Control temperature assimilation and red curves the NoChem temperature assimilation (i.e., without dynamical-chemical covariances). For reference, the temperature observation error is shown in (a) as a green dotted line, and the vertical range of the observations by the thin horizontal dotted lines in (a)-(d). The vertical axis is the log-sigma approximate height (km). Time averages are performed over the last 45 days of assimilation.

conclusions can be drawn from the Control assimilation, but only in the lower stratosphere, below 25 km. In the upper stratosphere (30-50 km altitude), the Control assimilation does not provide a reduction in the analysis RMSE with respect to the climatology. This is likely due to the level of variability in specific humidity in this region, possibly lower than the noise introduced during the assimilation.

The NoChem assimilation results on temperature and winds is identical to the Control assimilation, showing that cross covariances are inactive in this case. This means that ozone chemistry analysis increments do not feedback significantly onto zonal wind or temperature. This tells us that the radiation, only pathways for ozone changes to affect temperature and change wind patterns, can not transfer efficiently to the thermodynamical state, over a 24-hour forecast period, any gain obtained in the ozone analysis. Radiation time scales are at least ten-fold longer than the forecast period in the stratosphere. In the case of ozone, the NoChem assimilation's RMSE is slightly larger than the Control assimilation's RMSE. Therefore, ozone corrections resulting from better dynamical initial conditions only can be further improved by including the temperature-ozone covariances. In the specific humidity case, including the chemical-dynamical covariances slightly improves the specific humidity analysis in the upper and lower stratosphere but not in the middle stratosphere (20-30 km). This suggests that cross covariances can slightly but not systematically improve tracers when temperature is assimilated. The ozone correction is mostly made by the model

during the forecast period, as a result of the correction of winds and temperature in the analysis.

2.5.2 Ozone Assimilation

Results are different in the case of ozone mixing ratio assimilation (Fig. 2–4). The Control experiment shows again good improvements with the EnKF, as compared to climatology. But now, the temperature and zonal wind analyses with the NoDyn assimilation show at most marginal improvements with respect to climatology. In other words, better ozone initial conditions do not help the model in adjusting the dynamics. This is consistent with the results of the temperature assimilation, which showed that the radiation is too slow to translate ozone increments into temperature. In this case, the capacity of dynamical-chemical covariances to help balance the dynamical variables through the analysis increments is striking: when including dynamical-chemical covariances in the assimilation (Control experiments, blue lines in Fig. 2–4) the temperature and zonal wind RMSE and SPREAD reduce to very small values across the entire atmospheric column. Moreover, the accuracy of temperature and wind analyses is similar to the temperature assimilation case.

The ozone analysis in the case of ozone assimilation shows an approximately equal improvement of its RMSE between the climatology and NoDyn as between the NoDyn and Control. Therefore, in the Control case, the thermodynamics is corrected by cross covariances during the assimilation step, which helps the model further adjust the ozone state during the forecast period. Note that this is the same effect as the one responsible to most of the ozone correction in the

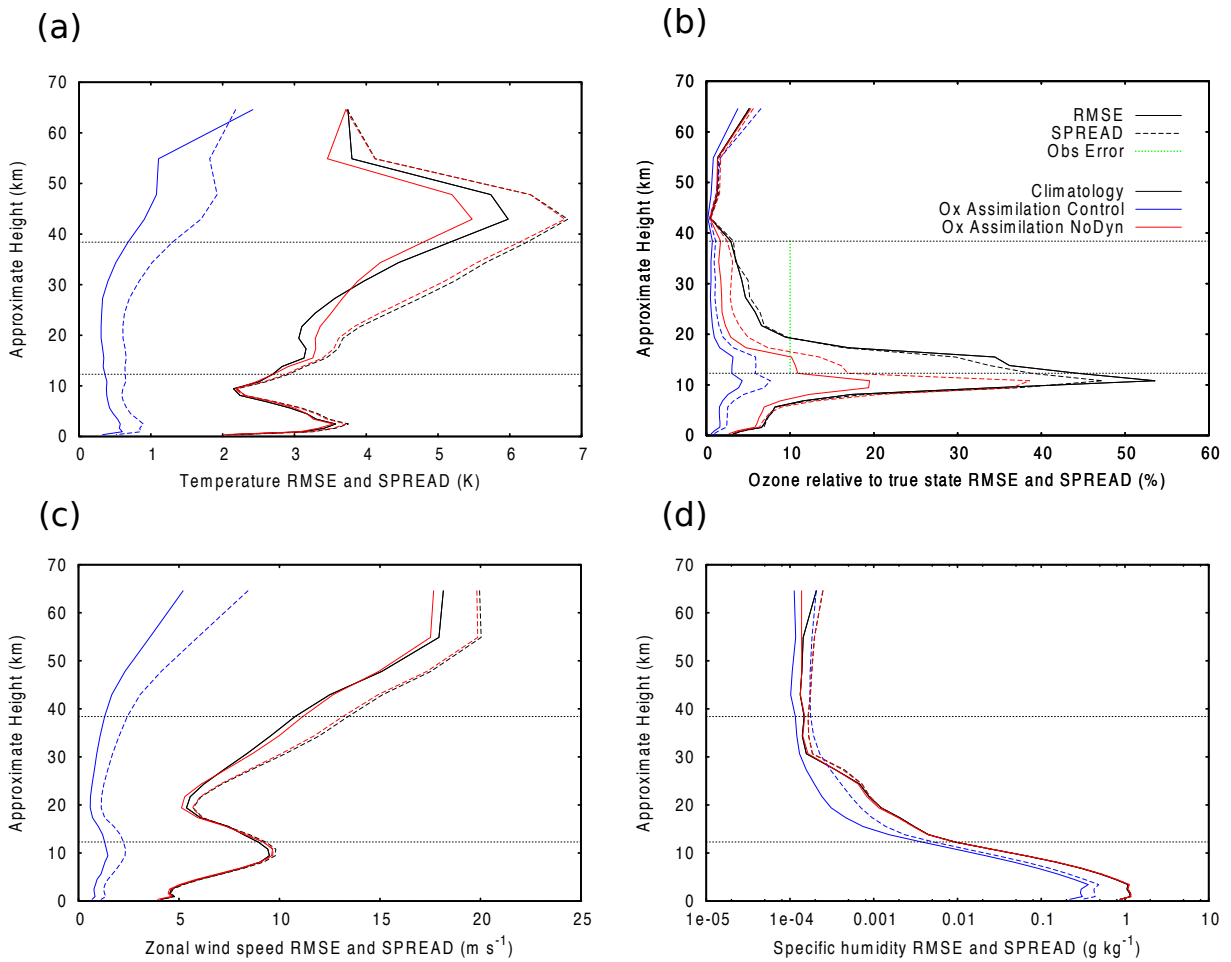


Figure 2-4: Same as Fig. 2-3 except that blue curves are results from the Control ozone assimilation and the red curves are for the NoDyn ozone assimilation (without chemical-dynamical covariances). (b) For reference, the ozone observation error is shown as a green dotted line.

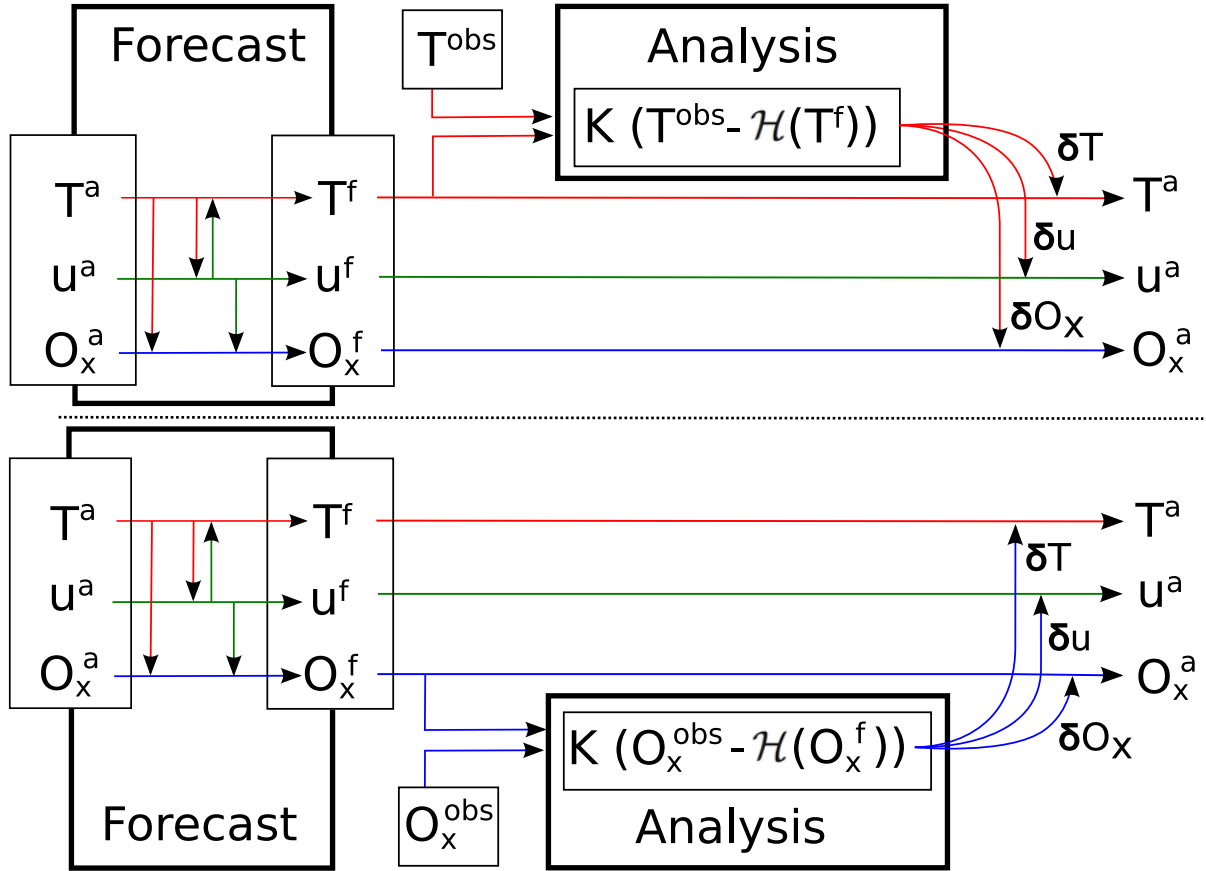


Figure 2–5: Schematic describing the information flow between variables during a data assimilation cycle, for our (top) temperature assimilation experiments and (bottom) ozone assimilation experiments. Curved arrows show the effect of cross covariances. Straight vertical arrows embedded in the “Forecast” box show the effect of model balancing. Note that ozone (O_x , blue arrows) can only affect the temperature (T , red arrows) and winds (u , green arrows) during the ozone assimilation, as observed in Section 2.5.

temperature assimilation case. Figure 2–5 summarizes schematically the flow of information during the assimilation cycle for both the temperature assimilation (top panel) and the ozone assimilation (bottom panel).

2.5.3 Ozone-Dynamical Covariances

Considering that most of the information from the ozone observations is transferred during the analysis phase through the ozone-dynamics covariances, it is interesting to determine which covariances in particular are responsible for the constrain of the dynamical variables. To investigate this, we ran two ozone-assimilation experiments:

- “NoTemp” ozone assimilation: All variables are updated except the temperature T .
- “NoWinds” ozone assimilation: All variables are updated except the zonal and meridional winds u and v .

Figure 2–6 shows the time-averaged analyses of zonal wind (Fig. 2–6a) and temperature (Fig. 2–6b) as a function of altitude. In the zonal wind analyses, the RMSE of the NoTemp assimilation is only about 1 m s^{-1} larger than the Control assimilation throughout the stratosphere, while the NoWinds RMSE is at least three times this difference. This implies that the ozone-winds covariances provide a stronger constraint on the zonal wind analysis than the ozone-temperature does. Figure 2–6b shows that this behavior is not symmetric. Indeed, ozone-temperature covariances have a weaker capacity to constrain the temperature analysis than do ozone-wind covariances (in conjunction with model balancing during the forecast period). In addition, the lack of ozone-wind covariances induces a very noisy

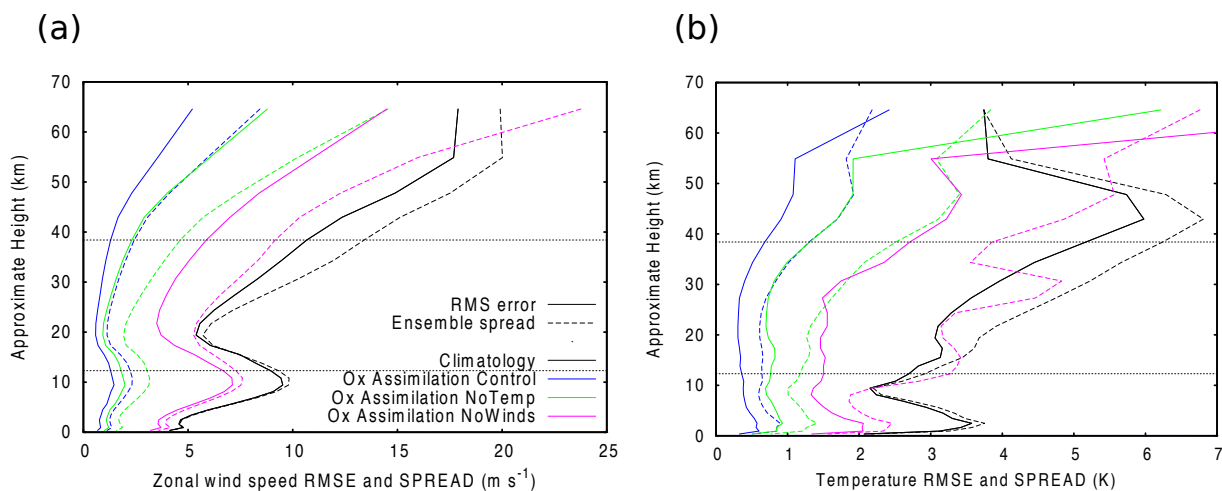


Figure 2-6: Time-averaged, σ -level-averaged RMSE (solid lines) and SPREAD (dashed lines) of (a) zonal wind speed (m s^{-1}) and (b) temperature (K) for various scenarios of ozone assimilation. Black curves represent the climatological ensemble, blue curves are the Control ozone assimilation experiment, pink curves and green curves are the NoWinds and NoTemp ozone assimilation experiments where ozone-winds or ozone-temperature covariances have been switched off, respectively. The vertical axis is the log-sigma approximate height (km). Time averages are performed over the last 45 days of assimilation.

vertical RMSE and SPREAD structure in the temperature analysis, pointing again towards a difficulty for ozone-temperature covariances to properly constrain the dynamical fields.

2.6 Conclusion

This study applies perfect-model OSSE hypotheses to a newly-developed EnKF on board a CCM, assimilating synthetic satellite retrievals of temperature and ozone mixing ratios, separately. We performed a sensitivity study on localization parameters, which showed, consistently with previous studies (Mitchell et al., 2002; Oke et al., 2007), that an appropriate choice of localization can prevent

filter divergence and that there exists an optimal value of prescribed decorrelation length which maximizes the reliability and the accuracy of the EnKF. These values appear to be, in the specific case of a January global stratospheric temperature assimilation, around 14 000 km and 10 units in log-pressure. Shorter horizontal and vertical localization values of $C_h = 5600$ km and $C_v = 4$ proved more optimal for ozone assimilation. Note however that these optimal values may vary according to season, and that splitting horizontal localization into longitudinal and latitudinal localizations might further improve as the natural anisotropy of the horizontal autocorrelation structures is better respected. These limitations may motivate a more adaptable method of localization, such as the Covariances Adaptively Localized with Ensemble CORrelations RAised to a Power (CALECO-RAP) proposed by Bishop and Hodyss (2007, 2009a,b) or the “hierarchical ensemble filter” of Anderson (2007b). However one should note that such adaptive methods of localization or the one used in this study, are still model-dependent and obtained optimal values must not be considered universal. In addition, the values proposed here have a significant uncertainty since, considering the computational expense associated with these sensitivity studies, only a few decorrelation lengths were tested.

Nevertheless, inflation diagnostics estimated for our most optimal localization parameters gave, in the temperature assimilation case, an inflation coefficient of 6% of the forecast-error covariance matrix and 1.6% for the observation-error covariance matrix. In the case of ozone assimilation, a deflation coefficient of 2.1% was estimated for \mathbf{P}_e^f and an inflation coefficient of 0.5% for $\tilde{\mathbf{R}}$. The low absolute

magnitude of these diagnosed coefficients ($< 10\%$) gives us some confidence in our choices of optimal localization parameters, and do not justify the application of artificial inflation. It is important to note that in all experiments the SPREAD was higher than the RMSE, meaning that the analysis ensemble has too much variability, but is well-centered near the true state. It is generally “safer” in ensemble prediction systems to overestimate the SPREAD, since the contrary would eventually result in filter divergence. However it also indicates that the analysis increments are noisy.

We also investigated the importance of cross covariances for temperature and ozone. Firstly, in the case of temperature assimilation, the EnKF converges towards an accurate solution in all analysis variables (except for specific humidity in the middle to upper stratosphere, where the variability in the climatology is very low anyway). The impact of including chemical-dynamical covariances in the EnKF is slightly felt in ozone but not in the temperature or the winds. Then, for the ozone assimilation case, similar accuracy is achieved for all analysis variables, but only in the presence of chemical-dynamical covariances in the EnKF. Without them, the dynamical analyses are hardly better than climatology. Improved ozone initial conditions for the forecasts do not help constraining the dynamics. The chemical-dynamical covariances appear to be well-enough specified to prevent filter divergence of the system. However, the systematic overestimation of the ensemble analysis spread might indicate that the covariances (auto- or cross covariances) contain noise, though not to the point of being detrimental to the system.

With regard to the stratospheric wind representation, the ozone-wind covariances produced from this Monte-Carlo ensemble technique produced significant improvement in the wind analysis when assimilating only ozone profiles. This is important as it shows that cross covariances can be very beneficial to the dynamics when assimilating ozone. Other experiments with 4D-Var in GCMs have shown improvements in wind analyses by assimilating ozone, not through explicit specification of background-error covariances, but implicitly through the tangent linear of the tracer transport model and its adjoint (Semane et al., 2009). The very different experimental setups makes it difficult to compare the quality of both techniques. However, our results suggest for the first time the potential of a well-specified background covariance matrix in constraining the unobserved wind field from ozone observations, in a CCM.

The results of this study are summarized in terms of information flow between variables in our EnKF in Fig. 2–5 for the temperature assimilation experiment (top panel) and the ozone assimilation experiment (bottom panel). Increments in the different variables during the analysis step are presented as the curved arrows and as vertical arrows for the forecast step. Of all the possible pathways, only the ozone radiative effect on temperature and winds in the model balancing was deemed negligible and thus omitted. The other pathways are effective in our EnKF system, though with various relative impact, as the ozone-wind covariances, for example, are much more effective than the ozone-temperature covariances.

This study is subject to a few limitations. Firstly, although our results seem quite robust, they come from single experiments and statistical significance is not

estimated. Secondly, this study is based on a perfect-model OSSE hypotheses. Although these hypotheses are justified in such a first study, it should be kept in mind that they may have some impact on the results presented here. Thirdly, all observations were assumed to be taken at the analysis time step. This reduces the problem to a three-dimensional one. Further investigations will address this issue of asynchronous observations, by extending the three-dimensional sequential EnKF to the time domain as well. This can include temporal interpolation to observations not at analysis time (Houtekamer et al., 2009), or even observations posterior to the analysis time window, within the Ensemble Kalman Smoother framework (EnKS, Evensen and van Leeuwen, 2000; Sakov et al., 2010).

Acknowledgment

We acknowledge fruitful discussions with and comments from Saroja Polavarapu, Jean de Grandpré, Simon Chabrilat, Richard Ménard, Peter Houtekamer, Herschel Mitchell and Ted Shepherd. Funding was provided by the Canadian Foundation for Climate and Atmospheric Sciences (CFCAS) and by the Canadian Chapter of the Stratospheric Processes And their Role in Climate (SPARC) initiative.

CHAPTER 3

Potential of an Ensemble Kalman Smoother for Stratospheric Chemical-Dynamical Data Assimilation

The previous chapter looked at the necessary (covariance localization) conditions for the Ensemble Kalman Filter analysis to better approximate the true model state. In addition, the constraint imposed by the assimilation of temperature or ozone observation on the other state variables was investigated. Two major simplifications were made in the assimilation system: the use of a perfect model observation system simulation experiment and the instantaneous nature of the observations. While the inclusion of model errors is beyond the scope of this thesis, the ability of ensemble assimilation to deal with observations spread over time is investigated here. An Ensemble Kalman Smoother formulation is used to extend the data assimilation system from a three-dimensional problem to a four-dimensional problem. The spatial impact of assimilating observations posterior to analysis time is investigated specifically for the analysis step and comparisons with the Ensemble Kalman Filter are provided.

The manuscript that constitutes this chapter has been submitted to Tellus A (ID #18541) in April 2012: Milewski, Thomas and Michel S. Bourqui, 2012: Potential of an Ensemble Kalman Smoother for stratospheric chemical-dynamical data assimilation.

Potential of an Ensemble Kalman Smoother for Stratospheric Chemical-Dynamical Data Assimilation

Thomas Milewski and Michel Bourqui

Department of Atmospheric and Oceanic Sciences, McGill University

Montréal, Qc, Canada

Abstract

A new stratospheric Ensemble Kalman Smoother (EnKS) system is introduced and the potential of assimilating posterior stratospheric observations to better constrain the whole model state at analysis time is investigated. A set of idealized perfect-model Observation System Simulation Experiments assimilating synthetic limb-sounding temperature or ozone retrievals are performed with a chemistry-climate model. The impact during the analysis step is characterized in terms of the root-mean-square error reduction between the forecast state and the analysis state. The performances of (i) an EnKS assimilating observations spread over 48 hours and (ii) an EnKF assimilating a denser network of observations are compared with a reference Ensemble Kalman Filter (EnKF). The ozone assimilation with EnKS shows a significant reduction of analysis error for dynamical variables in the upper-troposphere lower-stratosphere (UTLS) region when compared to the reference EnKF. This reduction has similar magnitude to the one achieved by the denser-network EnKF assimilation. The temperature assimilation with EnKS also significantly decreases the error in the UTLS for the ozone and wind variables

as much so as the denser-network EnKF assimilation. The temperature (ozone) assimilation with EnKS however significantly degrades the temperature (ozone) variable analyses through the time-lagged auto-covariances. The different analysis impacts from the assimilation of synchronous and asynchronous temperature observations indicate the capacity of time-lagged cross-variable background-error covariances to represent temporal interactions between variables during the ensemble data assimilation analysis step and the possibility to use posterior observations whenever additional current observations are unavailable.

3.1 Introduction

Over the past decade, there has been an increasing recognition that stratospheric dynamics influence tropospheric medium to long-range forecasts (Charlton et al., 2003; Gerber et al., 2012). Correspondingly, most operational centers have been raising the lid of their numerical weather prediction models. This extension of data assimilation to the stratosphere brings forth issues that are specific to the stratosphere, in particular model bias, dynamical-chemical nonlinearities and chemical or dynamical balances that require proper specification of background-error covariances.

The Ensemble Kalman Filter (EnKF; Evensen, 1994) is now established as a promising data assimilation approach for the initialization of operational weather forecasts (Whitaker et al., 2008; Szunyogh et al., 2008; Buehner et al., 2010b). Its relatively simple implementation and its reasonable performance even with non-Gaussian background states (Evensen, 2003) makes the EnKF an excellent candidate for constraining with observations the evolution of coupled nonlinear systems such as the stratosphere. It also provides an interesting framework for studying these complicated systems. An important nonlinearity issue in the stratosphere arises from the chemical-dynamical coupling. Chemical species are advected by the flow and ozone also feeds back on the radiation, hence contributing to determining the flow. Hence, to represent adequately the stratosphere, interactions between the dynamics and chemistry must be included in the modeling process, such as in chemistry-climate models (CCM; Eyring et al., 2006). The EnKF,

particularly the perturbed-observations type (Burgers et al., 1998), deals acceptably with a certain level of nonlinearity (Lawson and Hansen, 2004) despite being optimal for linear dynamics. It is thus likely to be appropriate for application to a CCM in order to perform chemical-dynamical data assimilation.

The EnKF uses a Monte-Carlo approach to estimate flow-dependent error covariances between variables from an ensemble of initially-perturbed forecasts. These (forecast-, prior- or background-) error covariances have two main purposes. First, they quantify uncertainties in the model forecasts and determine the weights applied to the model with respect to the observations. Second, they provide estimated correlations between variables of the model state for the propagation of the weighted information from the observed variable to the correlated variables, including in particular the unobserved ones. The error covariances are particularly important in the stratosphere considering the sparseness of observations, both spatiotemporally and in terms of the variables covered. As a consequence, the analysis significantly relies on the background-error covariances to “fill the gaps” appropriately and produce an accurate overall estimate of the model state.

Ensemble data assimilation may also be used to exploit temporal structures in observations for longer assimilation time windows, especially using observations posterior to the analysis time. This procedure is often referred to as the “Smoothing Problem” (see Cosme et al., 2011, for a complete overview of the different algorithms). The Smoothing Problem may offer an additional potential to improve the stratospheric analysis, for two main reasons. First, assimilation of observations posterior to analysis time allow the inclusion of additional data to constrain the

analysis. In a linear dynamics regime, the time lag between analysis and observations is irrelevant to the optimality of the analysis (as explained in Sakov et al., 2010) and therefore the assimilation of posterior (asynchronous) data has the same potential constraint on the analysis as the assimilation of current (synchronous) data. Of course, the stratospheric dynamics are forced by nonlinear phenomena such as momentum deposition from wave-breaking. It is therefore important to investigate the differential impact of assimilating asynchronous versus synchronous data. Second, assimilation of stratospheric chemical constituent observations spread over time may help retrieve the unobserved winds at analysis time. Indeed, temporal evolution of chemical constituents holds information on the winds as long as advection dominates over dissipation and chemistry within the assimilation time window and that the horizontal chemical tracer fields exhibit gradients parallel to the wind field (Daley, 1995; Riishøjgaard, 1996). This is likely to be the case in the lower stratosphere where ozone chemical timescales are long and where chaotic advection in the surf zone is dominant, outside the tropics. Furthermore, Milewski and Bourqui (2011, hereafter MB2011) have shown the ability of ensemble data assimilation of synchronous ozone data to constrain unobserved winds in an idealized setting through the background-error covariances.

In ensemble data assimilation applied to the Smoothing Problem, error covariances are calculated between analysis and observation times using ensemble statistics. This allows the background-error covariances to include temporal information. This temporal information might be better estimated than in four-dimensional variational assimilation (4D-Var) where the adjoint to the tangent

linear model is used to propagate posterior information backwards in time. Ensemble data assimilation smoothers use the full nonlinear model to estimate error covariances at various times, through which information from the posterior observations is transferred to the analysis. The smoothing problem in ensemble data assimilation was first approached with the Ensemble Smoother (ES; van Leeuwen and Evensen, 1996), similar to the AEnKF of Sakov et al. (2010), in which background-error covariances at all observation times within the assimilation window are obtained from the same ensemble of forecasts. It was later supplanted by the Ensemble Kalman Smoother (EnKS; Evensen and van Leeuwen, 2000), in which background-error covariances at a given observation time are calculated from an ensemble of forecasts initialized at the previous observation time.

The objective of this study is to explore the ensemble assimilation of posterior stratospheric data with a CCM with the goal of obtaining a better analysis at the beginning of the assimilation time window. This is relevant especially for improving reanalyses and medium to long-range forecasts, for which posterior observations are readily available for assimilation. This study follows that of MB2011 and uses similar modeling and data assimilation systems. In MB2011, ensemble data assimilation allowed a direct specification of flow-dependent multivariate background-error covariances, including chemical-dynamical covariances, which enabled the transfer of information from the observed variable to all state variables through repeated assimilation cycles. Here, we focus on the specific role of the analysis step and its ability to reduce forecast errors. These corrections obtained from the data assimilation are represented using the analysis minus forecast

(AmF) differences applied in calculating zonally-averaged root-mean-square errors (RMSE) for the variable of interest. This is first applied to an EnKF assimilations to provide an initial framework from which it will be easier to understand the added potential of the Smoother. Comparisons with an EnKF assimilating a denser network of observations (to assimilate the same total amount of observations as the EnKS) are also documented to estimate the viability of the Smoothing approach with a stratospheric CCM.

A description of the Ensemble Kalman Smoother is given in Section 3.2. The model, assimilation system and experiments are described in Section 3.3. The assimilation impact with the resulting error structures are shown in Section 3.4. Conclusions are drawn in Section 3.5.

3.2 The Ensemble Kalman Smoother

In this study, the Smoothing Problem is approached with the EnKS, as it yields better results than the ES in nonlinear contexts (Evensen and van Leeuwen, 2000), and for this experimental setup (not shown). The EnKS data assimilation technique solves an analysis equation very similar to that of the EnKF but with time-lags between analysis and innovations (observations minus forecast). It also uses forecasts initialized from a previous EnKF data assimilation experiment as background fields.

The expression for the matrix $\mathbf{X}_{\text{EnKS}}^a \in \mathbb{R}^{n \times m}$ holding the ensemble of m analysis states vectors $\mathbf{x}_{\text{EnKS}}^a$ of size n at analysis time t_k is:

$$\mathbf{X}_{\text{EnKS}}^{\text{a}}(t_k) = \mathbf{X}_{\text{EnKF}}^{\text{a}}(t_k) + \sum_{k'=k+1}^K \mathbf{P}(t_k, t_{k'}) \mathbf{H}_{k'}^{\text{T}} (\mathbf{H}_{k'} \mathbf{P}^{\text{f}}(t_{k'}) \mathbf{H}_{k'}^{\text{T}} + \mathbf{R}(t_{k'}))^{-1} \mathbf{D}_{k'} \quad (3.1)$$

with

$$\mathbf{D}_{k'} = \mathbf{Y}_{k'} - \mathbf{H}_{k'} \mathbf{X}_{\text{EnKF}}^{\text{f}}(t_{k'}) \quad (3.2)$$

$$\mathbf{P}(t_k, t_{k'}) \mathbf{H}_{k'}^{\text{T}} = \mathbf{X}_{\text{EnKF}}^{\text{a}}(t_k) \left(\mathbf{H}_{k'} \mathbf{X}_{\text{EnKF}}^{\text{f}}(t_{k'}) \right)^{\text{T}} \quad (3.3)$$

$$\mathbf{H}_{k'} \mathbf{P}^{\text{f}}(t_{k'}) \mathbf{H}_{k'}^{\text{T}} = (\mathbf{H}_{k'} \mathbf{X}_{\text{EnKF}}^{\text{f}}(t_{k'})) (\mathbf{H}_{k'} \mathbf{X}_{\text{EnKF}}^{\text{f}}(t_{k'}))^{\text{T}} \quad (3.4)$$

The EnKS analysis depends on the EnKF analysis $\mathbf{X}_{\text{EnKF}}^{\text{a}}$ at time t_k and the innovations \mathbf{D} at observation time $t_{k'}$ where $k' = k + 1, k + 2, \dots, K$. The innovations are the difference between the ensemble of observations \mathbf{Y} and the ensemble of forecasts from the EnKF data assimilation cycle $\mathbf{X}_{\text{EnKF}}^{\text{f}}$ mapped to observation space with the linear measurement operator \mathbf{H} . Here we use the unified notation of Ide et al. (1997), with extensions or changes to encompass the practical formulation of Evensen (2003). For example, here, the prime operator $(\cdot)'$ refers to the departure from ensemble average, and not to a linearization.

The initial EnKF analysis at time t_k is repeatedly corrected with observations at each posterior time $t_{k'}$ up to t_K , to eventually obtain the final EnKS analysis at time t_k . The innovations are weighted based on the model and observation uncertainties at observation time $t_{k'}$, given by their error covariance matrices $\mathbf{P}(t_k, t_{k'}) \mathbf{H}_{k'}^{\text{T}}$, $\mathbf{H}_{k'} \mathbf{P}^{\text{f}}(t_{k'}) \mathbf{H}_{k'}^{\text{T}}$ and $\mathbf{R}_{k'}$ (prescribed from knowledge on instrument

error). The background-error covariance matrix $\mathbf{P}(t_k, t_{k'})\mathbf{H}_{k'}^T$ also transfers the time-lagged innovation information from observation time $t_{k'}$ to analysis time t_k .

We introduce the notation $\text{EnKS}[\Delta t_1, \Delta t_2, \dots, \Delta t_K]$ to include the time-lag information $\Delta t_{k'-k} = t_{k'} - t_k$ (in hours) between observation time $t_{k'}$ and analysis time t_k , for better clarity when describing the different experiments in this study.

The sequential treatment of observations by batches (Houtekamer and Mitchell, 2001) used in MB2011 in the context of the EnKF could not be used in this study with the EnKS because of instabilities that arose from the sequential assimilation of batches. The RMSE and SPREAD (root-mean-square ensemble deviation about the ensemble mean as described in MB2011) of the ensemble dramatically increase in the assimilated variables after each batch in some localized spots in the North and South polar UTLS regions. The instabilities grow batch after batch and propagate to other variables and regions. Further investigation is needed to understand the causes of this instability. It however disappears when assimilating all observations of a given time at once using the compressed row storage technique (CRS, sometimes called ‘‘Compressed Sparse Row’’ CSR; Dongarra, 2000) to retain computational efficiency (details in Appendix C).

3.3 Experimental Setup

3.3.1 Assimilation Setup

This study, as in MB2011, is cast in a perfect-model Observation System Simulation Experiment context using a perturbed-observation Double-EnKF (Evensen, 1994; Burgers et al., 1998; Houtekamer and Mitchell, 2001) coupled with the chemistry-climate model IGCM-FASTOC (Taylor and Bourqui, 2005; Bourqui

et al., 2005) run at T21 resolution with 26 vertical sigma levels. A realization of the IGCM-FASTOC serves as the true state of the atmosphere (also referred to as “nature run” hereafter). Observations are synthesized from the nature run by trimming the state vector to the appropriate observation vector using the measurement operator \mathbf{H} . The observation vector is normally-randomized with a standard deviation equal to 10% for ozone and 2 K for temperature. The ensemble of observations generated are then assimilated to the ensemble of forecasts to obtain the ensemble of analyses. In this study, the ensemble of forecasts are taken from the CONTROL MIPAS experiments of MB2011 (hereafter CONTROL MIPAS O_x and CONTROL MIPAS T).

The assimilation setup retains the basic properties of the CONTROL Double-EnKF assimilation every 24 hours of MIPAS-like profile retrievals from MB2011 except for EnKS assimilations. For EnKS, observations are not assimilated in batches of up to a 100 observations anymore but all at once. Each profile has data on 11 levels, ranging from 180 to 4hPa (roughly 12 to 38 km altitudes) and the variables assimilated are either temperature (T) or odd oxygen mixing ratio (O_x). Note that O_x and O₃ (ozone) will be used interchangeably in the following, as usual in the stratosphere (Dessler, 2000). Note also that, for temperature assimilation, localization length parameters for all temperature-chemical tracer error covariances have been reduced to $[C_h, C_v] = [5600 \text{ km}, 4 \Delta \ln(P)]$. In MB2011, only the T-O_x error covariances were localized with this set of shorter-length parameters whereas temperature error covariances with other chemical tracers (NO_x, N₂O₅ and HNO₃) were treated with the longer-length parameters

[14000 km, 10 $\Delta\ln(P)$]. This allows to slightly improve results on the odd-nitrogen family $\text{NO}_y = \text{NO}_x + \text{HNO}_3 + 2 \times \text{N}_2\text{O}_5$ (not shown).

3.3.2 Experiments

A first set of experiments is designed to determine the accuracy of the analyses obtained when observations posterior to the analysis time are (asynchronously) assimilated as compared to when observations are synchronously assimilated.

Three 30-day ozone (or temperature) data assimilation experiments are initialized from the CONTROL MIPAS Ox (or CONTROL MIPAS T) analyses at day 30 and therefore cover the month of February. The three ozone (or temperature) data assimilation cycles follow the EnKS analysis (Equation 3.1 of Section 3.2) with a single observation time ($K = 1$) but different time lags of $\Delta t_1 = 0$ hour, $\Delta t_1 = 24$ hours and $\Delta t_1 = 48$ hours between observation and analysis, respectively. These experiments are denoted EnKF, EnKS[24] and EnKS[48] hereafter, based on the notation introduced in Section 3.2.

A second set of experiments is designed to study the potential additive impact of using observations at several times, this for both temperature and ozone assimilation. Individual data assimilation cycles are using, as background states, different daily ensembles of forecasts taken from the CONTROL MIPAS Ox and CONTROL MIPAS T assimilation experiments. The corresponding experiments are described below.

“EnKF MIPAS”: Reference experiment with synchronous assimilation of MIPAS temperature or ozone observations. Note that this is equivalent to doing a EnKS[0] update.

“**EnKS MIPAS**”: MIPAS temperature or ozone observations are asynchronously assimilated for two posterior days, in addition to the synchronous assimilation at time of analysis. The update procedure for the EnKS MIPAS is an EnKS[0,24,48].

Note that the EnKS MIPAS experiment assimilates three times more observations than the EnKF MIPAS experiment. The difference in the volume of data assimilated may lead to analysis improvements due to larger amounts of data assimilated, making ambiguous the benefits from the asynchronous aspect of the assimilation. The following experiment is designed to partially alleviate this ambiguity.

“**EnKF 3×MIPAS**”: Synchronous assimilation of observations corresponding to a three times denser MIPAS network. The EnKF 3×MIPAS is performed by repeating the EnKF (or EnKS[0]) analysis step three times, with horizontally-offset MIPAS observations each time. In the end, observations are filling the entire horizontal grid for the 11 stratospheric levels of the IGCM-FASTOC.

3.3.3 Initial Conditions

In the second set of experiments described above, assimilations are initialized from different CONTROL MIPAS T and Ox ensembles of forecasts and an individual single assimilation cycle is performed for each. In order to justify this choice, Figure 3–1 shows the RMSE and SPREAD for the CONTROL MIPAS Ox and T experiments (red and blue lines) and for the climatological ensemble (black lines). Initial conditions are taken from forecasts of day 31 onward, as both simulations present a stationary evolution with the desired saw-teeth pattern of

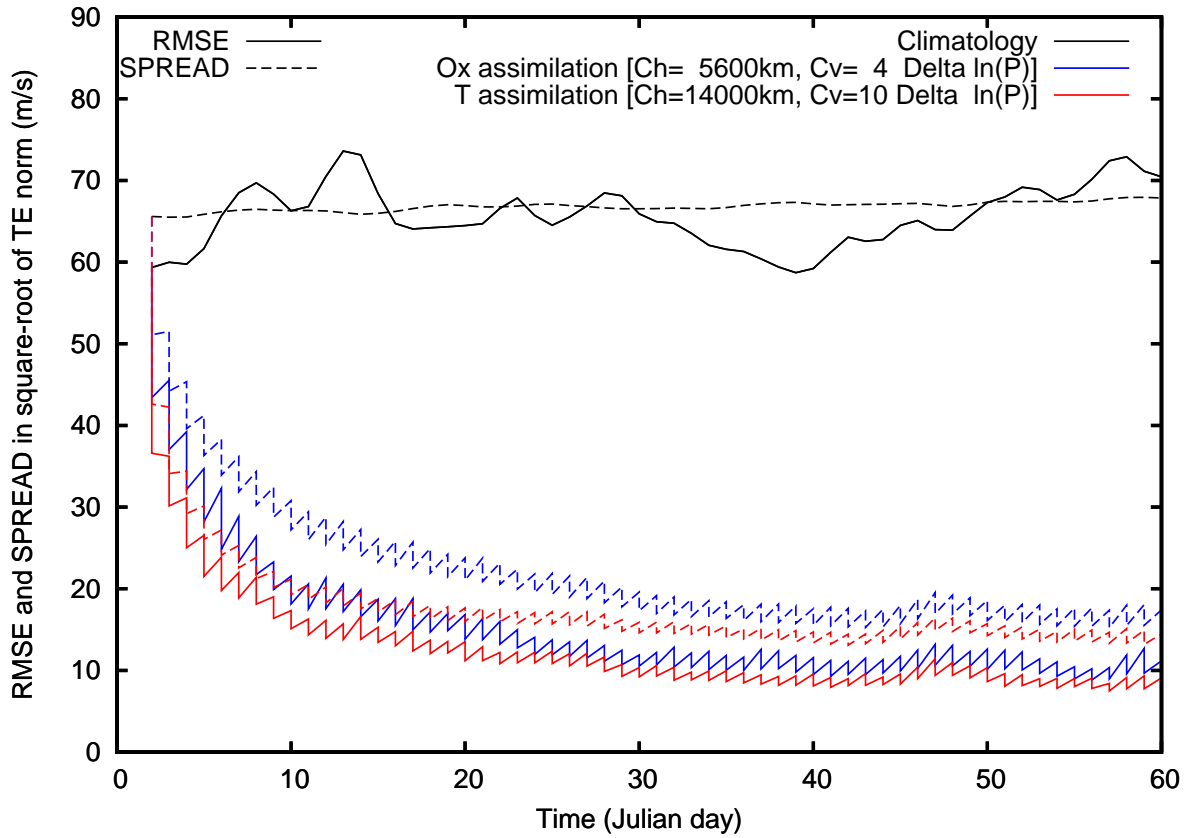


Figure 3–1: Time evolution of the root-mean-square error (RMSE, solid line) and ensemble spread (SPREAD, dashed line) of the square root of the total energy norm ($\text{m}\cdot\text{s}^{-1}$). Black lines: climatological ensemble; blue lines: ozone assimilation cycle; red lines: temperature assimilation cycle. Horizontal and vertical localization length parameters (C_h and C_v) are given in the legend.

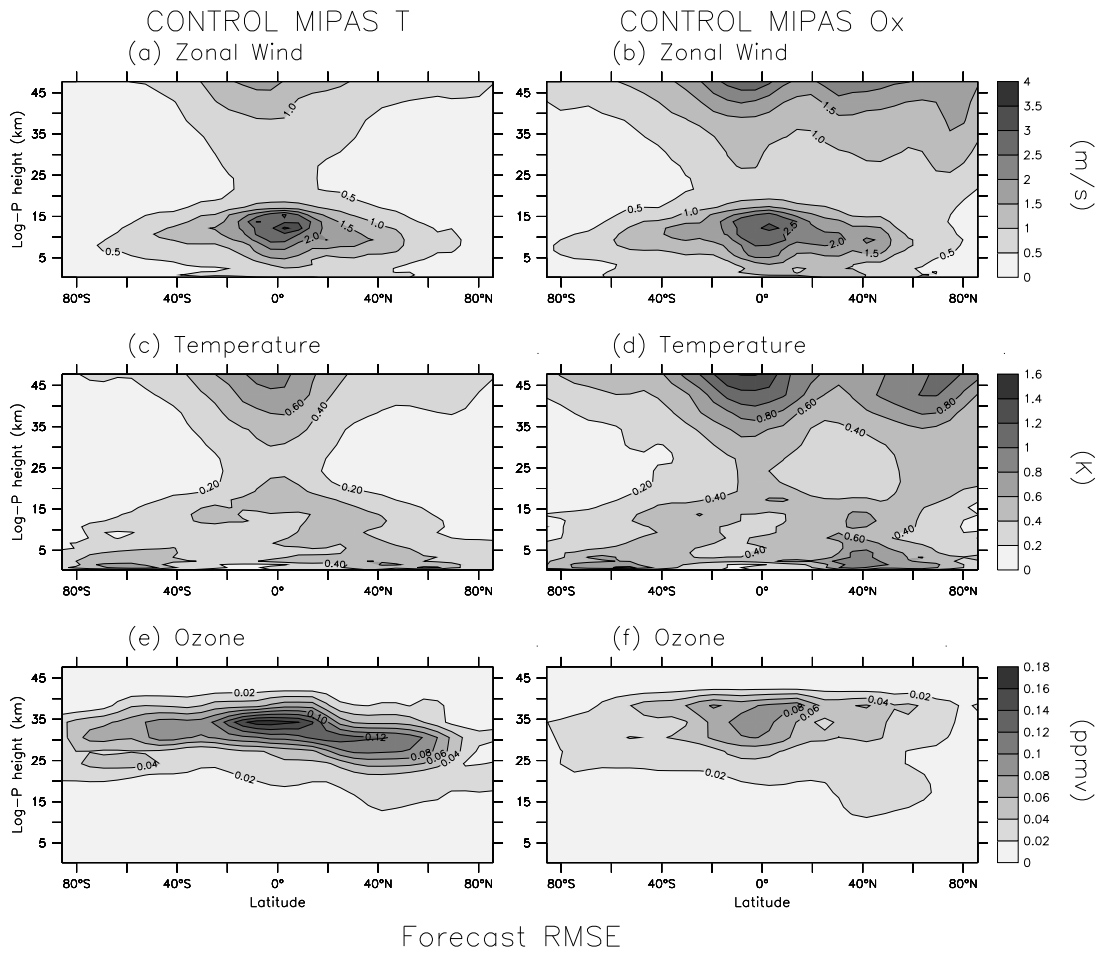


Figure 3-2: 10-day time-averaged zonal-mean forecast root-mean-square error (RMSE) for (top row) zonal wind ($\text{m}\cdot\text{s}^{-1}$), (middle row) temperature (K) and (bottom row) ozone (ppmv). Left and right columns show forecast RMSE from the CONTROL MIPAS temperature and ozone assimilation experiments, respectively.

forecast-error growth and analysis-error decay. Since experiments in this study assimilate observations two days posterior to the analysis time, in order to avoid any redundancy in the data assimilated, the forecast initial conditions are taken every three days in each experiment (i.e., CONTROL MIPAS T and CONTROL MIPAS Ox forecasts are sub-sampled at days 31, 34, 37, ..., 59), for a total of 20 different initial conditions for the month of February. Note that the SPREAD (dashed lines) is higher than the RMSE (solid lines) in both experiments without the use of any artificial covariance inflation. This is likely due to the limited amount of observations assimilated, as reported by Gottwald et al. (2011) and witnessed in Whitaker et al. (2009). There is a slight difference in magnitude between both experiments in the RMSE (solid lines) and SPREAD (dashed lines) quantities, with the CONTROL MIPAS T displaying the lowest values.

The spatial distribution of the time-averaged zonal-mean zonal wind, temperature and ozone forecast RMSE fields are showed in Figure 3–2 for the CONTROL MIPAS T and CONTROL MIPAS Ox forecasts. For each of the two experiments (left and right columns of Fig. 3–2), the RMSE fields are averaged over the 10 days of February taken as initial conditions. The forecast RMSE structures are quite similar in both experiments, except for the notable dynamical (temperature and zonal wind) errors in the Northern Hemisphere extratropical upper stratosphere only present in the CONTROL MIPAS Ox experiment. The differences are otherwise only in the magnitudes of the forecast RMSE. Smaller errors are witnessed in the ozone maximum for the CONTROL MIPAS Ox experiment and in the tropical upper stratosphere temperatures for the CONTROL MIPAS T

experiment. Overall, the differences in the forecast RMSE from both experiments are generally small. This allows the combination of different CONTROL MIPAS Ox and T daily ensembles of forecasts to form consistent initial conditions with a slightly wider variability. This consistency allows to compare the impact of the temperature and ozone assimilations on the same basis, with similar initial forecast conditions composed equally of temperature and ozone assimilation products.

3.4 Assimilation Impact on Analyses

In this section, the impact on the analysis of assimilating either temperature or ozone, synchronously or asynchronously, is investigated. The impact is quantified in terms of time-averaged zonal-mean RMSE change between the analysis and the forecast (hereafter, Δ RMSE, expressed in percentage relative to the forecast RMSE) for the variable of interest. This diagnostic was chosen because it isolates to some degree the effect of the analysis step from the subsequent balancing by the model forecasting step. It therefore allows to estimate typical error corrections accomplished by the EnKF or EnKS assimilation alone.

3.4.1 Synchronous Assimilation Impact

Before focusing on the assimilation impact of asynchronous observations, it is instructive to view which regions are affected in a typical synchronous EnKF assimilation of temperature or ozone observations. The error correction structures from the EnKF MIPAS are shown in Figure 3–3 for the zonal wind (top row), temperature (middle row) and ozone (bottom row) variables.

The EnKF MIPAS assimilation of temperature (left column) and ozone (right column) observations yields Δ RMSE values that are globally negative (blue to

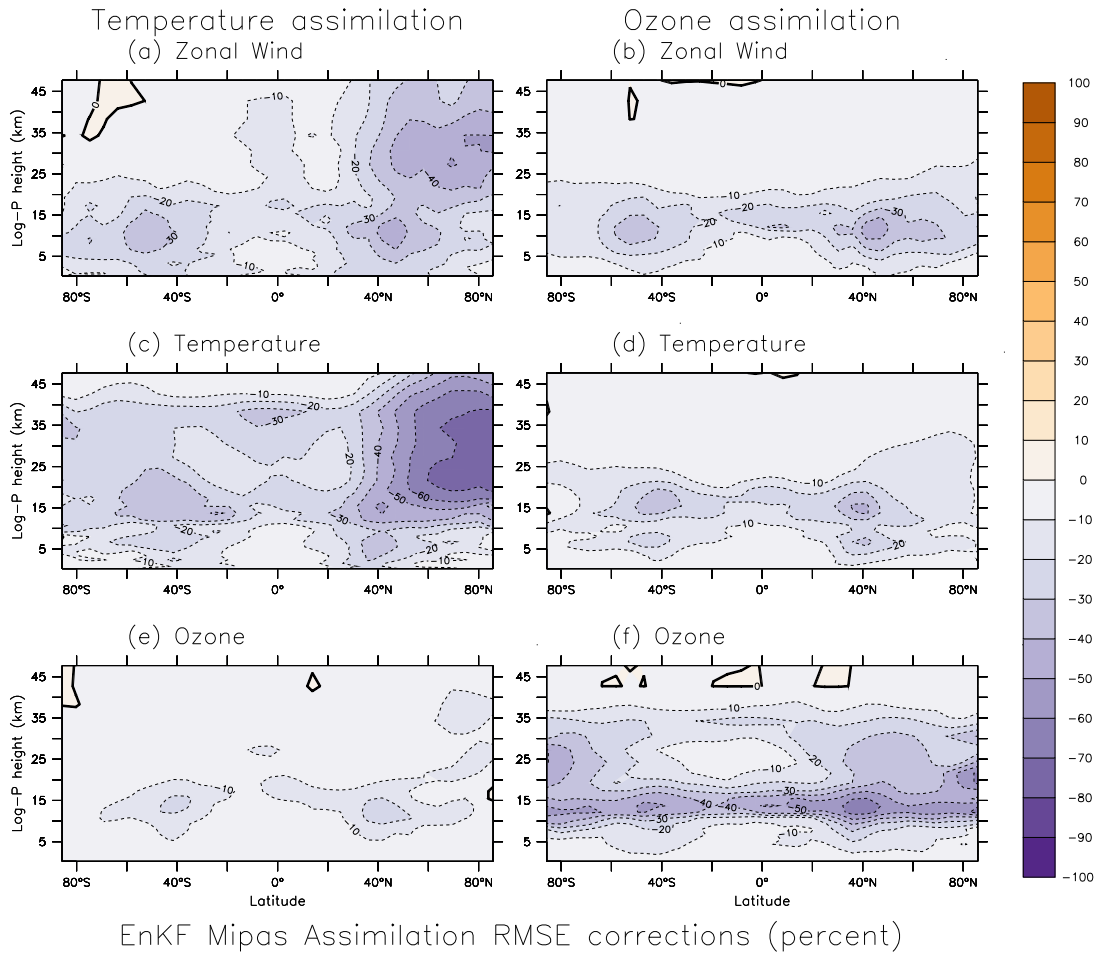


Figure 3–3: 20-day-average analysis-minus-forecast RMSE changes (in %) for (left column) EnKF MIPAS temperature assimilation and (right column) EnKF MIPAS ozone assimilation. Top row: zonal-mean zonal wind; middle row: zonal-mean temperature; bottom row: zonal-mean ozone. Zero-line of RMSE changes contoured with solid black line.

purple colors) implying beneficial assimilation impacts everywhere, except for a few small regions in the upper stratosphere with neutral or slightly detrimental assimilation impact (pink color). The EnKF MIPAS assimilation produces very different dynamical Δ RMSE with assimilation of temperature (left column) than with assimilation of ozone (right column). Temperature assimilation beneficially impacts the polar vortex winds and temperatures (Figs. 3–3a and 3–3c) while ozone assimilation achieves only limited improvements there (Figs. 3–3b and 3–3d). Note that this explains in part the larger forecast dynamical errors in the Northern Hemisphere in the CONTROL MIPAS Ox experiment (see Fig. 3–2). The most important Δ RMSE achieved with EnKF MIPAS temperature assimilation are in the polar vortex, with 70% error decrease per assimilation step for temperature and 50% error decrease for zonal wind. Strongest error corrections for ozone assimilation occur in the upper-troposphere lower-stratosphere (UTLS) region, with maximal RMSE reductions of up to 40% per analysis step in the tropospheric jets (Fig. 3–3b). The Δ RMSE are also different in the equatorial region where assimilation of temperature observations can better constrain the mid-stratosphere thermal and dynamical fields. In the UTLS, assimilation of ozone and temperature observations constrain the winds and temperature (Figs. 3–3 a-d) quite similarly. The improvements in the equatorial UTLS winds are an important achievement, considering the difficulties for models to correctly represent the dynamics in this region (Pawson et al., 2000; Eyring et al., 2006). The EnKF statistically captures some aspects of equatorial dynamical balances in its error covariances which might be otherwise difficult to prescribe (Zagar et al., 2004).

For each of temperature and ozone assimilation (left and right columns of Fig. 3–3, respectively), there is a strong similarity in the temperature and zonal wind Δ RMSE (Fig. 3–3a versus Fig. 3–3c and Fig 3–3b versus Fig 3–3d), but the impact on the ozone field is different. In fact, temperature assimilation corrects the global ozone errors only slightly. The only distinct signal is seen near the tropospheric jets. The ability of temperature assimilation to correct errors in the mid-to-upper stratosphere, as for the dynamical variables, is not witnessed in the ozone variable. Conversely, the ozone assimilation can only reduce the dynamical variable errors in the UTLS region. Its impact on the ozone state is not only strong near the tropopause but in the mid-stratosphere as well, particularly in both polar regions.

Apart from the UTLS and tropospheric jets that are well constrained in all variables by chemical and dynamical observations, there is a general complementary impact from assimilation of temperature and ozone in the mid-stratosphere. Temperature assimilation can constrain dynamical variables in that region, something that ozone assimilation can not achieve. In turn, ozone assimilation can constrain ozone, this being something that temperature assimilation can not achieve.

3.4.2 Time-lagged Assimilation Impact

Observations are rarely exactly measured at the time of analysis. In fact, “asynoptic” observations like satellite or radar data are spread over time. A purely sequential assimilation of such data, where a new assimilation cycle is started every time observations are available, would be extremely impractical.

Zonal wind RMSE correction (in percent)

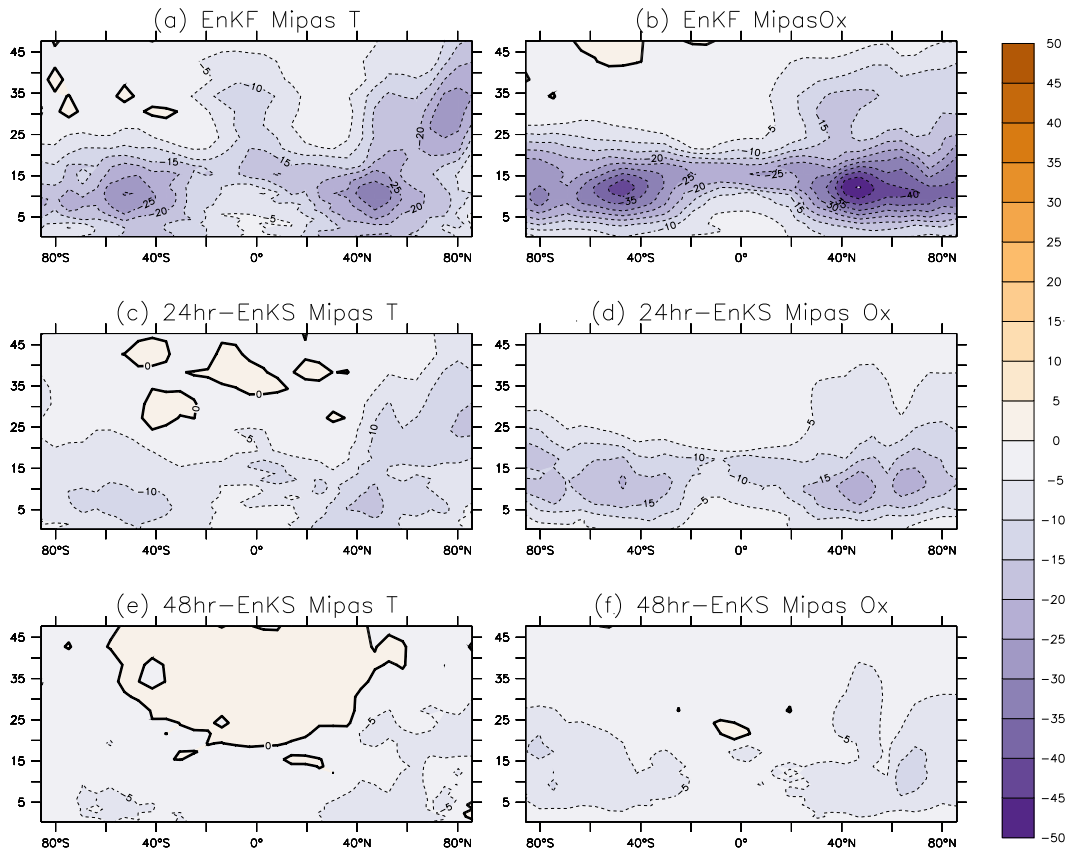


Figure 3–4: 30-day average of zonal-mean zonal wind analysis-minus-forecast RMSE changes (in %) for MIPAS ozone assimilation with (top row) an EnKF (middle row) an EnKS with 24-hour lag between observation and analysis time and (bottom row) an EnKS with 48-hour lag. Left and right columns show forecast RMSE from the CONTROL MIPAS temperature and ozone assimilation experiments, respectively.

In the case of linear dynamics, assimilating observations posterior to analysis time does not affect the filter solution (Sakov et al., 2010). But in realistic atmospheric simulations, such time-lags reduce the data assimilation performance. The assimilation impact as a function of time-lag is examined here.

The different assimilation impacts of the synchronous EnKF and the two asynchronous EnKS[24] and EnKS[48] experiments are investigated in terms of ΔRMSE , averaged here over the 30 daily analysis steps performed during a typical month of February. The time-averaged zonal-mean zonal wind ΔRMSE is presented in Figure 3–4 for the temperature assimilation (left column) and ozone assimilation (right column) experiments. Note the similarity of the zonal-mean zonal wind ΔRMSE for the EnKF MIPAS temperature and ozone assimilation experiments in Figures 3–3a and 3–3b with Figures 3–4a and 3–4b despite the different experimental setup (20 daily cycles initiated from CONTROL MIPAS Ox and CONTROL MIPAS T versus 30 daily cycles initiated from CONTROL MIPAS T or CONTROL MIPAS Ox; beware of the scale difference between figures). The relatively small differences obtained from both sampling strategies validate our choice of using both the CONTROL MIPAS Ox and CONTROL MIPAS T forecasts as backgrounds for the assimilation experiments.

The middle and bottom rows of Figure 3–4 display the assimilation impact from the EnKS[24] and EnKS[48], respectively. For a 24-hour time-lag between analysis and observations (Figures 3–4c and 3–4d), the temperature and ozone assimilation ΔRMSE structures remain relatively similar to the ones seen in the EnKF but the magnitude of the correction are globally reduced by a factor

of about 2. As the time-lag is increased to 48 hours (Figures 3–4e and 3–4f), assimilation corrections are further reduced to improvements lower than 10% per analysis step. The assimilation impact remains globally beneficial in the ozone assimilation experiment for a two-day time-lag, but becomes increasingly deleterious for the temperature assimilation case in the subtropical and tropical upper stratosphere. This decrease in ΔRMSE with time-lag is also witnessed for the other state variables O_x and T (not shown).

The background-error covariances are therefore able to convey information backward in time, but with a loss in signal with increasing time-lag. The overall decrease in magnitude of error corrections with time-lag does not allow an arbitrary choice of analysis time with respect to observations as expected for a linear model, this following Sakov et al. (2010). In our nonlinear context, the assimilation of synchronous observations has a better impact on the analysis than the assimilation of asynchronous (posterior) observations. Yet, the presence of a beneficial correction on the analysis based upon posterior observations suggests that assimilating posterior observations in addition to current ones has the potential of further improving the analysis.

3.4.3 Ensemble Kalman Smoother Assimilation Impact

The EnKF MIPAS assimilation experiment provides a reference to determine the relative impact of assimilating additional temporal data with the EnKS MIPAS or spatial data with the EnKF 3×MIPAS. These impacts are calculated by taking the difference between the EnKS MIPAS analysis RMSE and the EnKF MIPAS analysis RMSE, and the difference between the EnKF 3×MIPAS analysis RMSE

and the EnKF MIPAS analysis RMSE, respectively. These Δ RMSE values are also expressed in percentage relative to the EnKF MIPAS forecast RMSE, so that they can be compared to the Δ RMSE values of the synchronous EnKF assimilation case of Section 3.4.1.

The difference in zonal-mean zonal wind Δ RMSE between the EnKS MIPAS and the reference EnKF MIPAS is shown in the top row of Figure 3–5. Black lines enclose regions where differences are significant at the 95% confidence level, as determined from a bilateral Student’s *t* test. The only statistically significant differences are witnessed in the extratropical troposphere and UTLS regions, as well as near the tropical cold-point tropopause for both the temperature (Fig. 3–5a) and ozone (Fig. 3–5b) assimilation experiments. They present roughly a 10% further error reduction obtained from the additional assimilation of posterior observation. This indicates that, below 20 km, similar error corrections can be expected from the assimilation of temperature and the assimilation of ozone, regardless of the temporal distribution of observations (see also Figures 3–3a and 3–3b). Above 20 km, opposite impacts are obtained between the temperature and ozone assimilations. The assimilation of posterior temperature observations degrades the polar vortex winds, whereas posterior ozone observations improve them. This probably owes to the fact that the EnKF MIPAS temperature assimilation already strongly corrects the polar vortex winds (Fig. 3–3a), while the EnKF MIPAS ozone does not (Fig. 3–3b). There is therefore potential for improvement with assimilation of posterior ozone observation but not for the assimilation of

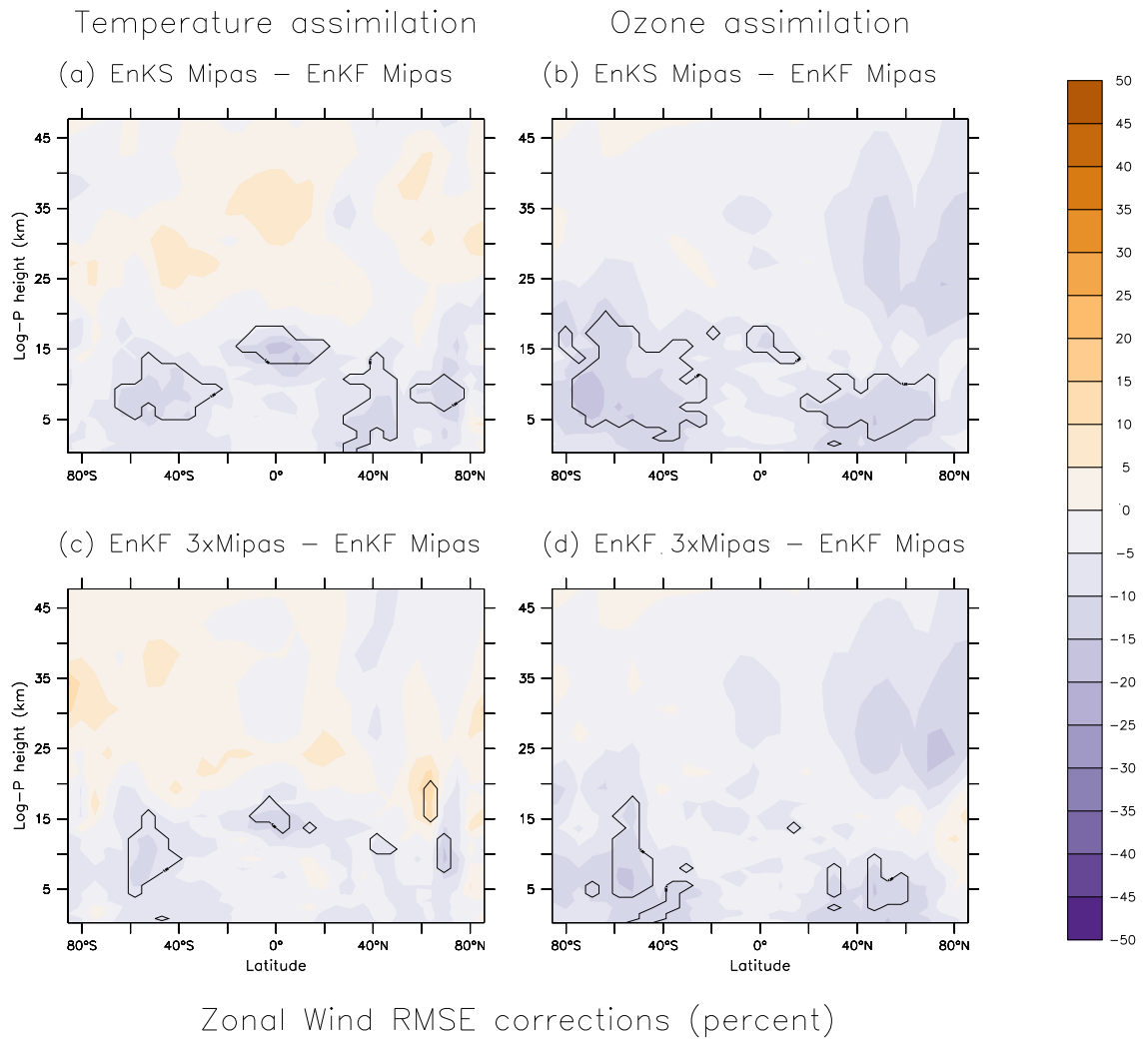


Figure 3–5: Zonal-mean zonal wind Δ RMSE difference (in %) between the EnKS MIPAS and the EnKF MIPAS (top row) and between the EnKF 3×MIPAS and the EnKF MIPAS (bottom row) for temperature assimilation (left column) and ozone assimilation (right column). Purple (orange) colors indicate improvement (degradation) of the EnKS MIPAS or EnKF 3×MIPAS over the EnKF MIPAS. Statistically significant differences at the 95% confidence level are enclosed by the black lines.

posterior temperature observations. However, these differences are not statistically significant and their importance should thus be minimized.

The EnKF 3×MIPAS experiment serves as a comparison for the EnKS MIPAS to see the difference between assimilating additional data synchronously (spatially) and asynchronously (temporally). The bottom row of Figure 3–5 gives the zonal-mean zonal wind Δ RMSE difference between the dense observation network EnKF 3×MIPAS experiment and the reference EnKF MIPAS experiment. The EnKF 3×MIPAS temperature assimilation impact on the wind error (Fig. 3–5c) is not much different from the EnKS MIPAS temperature assimilation impact. There is however a little less further constraint on the winds from the additional spatial temperature data in the subtropical troposphere and a small but significant deterioration in the lower regions of the polar vortex. Overall, this tells us that there is valuable and available additional information in future temperature observations that the EnKS is able to use to further constrain the EnKF MIPAS analysis. The Smoother does so at least as well the Filter in this case, if not better.

The relative impact on the wind analysis from assimilating additional stratospheric ozone observations spatially (Fig. 3–5b) or temporally (Fig. 3–5d) is mostly positive. The EnKF 3×MIPAS ozone assimilation produces beneficial analysis increments everywhere, similar in structure and magnitude to the ones from the EnKS MIPAS ozone assimilation. The only difference between both assimilations is in the size of the regions of significant differences with respect to

the reference EnKF analysis. The EnKS MIPAS has larger regions of statistically-significant improvements than the EnKF 3×MIPAS. It is therefore safe to say that the Smoothing approach represents a viable ozone assimilation alternative to constrain the winds when additional synchronous observations are unavailable.

The impact of synchronous and asynchronous assimilation on the temperature and ozone analysis is shown in Figure 3–6 and Figure 3–7, respectively. Additional temporal temperature observations yield more similar Δ RMSE structures for temperature than for winds (Figs. 3–6a versus Figs. 3–5a) where all regions above 20 km are degraded on average and all regions below are improved. The Δ RMSE magnitudes and regions of statistical significant differences are however very different. The deterioration of the polar vortex and tropical upper stratosphere in the Smoother analysis is here significant and of important magnitude. In particular, there is a 20% degradation of the polar vortex and tropical upper stratosphere temperatures when posterior temperature observations are assimilated (Fig. 3–6a). Also, the regions of significant improvement of the temperatures by the EnKS MIPAS temperature assimilation have essentially disappeared. Consequently, the assimilation of posterior temperature observations has no further benefits on the temperature analysis and only drawbacks in the upper part of the stratosphere. On the contrary, the EnKF 3×MIPAS temperature assimilation case displays a significant temperature improvement in the tropical upper and lower stratosphere (Fig. 3–6c). This is probably from the finer horizontal resolution in the observation network that helps determining the smaller-scale dynamical

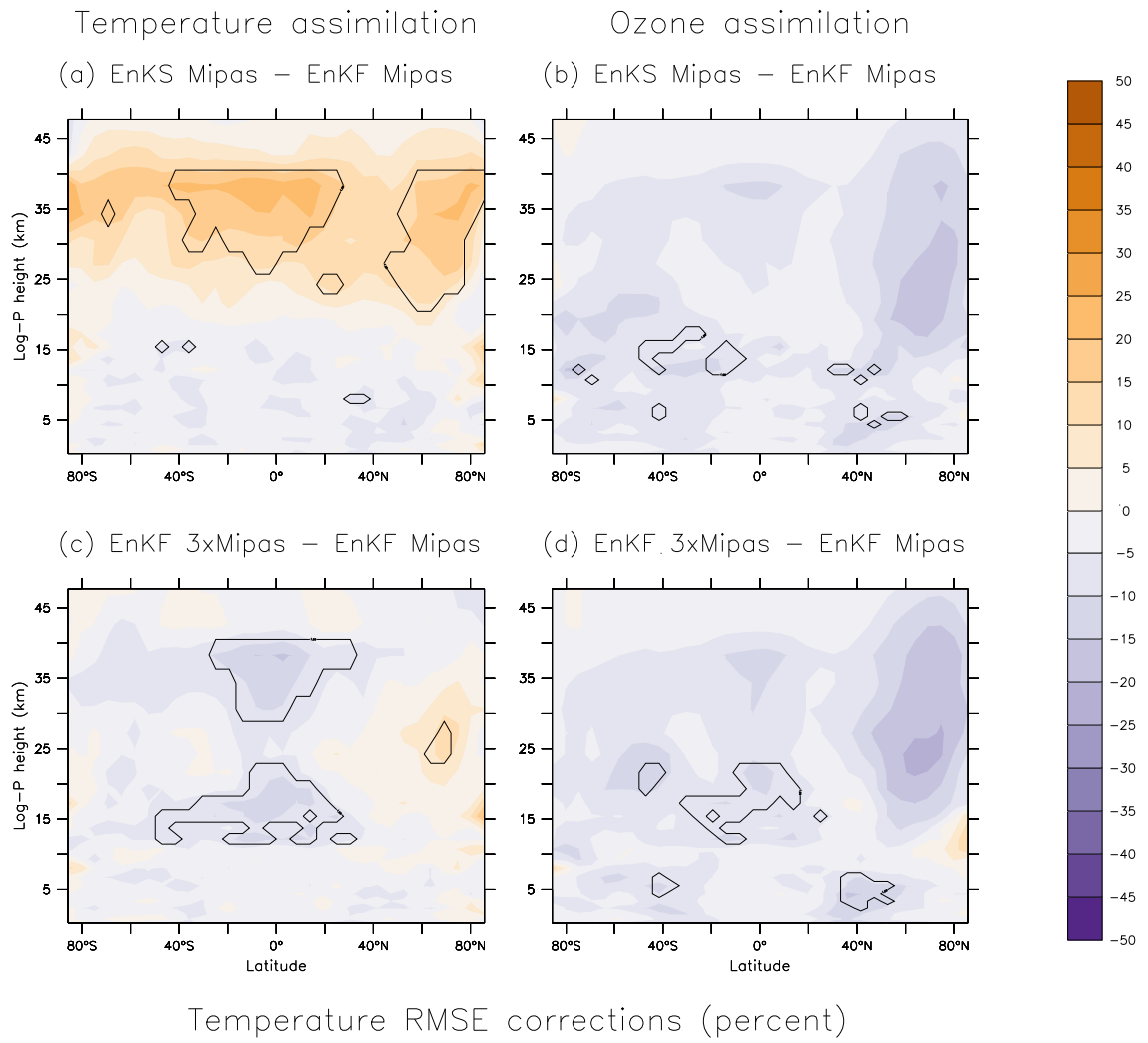


Figure 3–6: Same as Figure 3–5 but for the zonal-mean temperature Δ RMSE differences

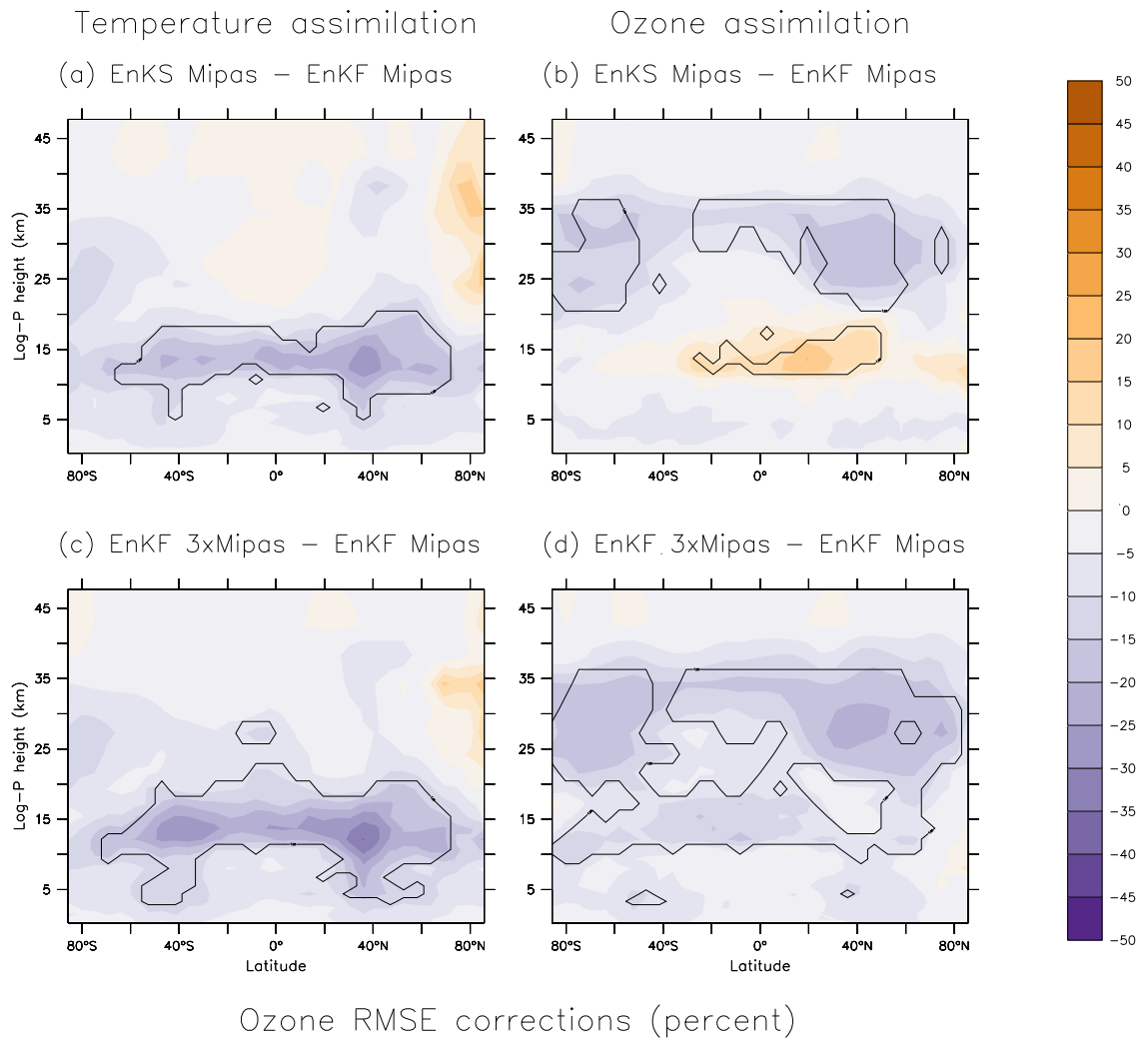


Figure 3–7: Same as Figure 3–5 but for the zonal-mean ozone mixing ratio Δ RMSE differences

features proper to the tropics. It however also displays a small but significant degradation in the polar vortex temperature analysis.

The assimilation of additional synchronous temperature observations with the EnKF 3×MIPAS and additional asynchronous observations with EnKS MIPAS both further constrain the EnKF MIPAS ozone analysis in the UTLS region outside the poles (Figs. 3–7a and 3–7c). This implies that time-lagged $T - O_x$ background-error covariances convey the beneficial temperature-to-ozone information nearly as well as synchronous background-error covariances.

The impact of synchronous and asynchronous ozone assimilation on the temperature (right column of Fig. 3–6) follows the general correction structures obtained for the impact on the wind analysis. The assimilation of additional posterior ozone observations produces generally beneficial temperature analysis increments (EnKS Mipás of Fig. 3–6b), albeit noisier than the temperature analysis increments from assimilation of additional spatial ozone data (EnKF 3×MIPAS of Fig. 3–6d). This is reflected in the limited extent of regions displaying significant differences for the EnKS MIPAS compared to the EnKF 3×MIPAS, particularly near the cold-point tropopause region and the subtropical troposphere.

The improvement from adding synchronous ozone observations on the ozone analysis (Fig. 3–7d) have a pronounced beneficial effect in the mid stratosphere. It is strongest in the mid-stratosphere and equatorial UTLS which are not well constrained by the reference EnKF MIPAS experiment (see Fig. 3–3f). Such a potential ozone improvement is not as notable from the EnKS MIPAS ozone assimilation though. The additional error corrections from the EnKS MIPAS are

also significant and of similar magnitudes in the mid-stratosphere compared to the EnKF 3×MIPAS ones (Fig. 3–7b versus Fig. 3–7d) but a significant degradation is witnessed in the lower stratosphere near 15 km in altitude. The EnKS MIPAS ozone assimilation confirms the difficulty seen with the EnKS MIPAS temperature assimilation for the stratospheric Smoother to extract information from posterior observations through the time-lagged auto-covariances ($O_x - O_x$ or $T - T$).

3.5 Conclusions

The goal of this study was to investigate the potential benefits of a Smoothing approach where posterior observations are assimilated in order to further improve the model state analysis. This was done using dynamical and chemical data assimilation in an idealized perfect-model experiment setup. An Ensemble Kalman Smoother (EnKS) based on Evensen and van Leeuwen (2000) was developed and applied to the IGCM-FASTOC chemistry-climate model. The system is identical to the one in Milewski and Bourqui (2011) except for a few changes in localization parameters and the fact that all available observations from a typical daily MIPAS network are assimilated simultaneously, instead of in successive observation batches following Houtekamer and Mitchell (2001). Instabilities arose in the EnKS analysis when using the sequential assimilation of observations by batches, which led us to assimilate all observations at once. A sparse-matrix treatment of the background-error covariances was implemented to keep the EnKS computationally competitive.

The Smoothing Problem was approached with the optic of detailing the properties and potential of the EnKS update. To separate the effects of the

analysis and the forecast in the data assimilation cycle, relative difference of RMSE (Δ RMSE) between analyses and forecasts were produced and examined.

Understanding the impact of assimilating posterior observations required a prior knowledge of the assimilation impact obtained by the reference EnKF. As expected from Milewski and Bourqui (2011), stratospheric ozone assimilation with an EnKF was found to constrain the dynamical state globally with larger benefits for the UTLS and tropospheric jets regions. The beneficial impact of an EnKF ozone assimilation on the ozone state is enhanced compared to its impact on the dynamical state and extends to the mid-stratosphere. Stratospheric EnKF temperature assimilation constrains the UTLS comparably to the ozone assimilation. It is particularly effective on dynamical variables in the polar vortex and tropospheric jets. It provides however a limited effect on the ozone error which is restricted to the tropospheric jet region. The EnKF temperature and ozone (synthetic) MIPAS observation assimilation experiments showed a globally beneficial impact on the mid-stratosphere chemistry and dynamical error constraint.

A first set of EnKS temperature or ozone assimilation experiments characterize the constraint on the forecast errors that posterior observations provide, compared to current observations, by introducing a time-lag between the analysis and the observations. The EnKS assimilations display an increasing loss of impact with time-lag. As a result, asynchronous posterior observations do not provide the same constraint on the analysis as a similar amount of synchronous observations. It was found that EnKS assimilation with a 48-hour time-lag started to produce

minimally deleterious analysis wind increments, particularly for temperature assimilation. That motivated our choice of attempting further EnKS experiments with assimilation of data from two posterior days in addition to current-day data assimilation.

A second set of experiments was performed with the EnKF, the EnKS, and the EnKF with a denser observation network composed of three daily MIPAS networks. The denser-network EnKF assimilates the same amount of observations on the same grid points as the EnKS does, and provides a meaningful comparison for the quality of the EnKS impacts. The impact of assimilating additional observations posterior to the analysis time with the EnKS is not ubiquitous. It was actually found that EnKS assimilation provides relatively small but significant further improvements on the reference EnKF analysis in parts of the lower stratosphere and troposphere but only for variables other than the assimilated one. The EnKS assimilation of posterior temperature observations caused important degradation on the reference EnKF temperature analysis in the polar vortex and tropical mid-to-upper stratosphere. The ozone assimilation with EnKS did provide further improvement on the reference EnKF ozone analysis in the mid-stratosphere, but also notable ozone degradation in the lower stratosphere. Apart from this difficulty of the Smoother, the comparison of the EnKS temperature and ozone assimilation impact to the denser-network temperature EnKF assimilation impact revealed that the cross-variable (e.g., temperature on winds and ozone, ozone on temperature and winds) gains made by the Smoother were very valuable as they were similar to the gains made by the Filter. We do not find remarkable

added value from assimilating future observations over assimilating additional current observations. However, the Smoother does provide a viable alternative to the Filter in some contexts if additional synchronous observations are not available.

This study was motivated in part by the need to obtain meaningful long-term reanalyses representing stratospheric dynamics and chemistry. Considering the sparseness of observations in the stratosphere before and even during the recent satellite era, the proper assimilation of readily-available observations posterior to the (re)analysis time could be precious. The idealized environment in which this study is cast renders the results obtained as only indicative of possible benefits the EnKS may bring to stratospheric chemical-dynamical assimilation. Other challenges need to be assessed such as accounting for model errors and biases or instrument biases before the results can be affirmative.

CHAPTER 4

Constraining a Stratospheric Sudden Warming with Ensemble Kalman Filter Ozone assimilation

The results from the two previous chapters focused on the multivariate characteristics of the ensemble data assimilation system once it has reached a stationary evolution in analysis error and ensemble spread. This Chapter focuses on the transient period from the first assimilation time to the stationary phase, and particularly how the EnKF responds to initially-biased forecast conditions. A stratospheric sudden warming event self-generated from the IGCM-FASTOC is chosen here to represent the true state of the atmosphere. It is a simple, yet essential, experiment to evaluate the potential of the EnKF to constrain the dynamical state from the assimilation of ozone observations in highly perturbed conditions.

This chapter of the thesis is a short scientific letter prepared to be submitted to Geophysical Research Letters, Milewski, Thomas and Michel S. Bourqui, 2012: Constraining a Stratospheric Sudden Warming with Ensemble Kalman Filter ozone assimilation.

Constraining a Stratospheric Sudden Warming with Ensemble Kalman Filter Ozone Assimilation

Thomas Milewski and Michel Bourqui

Department of Atmospheric and Oceanic Sciences, McGill University

Montréal, Qc, Canada

Abstract

A pair of perfect-model Ensemble Kalman Filter (EnKF) ozone assimilation experiments are performed to investigate the ability of ozone observations to constrain the stratospheric Polar Vortex winds and temperatures even in the presence of strong initial forecast deviations. The true state of the atmosphere is defined to be a major Stratospheric Sudden Warming (SSW) splitting event self-generated by the IGCM-FASTOC chemistry-climate model. It is found that the ensemble of analyses converge with similar speed and accuracy onto the SSW true state whether the initial ozone forecast bias is of the order of one standard ensemble deviation or peaking at more than 6 standard ensemble deviations. This demonstrates the robustness of chemical-dynamical coupling in an EnKF system.

4.1 Introduction

Particular interest has been devoted to Stratospheric Sudden Warmings (SSW) lately, with three events of unprecedented magnitude having occurred over the last decade. SSWs are the most dynamically intense events in the middle atmosphere. Under favorable conditions, planetary Rossby waves originating from the troposphere propagate upwards into the stratosphere and eventually break when reaching their critical layer, depositing their momentum (Shepherd, 2000). When this momentum deposition is anomalously strong and poleward, the stable polar night vortex structure may deform, be displaced from the pole (“wave-one” events), or split (“wave-two” events) and be temporarily replaced by a warm anticyclone. In the process, the polar-cap (50°N to 90°N area-averaged) temperatures increase abruptly and the mid-stratospheric vortex zonal flow (defined as the 10 hPa zonal-mean zonal winds at 60°N) may reverse from westerly to easterly, in which case the SSW is labeled as a “major” event (Charlton and Polvani, 2007). SSW events in turn affect the troposphere on daily to weekly timescales (Baldwin and Dunkerton, 2001) explaining in part the recent inclusion of a fully-resolved stratosphere in operational numerical weather prediction (NWP) models.

The three important SSW events of the last decade all have their specificities. The Antarctic Sudden Warming of 2002 was the only Southern Hemisphere SSW on record, dating back to 1957 (Roscoe et al., 2005, see also the the Journal of the Atmospheric Sciences March 2005 special issue on to this event). The Arctic polar vortex displacement event of 2006 was already among the strongest on

record (Manney et al., 2008) but was superseded in magnitude and duration by the vortex splitting event of 2009 (Manney et al., 2009). These cases have already been a fertile ground for research, validation and intercomparisons of various data assimilation systems (DAS), applied to models of different complexity. These range from middle-atmosphere general circulation models (GCM) or chemistry-climate models (CCM) to operational NWP models or reanalyses. In particular, the 2002 event was simulated with the CMAM-DAS CCM (Ren et al., 2008). The unobserved upper stratosphere and mesosphere in this high-lid model were constrained during the forecasts by the upward propagation of information from the constrained lower stratosphere via the gravity-wave drag scheme. The 2006 event was reconstituted with the CMAM-DAS (Ren et al., 2011) and NOGAPS-ALPHA GCM (Hoppel et al., 2008; Coy et al., 2009) middle-atmosphere research data assimilation systems (DAS). In the CMAM-DAS, the upper stratosphere is again constrained only through the gravity-wave drag scheme while the NOGAPS-ALPHA assimilated limb-sounding MLS and SABER data ranging up to 80 km. For the same event, the operational GEOS-5 and ECMWF analyses were compared to the independent (unassimilated) MLS and SABER data in Manney et al. (2008). The vertical limit of the operational models and nadir-sounding ATOVS temperature data assimilated prevented the capture of the full vertical extent of the SSW. In particular, it did not reflect the mesospheric cooling and stratopause disintegration and later reformation at higher altitudes, as seen in limb-sounding instruments. The 2009 event was studied with the JCDAS (Harada et al., 2010) and the GEOS-5 (Manney et al., 2009). Martineau and Son (2010)

also compared five different 2009 SSW event reanalyses to the COSMIC GPS Radio-Occultation temperature data.

These events provide an overview of the quality of stratospheric analyses and the challenges that DAS still face in the stratosphere. They include biases, sparseness in the observing network and the proper specification of error covariances, among others (Polavarapu et al., 2005b). Stratospheric temperature observations are not as easily exploitable as their tropospheric counterparts. For example, the upper channel of the nadir-sounding AMSU-A (part of ATOVS) instrument peaks at 1 hPa and has a broad weighting function giving temperature retrievals with poor vertical resolution in the upper stratosphere. The bias in satellite observations in the stratosphere is hard to determine considering the lack of in-situ observations for validation. The situation for wind data available for assimilation is even worse as they are only observed below 10 hPa on the sparse network of in-situ radiosonde and aircraft data. Winds are completely unobserved in the highly-variable middle and upper stratosphere regions where models display significant biases (Eyring et al., 2006). However, the proper specification of error covariances can potentially alleviate the lack of wind observations. During the data assimilated step, information is transferred between observed variables to unobserved ones by means of error covariances. Depending on the DAS, the wind correction during the assimilation step may happen in different ways:

- In 3D-Var, geostrophic balance, where applicable, is generally captured in the mass-wind cross-covariances, so temperature observations can constrain

the winds. However, the error covariances are static and do not reflect the current state of the atmosphere.

- In 4D-Var, in addition to similar constraint as in 3D-Var, the adjoint of the TLM propagates analysis increments from the end of the assimilation window to the beginning, adjusting all the (linear) balances in the process. For example, the winds are adjusted from analysis increments in ozone through the tracer transport equation (Semane et al., 2009).
- In the EnKF, error covariance are calculated from an ensemble of forecasts and include multivariate cross-covariances that transfer information from the observation innovations to the analysis increments. Error covariances need to be properly localized to remove spurious sampling noise caused by the finite size of the ensemble.

In addition to the impact on the winds during the data assimilation step, the ensuing forecast will also readjust balances (Daley, 1991).

Notable scientific research efforts have been attempted on comprehensive lower-resolution models (CMAM-DAS or NAVY-NOGAPS) to investigate some of the stratospheric data assimilation challenges. This study follows along these steps to demonstrate a use of multivariate ensemble-based assimilation for obtaining a good representation of SSW events in analyses through the assimilation of ozone observations and its constraint on stratospheric winds. The setup used in this study follows that of Milewski and Bourqui (2011), an idealized perfect-model (identical-twin) Observation System Simulation Experiment with assimilation

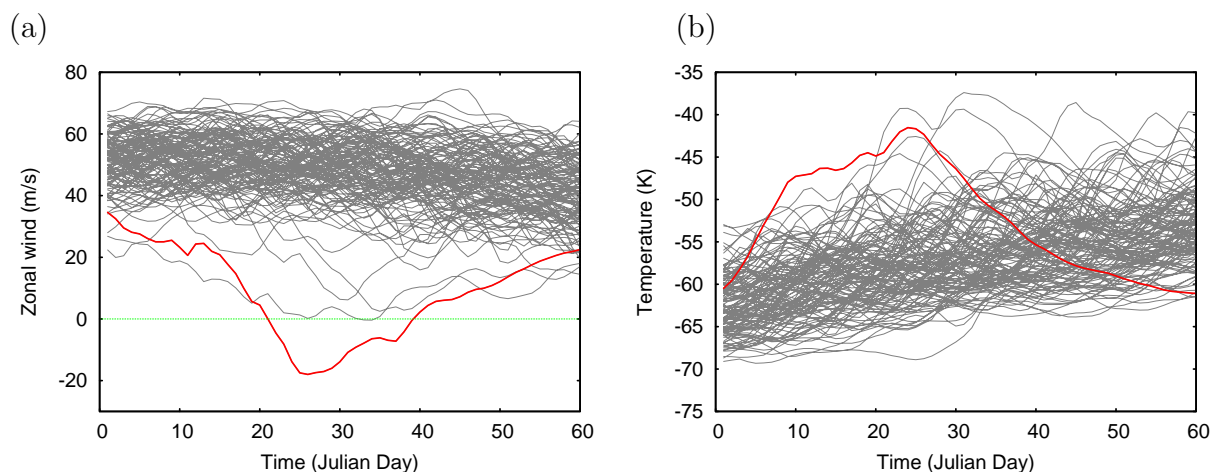


Figure 4–1: Time evolution of the 12-hPa zonal-mean (a) zonal wind at 58°N and (b) polar cap temperature (area-averaged from 50 to 85°N) for the 128 climatological ensemble members (grey curves) and the stratospheric sudden warming true state (red curve). The zero-wind line is in green in panel (a).

of stratospheric limb-sounding ozone retrievals only (no conventional data assimilated). The true state is a SSW vortex-splitting event self-generated in the IGCM-FASTOC CCM (Taylor and Bourqui, 2005).

4.2 Self-generated Stratospheric Sudden Warming Event

Figures 4–1 shows the IGCM-FASTOC climatological ensemble composed of January 1st to March 1st time-sections (grey curves) from a 129-year time-slice simulation, for the 12-hPa zonal-mean zonal winds at 58°N (Fig. 4–1a) and 50°N to 85°N area-averaged temperatures (Fig. 4–1b). The IGCM-FASTOC model with T21 horizontal resolution, 26 vertical levels reaching up to 0.1 hPa and prescribed surface temperatures generates a single clear major SSW event (red curve) in the 129 simulated years. Three other cases could qualify as minor events based on their strong and rapid polar temperature increase but fail to have

reversal of the vortex zonal flow. For the major SSW event, the polar vortex is initially weak (negative bias of 18.8 m.s^{-1} compared to an ensemble spread of 15.5 m.s^{-1}) and relatively warm (3.7 K bias for a 7.7 K ensemble spread) with respect to the climatological ensemble average at day 1, but the flow soon becomes strongly easterly. The reversal of the mid-stratosphere polar vortex zonal winds criterion (green line) is fulfilled starting day 21 until day 39, with a maximum zonally-averaged easterly flow nearly reaching 20 m.s^{-1} .

The evolution of the geopotential height field at 10 hPa is shown in Figure 4–2. In the vortex weakening phase (day 1 to 15), the Aleutian High and the anticyclone over the Atlantic deform the polar vortex to create within it two distinct closed circulations. On day 20, the polar vortex splits showing a clear quadrupole structure in the height fields. The two anticyclones merge to form a single crest over the North Pole (days 25 and 30). The newly-formed anticyclone eventually weakens (day 35) and is replaced by the re-formed polar vortex (day 45) that intensifies afterwards (day 55). This is clearly a vortex-splitting event and the Polar Vortex wind-reversal period (day 21 to 39) coincides well with the anticyclone settling over the Pole.

Note that the recurrence frequency of SSW within the IGCM-FASTOC is much lower than in the real stratosphere (6 SSW per decade) and other stratosphere-resolving GCMs (Charlton et al., 2007). The horizontal resolution and the interactive surface temperatures in the model play an important role in the generation of upward-propagating tropospheric waves responsible for the weakening of the polar vortex (Winter and Bourqui, 2011). Although this

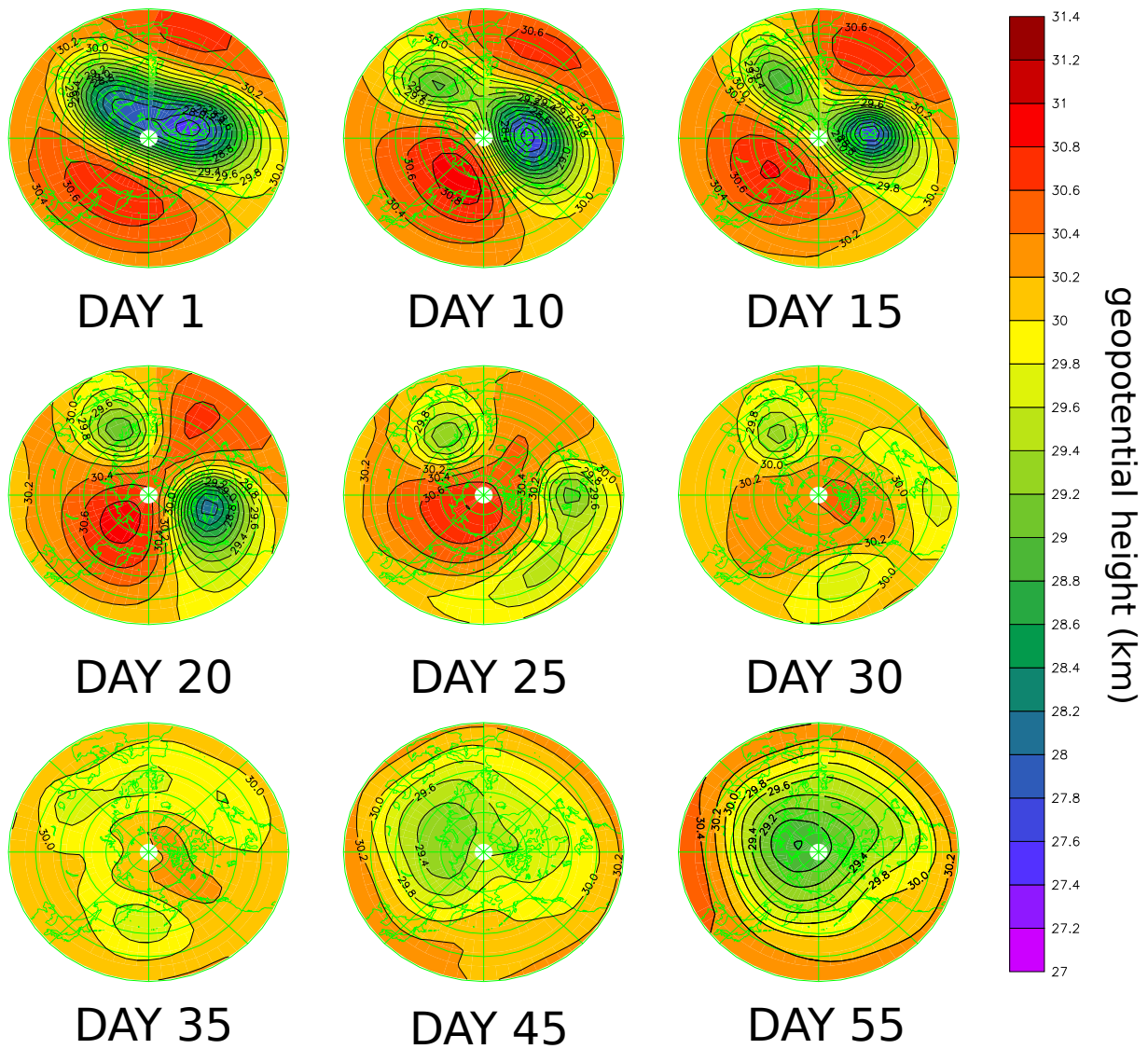


Figure 4-2: Evolution of the 10-hPa geopotential height field for the stratospheric sudden warming case in polar stereographic view between 30 and 90°N. Latitudes circles are marked in green every 10° starting from 30°N. Geopotential height contours intervals are set to 200m.

version of the IGCM-FASTOC does not display a realistic annual variability in polar vortex strength, the single major SSW event allows to perform an ensemble data assimilation experiment where the SSW is chosen as the true state of the atmosphere. Observations are sampled from this true state and the remaining 128 simulations are used as forecast ensemble members. This allows to test the possibility to constrain the stratospheric winds to the SSW state with assimilation of ozone retrievals in the presence of a biased initial ensemble.

4.3 Ozone Assimilation

The EnKF experiments follow the experimental setup of Milewski and Bourqui (2011). It involves the assimilation, every 24 hours at 00Z, of a daily coverage of ozone MIPAS-like retrievals, sampled from the SSW simulation and perturbed with unbiased random Gaussian noise with 10% error standard deviation. The observations cover one third of the horizontal model grid points (an observation every three longitudinal grid points and every latitudinal grid points) for the 11 stratospheric levels between 180 and 4 hPa (roughly 12 to 38 km in altitude). Observational errors are assumed uncorrelated, yielding a diagonal observation-error covariance matrix. The ensemble data assimilation filter used here is a perturbed-observations 128-member Double-EnKF with sequential assimilation by batches of 100 observations following Houtekamer and Mitchell (2001). Covariance localization is applied separately in the horizontal and vertical directions with respective decorrelation lengths of 5600 km and 4 scale heights (Milewski and Bourqui, 2011). No artificial inflation is necessary owing to the absence of model errors (perfect-model setup), the relatively high ensemble size

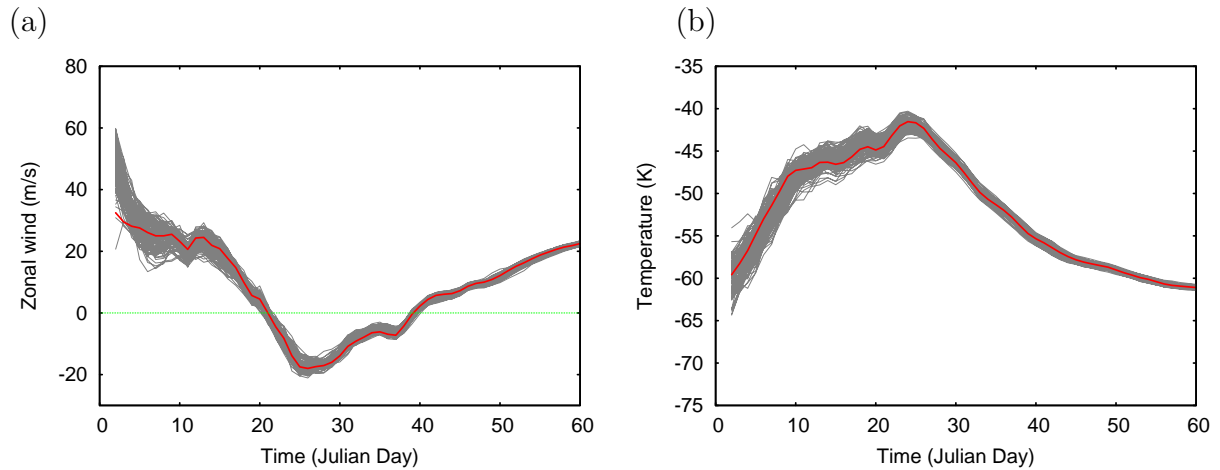


Figure 4-3: Same as Fig. 4-1 but for the ensemble of zonal-mean (a) zonal wind and (b) polar cap temperature analyses from the Ensemble Kalman Filter daily assimilation of synthetic MIPAS ozone retrieval starting on day 1.

(128 members), covariance localization and a relatively sparse observing network. This combination of factors yields analysis ensemble spreads naturally larger than analysis errors. Ensemble-calculated forecast-error covariances include multivariate (cross) covariances describing the instantaneous relationship between different variables (e.g., ozone and winds), and allowing the transfer of information from observed to unobserved variables.

4.3.1 Assimilation Starting Prior to Wind-reversal Time

In the first EnKF experiment, observations are assimilated from day 1 onward and the ensembles of 10-hPa zonal wind and temperature analyses at 60°N are displayed in Figures 4-3a and 4-3b, respectively. In comparison with the (unconstrained) climatological ensembles of Fig. 4-1 where the true state (red curve) was a clear outlier, the analysis ensembles constrained by ozone

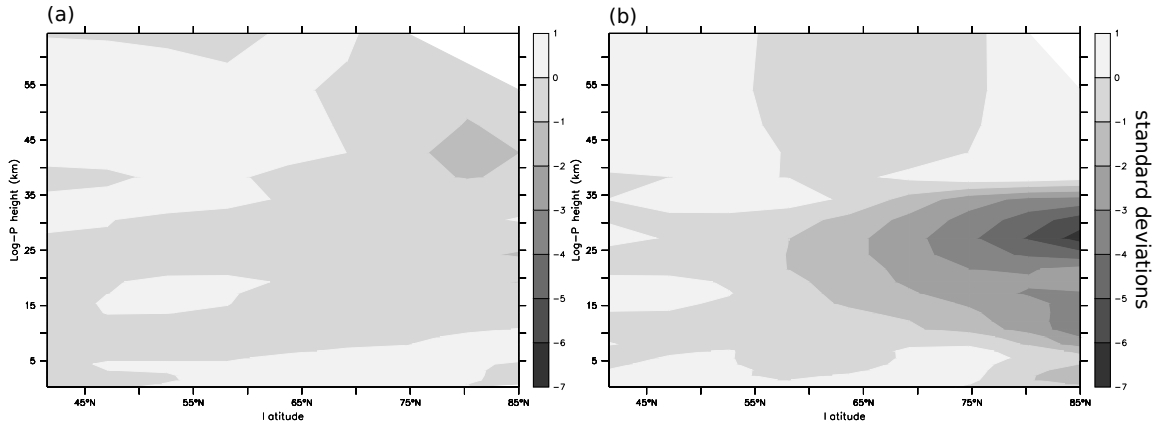


Figure 4-4: Latitude-height cross-section of the climatological ensemble ozone deviation with respect to the true state (a) prior to stratospheric sudden warming (day 1) and (b) at time of Polar Vortex wind reversal (day 21), normalized by the climatological ensemble spread (in standard deviations).

observations follow closely the true state. The initial bias in winds in the ensemble of Fig. 4-3a is reduced in the first few assimilation steps and the true (SSW) state lies centered inside the ensemble afterwards. The spread of the ensemble also shrinks with time, indicating the confidence of the EnKF in its depiction of the SSW state.

This assimilation experiment which started on day 1 shows the ability of the EnKF to transfer the information from the incompletely-observed ozone state under SSW conditions to the wind and temperature variables. The initial forecast biases are however not very pronounced (18.8 m.s^{-1} and -3.7 K compared to ensemble spreads of 15.5 m.s^{-1} and 7.7 K) and the analysis ensemble adjusts quickly.

4.3.2 Assimilation Starting at Wind-reversal Time

In the second data assimilation experiment, the assimilation is started at day 21 when the mid-stratosphere polar vortex zonal winds switch from westerly to easterly. This is an opportunity to test the EnKF behavior when subject to much larger initial biases (49.9 m.s^{-1} and -20.33 K compared to ensemble spreads of 17.08 m.s^{-1} and 9.7 K). Particularly relevant to the assimilation problem is the forecast bias in the observed variable as it contravenes the “unbiased prior” assumption imposed when deriving the Kalman Filter equations. Figure 4–4 shows the climatological ensemble ozone bias at for days 21 and 1. At day 21, the Polar Vortex clearly shows in the ozone bias. For all latitudes, there is a maximum at 30 km altitude, with increasing negative ozone biases towards the North Pole, culminating at 6.7 times the ensemble spread at 85°N and 27 km. In comparison, the ozone biases 20 days before the Polar Vortex wind-reversal data are always within plus or minus one ensemble standard deviation in the vertical range where observations are assimilated.

To verify if a high negative bias in the observed variable forecast prevents the EnKF ozone assimilation to constrain the SSW, the evolution of the ensemble polar vortex zonal winds and polar cap temperatures analyses are shown in Figure 4–5. Both zonal winds and temperatures actually converge to the true (SSW) state (red curve) without any significant bias, similar to the assimilation experiment starting before the SSW central date (Fig. 4–3). The convergence towards the stationary wind and temperature error with respect to the true state takes 4.5 days and 5 days, respectively (from the e -folding times of an exponential decay

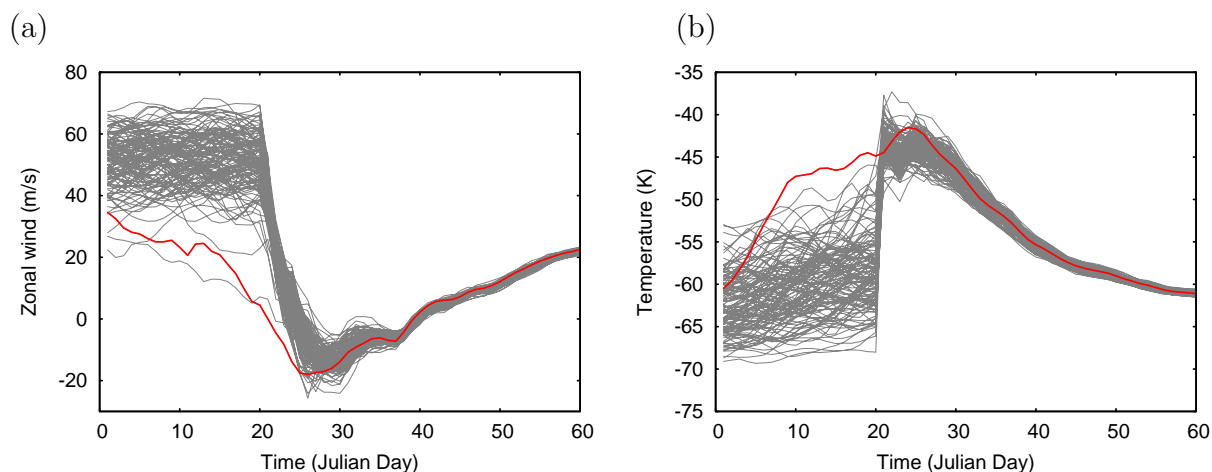


Figure 4-5: Same as Fig. 4-1 but for the ensemble of zonal-mean (a) zonal wind and (b) polar cap temperature analyses from the Ensemble Kalman Filter daily assimilation of synthetic MIPAS ozone retrieval starting on day 21.

fit). This is long for NWP purposes but the focus of the study is not to accurately depict the stratosphere but to investigate the behavior of the EnKF in unusual conditions. In that respect, the ability of the EnKF to adjust to initially strongly-biased dynamical states from the assimilation of a chemical tracer only is quite remarkable.

4.4 Conclusion

Two perfect-model assimilation experiments were performed to demonstrate the potential of ensemble assimilation of ozone observations to constrain an unusual dynamical event : a major stratospheric sudden warming splitting event, self-generated by the IGCM-FASTOC model. This event is actually highly unusual as it is the unique SSW event in the 129-member IGCM-FASTOC climatological ensemble. This permitted to test the multivariate response of the EnKF when subject to prior forecasts that are close or far away from the true state. This was

done by starting the assimilation 19 days before the SSW Polar Vortex wind-reversal time and at wind-reversal time. Both assimilation experiments yield similar quick convergence to the stationary analysis solution, this even though the second experiment is initiated with a bias as high as six times the ensemble standard deviation. This strongly reinforces results from the previous study by Milewski and Bourqui (2011) where the capacity of the ozone-wind error covariance to convey information from the ozone observation innovations to the wind analysis increments was demonstrated.

Note that the EnKF ozone assimilation convergence towards an outlier state may not be effective for all combinations of prior ensemble biases and spreads. In our case, the climatological prior ensemble has large variability, implying low weight in the EnKF. This allows the observations to conduct the analysis ensemble towards the right state. The application of the EnKF to an initial forecast ensemble with smaller spread but large bias with respect to the state is likely to be subject to filter divergence. Artificial inflation may be an alternative to increase the ensemble spread and obtain convergence on an outlier state.

CHAPTER 5

Conclusions

The main hypothesis of this study is that ensemble data assimilation could play a critical role in obtaining a better representation of the instantaneous state of the stratosphere. The data assimilation process is essential to obtain the best estimate of a system. This also holds for stratospheric data assimilation even though it presents a few particularities. Models exhibit biases accountable in part on their reliance on parametrization of unresolved gravity waves that interact with the mean stratospheric flow. One of the deficiencies of the observation network is that the stratospheric wind field is only measured in the lowermost stratosphere and sparsely so. This is where ensemble data assimilation may prove useful, as it provides a method to calculate flow-dependent ensemble error covariances that transfer weighted information from the observations to all correlated state variable with the possibility to constrain them.

This doctoral study represents a first attempt at assimilating both stratospheric chemical and dynamical observations with an ensemble data assimilation scheme with a coupled chemistry-climate model. It investigates specifically the capacity of Ensemble Kalman Filters and Smoothers assimilating available stratospheric observations to impact and constrain the different variables of the model state. The experiments in this work are performed in an idealized perfect-model

Observation System Simulation Experiment (OSSE) setup with the IGCM-FASTOC model (Taylor and Bourqui, 2005) providing the ensemble of forecasts as well as the true state of the atmosphere from which (synthetic) observations are sampled. Perfect-twin OSSEs are a necessary first step to develop a data assimilation system as they allow to set aside the problems incurred with model errors to concentrate on investigating the specific behavior of the (ensemble) data assimilation system.

The major achievement of this doctoral study is the implementation of a stable ensemble data assimilation system (EDAS) able to constrain the global coupled chemical-dynamical system. The ensemble data assimilation scheme chosen is a stochastic perturbed-observation Ensemble Kalman Filter with two sub-ensembles of 64 members similar to the filter of Houtekamer and Mitchell (2001). Throughout the study, the observations assimilated are synthetically generated from the true model run, mimicking limb-sounding MIPAS temperature and ozone retrievals with characteristic data coverage and error statistics. The application of the EnKF to this coupled chemical-dynamical model required to optimize the covariance localization parametrization. This strongly affects the stability and overall performances of the EnKF system. In fact, the absence of covariance localization directly led to filter divergence and system failure (Fig. 2–1b). Covariance localization is separately applied horizontally and vertically as customary in EnKF systems and different optimal decorrelation length parameters were obtained for temperature and ozone error covariances. Multiple pairs of horizontal and vertical localization parameters actually allowed for the EnKF

system to reach a stationary evolution in ensemble spread (SPREAD) and error (RMSE), with no hint of potential filter divergence. The EnKF analyses converged to minimum errors in global total energy norm for optimal values of localization parameters (Fig. 3–1). Relatively long decorrelation length parameters were optimal for temperature covariances $[C_h, C_v]=[14000 \text{ km}, 10 \Delta \ln(P)]$, while much shorter values proved optimal for ozone $[C_h, C_v]=[5600 \text{ km}, 4 \Delta \ln(P)]$. These optimal parameters values are much longer than the $[C_h, C_v]=[2800 \text{ km}, 2 \Delta \ln(P)]$ values chosen by Houtekamer and Mitchell (2001). This reflects the dependence of the covariance localization on the observing system. The sparse stratospheric network involved here requires long decorrelation lengths in order to maximally exploit the observations and spread their information as far as possible, particularly vertically due to the absence of data in the troposphere. Also, the natural dynamical correlation lengths are typically longer in the stratosphere than in the troposphere. Moreover, the very relaxed localization imposed on the ensemble-calculated error covariances better retains their natural correlation patterns. This is ideal for a system that relies on the error covariances to constrain the unobserved variables. On the contrary, a too severe localization is likely to damage the natural correlation patterns and introduce imbalance (Oke et al., 2007). Once the ensemble data assimilation system was well configured, it became possible to concentrate on the main objectives of the study.

The primary objective of the study is to characterize the potential multivariate constraints in an EDAS by looking at the impact that observations have on various variables of the model state. An effort was made to distinguish the relative

contribution brought by the analysis step and the forecast step (see schematics of Fig. 2–5). This was done by comparing the time-averaged analyses errors from experiments with nullified chemical-dynamical error covariances to experiments with the full error covariance matrices (Chapter 2) and by comparing the forecast and analysis errors with time-averaged diagnostic results (Chapter 3). The results yielded some very promising properties of a stratospheric EDAS, listed below.

The impact of assimilating stratospheric temperature observations during the analysis step is strongly felt on the dynamical variables (temperature and wind) in regions of strong dynamical variability such as the Polar Vortex or the tropospheric jets (Figs. 3–3a and 3–3c). The analysis-step impact on the ozone state is weak and is limited to weakly constraining the tropospheric jets (Fig. 3–3e). However, the analyzed winds and temperatures are able to correct the ozone state during the forecast step (Fig. 2–3b) through improved transport and chemistry. The inverse is not true, as the analyzed ozone state is not able to improve the dynamical state during the forecast step as radiation is not effective over the 24-hour forecast period. The ozone assimilation impact on the dynamical analysis during the analysis step is noticeable but only in the upper troposphere lower stratosphere (UTLS, Figs. 3–3b and 3–3d). However, when looking at the time-integrated effect of the ozone assimilation on the dynamics (Figs. 2–4a and 2–4c), one realizes that the dynamical state is well constrained throughout the atmosphere. This indicates that there is an analysis-to-forecast feedback operating on the dynamical model state through repeated assimilations of ozone observations. Moreover, background ozone-temperature and ozone-wind

multivariate covariances are found to be essential to achieve such a constraint (Figs. 2–4a and 2–4c) and particularly the ozone-wind covariances (Fig. 2–6). This is the single most significant result in this study. It demonstrates the ability of the chemical-dynamical EDAS in producing multivariate error covariances accurate enough for the ozone observations to affect the dynamical model state during the analysis step and obtain a low-error wind analysis. This result extends the studies of Daley (1995); Riishøjgaard (1996); Semane et al. (2009) by involving explicitly the background-error covariances able to represent appropriately the chemical-dynamical coupling.

The impact of assimilating stratospheric ozone observations on the ozone analysis is strongly felt in the UTLS region at all latitudes as well as in the mid-stratospheric extratropical and polar regions (Fig. 3–3f). The above-mentioned ozone-dynamics coupling resulting in better-analyzed dynamics also feeds back onto the chemical state to further improve the ozone analysis (Fig. 2–4b). It is apparent that the complex interplay between dynamics and chemistry in the stratosphere is well exploited by the EDAS as information from a chemical or dynamical observation can constrain specific variables and regions during the analysis step and the analyzed variables can then offer further constraints during the forecast step.

The secondary objective was to test some limits of applicability of the EDAS, always within the perfect-model hypothesis context. The first limit investigated was the impact of introducing a time-lag between observations and analysis. The experiments in Chapter 2 had observations sampled from the true state at

analysis time exactly. This is a coarse approximation with respect to reality and its impact on the analysis needed to be verified. An Ensemble Kalman Smoother (EnKS) was used for this purpose in Chapter 3. It is a simple extension to the EnKF that uses previous EnKF analysis cycles as background states and includes time-lagged background-error covariances to transfer information temporally from the observations to the model state at analysis time. It was generally found that there is decreasing impact on the analysis with increasing observation-analysis time-lag but the structure of the assimilation impact remain similar. There is a greater loss in signal from the temperature-wind time-lagged error covariances than from the ozone-wind error covariances with a strong loss of signal for 48-hour time-lags (Figs. 3–4e and 3–4f). Therefore, within the typical 6 to 12-hour assimilation time window, we expect that observation-analysis time-lags are not too detrimental to stratospheric data assimilation. The EnKS also allowed to estimate the added benefit of a Smoothing Approach (i.e., the inclusion of posterior observations to constrain the analysis) in stratospheric data assimilation. This is particularly interesting for reanalysis projects where posterior data are available and could replace missing data at analysis time. To better evaluate the impact on the analysis of the EnKS assimilating two posterior days of data, an EnKF assimilation with a denser network of observations was also performed as means of comparison. It was found that in most cases the Smoother assimilation provided very similar constraints on the analysis state in magnitude and structure to those obtained by the Filter (dense-network) assimilation. The assimilation of posterior data therefore offers an interesting potential when current data are

not instantly available. The stratospheric Smoother Approach did however suffer from negative assimilation impact on the analysis variable observed (e.g., negative impact on the temperature analysis from assimilation of posterior temperature observations in Fig. 3–6a or on the ozone analysis from assimilation of posterior ozone observations in Fig. 3–7b), indicating some time decorrelation in the autocovariances.

The other tested limit in the EDAS during this work is on the assumption of an unbiased prior state intrinsic to the Kalman Filter equations. The EnKF was subjected to strong initial deviations in the temperature, winds and ozone forecast states with respect to the true state (Fig. 4–4), which was chosen to be a rare event of stratospheric sudden warming (SSW) self-generated in the IGCM-FASTOC model. With assimilation of stratospheric ozone observations, the initial forecast deviation at the central time of the SSW event was reduced over the course of a few data assimilation cycles (Fig. 4–5). This further confirms and demonstrates the ability of ensemble-derived ozone-dynamics error covariances to transfer information efficiently from the sparse ozone observations to the dynamical state of the model.

A few additional comments should be raised about the results obtained in this study. In most EDAS, the SPREAD of the ensemble is smaller than the RMSE. We systematically find the opposite in this study without imposing covariance inflation. An over-dispersive ($\text{SPREAD} > \text{RMSE}$) analysis ensemble is not prone to filter divergence, and therefore preferable than the contrary as it underestimates the accuracy of the model. The absence of model errors contributes

to the relatively low RMSE in the system. Also, we hypothesize that the reason for the larger SPREAD is a combination of the sparse observation network (Gottwald et al., 2011) and the effect of noisy cross covariances. In a sparsely observed system, the observations can not efficiently constrain some of the grid variables, particularly if the error covariances are noisy.

Throughout the study the focus was slightly biased towards the dynamical analysis of the system to the expense of the chemical state. For example, no diagnostics were included in this work about the interactive chemical species composing NO_y . Also, in the sensitivity study on the covariance localization of Chapter 2, the parameters were chosen based on the reduction of the error in total energy (Eqn. 2.11) which is composed of dynamical variables. Nonetheless, the chemical model state was considered as an integral part of the system and provided the possibility to constrain the dynamical model state with ozone observations. This work could be extended to include a more detailed analysis of the chemical state of the stratosphere following chemical or dynamical ensemble data assimilation. The other interactive chemical species forming NO_y could be assimilated as well to investigate their impact on the ozone analysis or even on the dynamical analysis.

This study has looked at many aspects of the chemical-dynamical coupling in an idealized ensemble data assimilation system. However, there are still many compelling problems that could be inquired. The most obvious ones are related to arguably the two most important choices that were made in setting up the experiments : the ensemble data assimilation filter and the type of localization. The

choice of the stochastic EnKF was made based on results from Lawson and Hansen (2004) stating its superior behavior with nonlinear prior distributions compared to the deterministic EnSRFs. Simple models were used for inter-comparisons between both types of filters. The IGCM-FASTOC could provide an interesting framework for further investigation on this aspect. Schur-product localization and local analysis are currently the most used methods to alleviate the problems incurred by using a limited amount of ensemble members. But the fact that they are tuned based on physical distance only is not appropriate for multivariate covariances and yields imbalances. In this study, the relatively high ensemble size and the sparse observing network allowed to relax the localization without incurring filter divergence. A relaxed localization minimizes the imbalances and permits an efficient propagation of information spatially and between variables, which is essential in a sparsely-observed region like the stratosphere. However, this is still a suboptimal procedure, particularly when the goal of the study is precisely to investigate information transfer through error covariances. Adaptive techniques of localization such as with “hierarchical filters” (Anderson, 2007b) or ensemble covariances raised to a power (ECO-RAP; Bishop and Hodyss, 2009a,b) would likely be more appropriate but require too much computational resources.

A minor but intriguing point raised during this work regards the spurious analysis increments obtained when sequential assimilation of observations by small batches following Houtekamer and Mitchell (2001) is applied to EnKS assimilation of posterior observations. This sequential technique uses the analysis from the assimilation of a batch of observations as background for the assimilation of the

next batch. While it has proved perfectly appropriate for synchronous EnKF assimilation both in this study and in previous scientific literature, the problematic behavior with the EnKS requires further analytical and applied inquiries.

The conclusions from ensemble data assimilation on our model with intermediate complexity stimulate continuing research with the apparatus on hand, as well as guidance for research with simpler to more complex numerical models. On the one hand, the logical next step is to attempt an imperfect-model OSSE with the same system by including model errors. That however requires to have a more complete observing network. Otherwise, techniques to compensate for underestimated forecast variance due to model errors, such as multiplicative inflation, may lead to unbounded error growth in regions poorly-constrained by the EDAS. With appropriate account of model errors in the EDAS, tests with state-of-the-art operational models could then be considered. This would allow to assess the effect of model errors on the quality of multivariate error covariances as witnessed in the perfect-model OSSEs from this study. On the other hand, investigation using toy models with simplified chemistry provide a practical and beneficial framework with which to study in depth the properties of multivariate chemical-dynamical data assimilation. An example is investigating the coupling when both chemistry and dynamics occur on similar timescales.

Appendix A: Kalman Filter and Extended Kalman Filter Equations

Kalman Filter Equations

We provide here details on the Kalman Filter equations for both the linear and the nonlinear model cases, as well as a guideline for the derivation of those equations. For simplicity, discrete-time (as opposed to continuous-time) equations are derived. The observation operator \mathcal{H} is assumed to be linear \mathbf{H} , allowing the use of linear algebra.

Let us start with estimating of the analysis state vector \mathbf{x}^a at time t_k by a linear combination of the forecast state vector \mathbf{x}^f and the observation vector \mathbf{y} , having respective weights $\tilde{\mathbf{L}}$ and $\tilde{\mathbf{K}}$:

$$\mathbf{x}_k^a = \tilde{\mathbf{L}}_k \mathbf{x}_k^f + \tilde{\mathbf{K}}_k \mathbf{y}_k \quad (5.1)$$

Define the true state \mathbf{x}^t of the atmosphere and its evolution, using an imperfect linear model ϕ and its error η :

$$\mathbf{x}_{k+1}^t = \phi_k \mathbf{x}_k^t + \eta_k \quad (5.2)$$

$$\mathbf{x}_k^f = \mathbf{x}_k^t + \mathbf{e}_k^f \quad (5.3)$$

$$\mathbf{x}_k^a = \mathbf{x}_k^t + \mathbf{e}_k^a \quad (5.4)$$

$$\mathbf{y}_k = \mathbf{H}_k \mathbf{x}_k^t + \varepsilon_k \quad (5.5)$$

$$\mathbf{x}_{k+1}^f = \phi_k \mathbf{x}_k^a \quad (5.6)$$

\mathbf{e}^a , \mathbf{e}^f and ε are respectively the analysis error, the forecast error and the observation error. The analysis error \mathbf{e}^a can be expressed as:

$$\mathbf{e}_k^a = \mathbf{x}_k^a - \mathbf{x}_k^t \quad (5.7)$$

$$= \tilde{\mathbf{L}}_k \mathbf{x}_k^f - \mathbf{x}_k^t + \tilde{\mathbf{K}}_k \mathbf{y}_k \quad (5.8)$$

$$= \tilde{\mathbf{L}}_k (\mathbf{x}_k^f - \mathbf{x}_k^t + \mathbf{x}_k^t) - \mathbf{x}_k^t + \tilde{\mathbf{K}}_k (\mathbf{H}_k \mathbf{x}_k^t + \varepsilon_k) \quad (5.9)$$

Since the forecast error term is $\mathbf{e}_k^f = \mathbf{x}_k^f - \mathbf{x}_k^t$, the analysis error becomes:

$$\mathbf{e}_k^a = \tilde{\mathbf{L}}_k (\mathbf{e}_k^f + \mathbf{x}_k^t) - \mathbf{x}_k^t + \tilde{\mathbf{K}}_k (\mathbf{H}_k \mathbf{x}_k^t + \varepsilon_k) \quad (5.10)$$

$$= \tilde{\mathbf{L}}_k \mathbf{e}_k^f + \tilde{\mathbf{L}}_k \mathbf{x}_k^t - \mathbf{x}_k^t + \tilde{\mathbf{K}}_k \mathbf{H}_k \mathbf{x}_k^t + \tilde{\mathbf{K}}_k \varepsilon_k \quad (5.11)$$

$$= (\tilde{\mathbf{L}}_k + \tilde{\mathbf{K}}_k \mathbf{H}_k - \mathbf{I}) \mathbf{x}_k^t + \tilde{\mathbf{L}}_k \mathbf{e}_k^f + \tilde{\mathbf{K}}_k \varepsilon_k \quad (5.12)$$

The expectation value of \mathbf{e}_k^a is:

$$\langle \mathbf{e}_k^a \rangle = (\tilde{\mathbf{L}}_k + \tilde{\mathbf{K}}_k \mathbf{H}_k - \mathbf{I}) \langle \mathbf{x}_k^t \rangle + \tilde{\mathbf{L}}_k \langle \mathbf{e}_k^f \rangle + \tilde{\mathbf{K}}_k \langle \varepsilon_k \rangle \quad (5.13)$$

Before proceeding forth, few assumptions need to be made :

- (i) the forecast errors are assumed to be unbiased $\langle \mathbf{e}_k^f \rangle = 0$.
- (ii) The observation errors are also assumed unbiased $\langle \varepsilon_k \rangle = 0$.

As the true state is obviously unbiased, for the analysis errors to be unbiased we need:

$$\tilde{\mathbf{L}}_k + \tilde{\mathbf{K}}_k \mathbf{H}_k - \mathbf{I} = 0 \quad (5.14)$$

thus

$$\tilde{\mathbf{L}}_k = \mathbf{I} - \tilde{\mathbf{K}}_k \mathbf{H}_k \quad (5.15)$$

Substituting $\tilde{\mathbf{L}}_k$ in (5.1) permits to obtain the best linear unbiased analysis of the true state and its error:

$$\mathbf{x}_k^a = \mathbf{x}_k^f + \tilde{\mathbf{K}}_k(\mathbf{y}_k - \mathbf{H}_k\mathbf{x}_k^f) \quad (5.16)$$

$$\mathbf{e}_k^a = (\mathbf{I} - \tilde{\mathbf{K}}_k\mathbf{H}_k)\mathbf{e}_k^f + \tilde{\mathbf{K}}_k\varepsilon_k \quad (5.17)$$

The analysis is unbiased so the first moment of the analysis is zero, but the second-moment error statistic, the analysis error covariance, is :

$$\begin{aligned} \mathbf{P}_k^a &= \langle (\mathbf{e}_k^a)(\mathbf{e}_k^a)^\top \rangle \\ &= \langle ((\mathbf{I} - \tilde{\mathbf{K}}_k\mathbf{H}_k)\mathbf{e}_k^f + \tilde{\mathbf{K}}_k\varepsilon_k)((\mathbf{I} - \tilde{\mathbf{K}}_k\mathbf{H}_k)\mathbf{e}_k^f + \tilde{\mathbf{K}}_k\varepsilon_k)^\top \rangle \\ &= (\mathbf{I} - \tilde{\mathbf{K}}_k\mathbf{H}_k) \langle (\mathbf{e}_k^f)(\mathbf{e}_k^f)^\top \rangle (\mathbf{I} - \tilde{\mathbf{K}}_k\mathbf{H}_k)^\top + (\mathbf{I} - \tilde{\mathbf{K}}_k\mathbf{H}_k) \langle (\mathbf{e}_k^f)(\varepsilon_k)^\top \rangle \tilde{\mathbf{K}}_k^\top \\ &\quad + \tilde{\mathbf{K}}_k \langle (\varepsilon_k)(\mathbf{e}_k^f)^\top \rangle (\mathbf{I} - \tilde{\mathbf{K}}_k\mathbf{H}_k)^\top + \tilde{\mathbf{K}}_k \langle (\varepsilon_k)(\varepsilon_k)^\top \rangle \tilde{\mathbf{K}}_k^\top \end{aligned}$$

Assuming that the forecast and observation errors are uncorrelated $\langle \mathbf{e}_k^f \varepsilon_k^\top \rangle = \langle \varepsilon_k \mathbf{e}_k^f{}^\top \rangle = 0$, \mathbf{P}^a becomes :

$$\begin{aligned} \mathbf{P}_k^a &= (\mathbf{I} - \tilde{\mathbf{K}}_k\mathbf{H}_k) \langle (\mathbf{e}_k^f)(\mathbf{e}_k^f)^\top \rangle (\mathbf{I} - \tilde{\mathbf{K}}_k\mathbf{H}_k)^\top + \tilde{\mathbf{K}}_k \langle (\varepsilon_k)(\varepsilon_k)^\top \rangle \tilde{\mathbf{K}}_k^\top \\ \mathbf{P}_k^a &= (\mathbf{I} - \tilde{\mathbf{K}}_k\mathbf{H}_k)\mathbf{P}_k^f(\mathbf{I} - \tilde{\mathbf{K}}_k\mathbf{H}_k)^\top + \tilde{\mathbf{K}}_k\mathbf{R}_k\tilde{\mathbf{K}}_k^\top \end{aligned} \quad (5.18)$$

The analysis-error covariance matrix \mathbf{P}_k^a depends on the forecast-error covariance matrix \mathbf{P}_k^f and the observations-error covariance matrix \mathbf{R}_k :

$$\begin{aligned} \mathbf{P}_{k+1}^f &= \langle (\mathbf{e}_{k+1}^f)(\mathbf{e}_{k+1}^f)^\top \rangle \\ &= \langle (\mathbf{x}_{k+1}^f - \mathbf{x}_{k+1}^t)(\mathbf{x}_{k+1}^f - \mathbf{x}_{k+1}^t)^\top \rangle \\ &= \langle (\phi_k\mathbf{x}_k^a - \phi_k\mathbf{x}_k^t - \eta_k)(\phi_k\mathbf{x}_k^a - \phi_k\mathbf{x}_k^t - \eta_k)^\top \rangle \end{aligned}$$

$$\begin{aligned}
&= \langle (\phi_k(\mathbf{x}_k^a - \mathbf{x}_k^t) - \eta_k)(\phi_k(\mathbf{x}_k^a - \mathbf{x}_k^t) - \eta_k)^\top \rangle \\
&= \langle (\phi_k \mathbf{e}_k^a - \eta_k)(\phi_k \mathbf{e}_k^a - \eta_k)^\top \rangle \\
&= \phi_k \langle \mathbf{e}_k^a \mathbf{e}_k^{a\top} \rangle + \phi_k^\top \langle \eta_k \rangle - \phi_k \langle \mathbf{e}_k^a \eta_k^\top \rangle - \langle \eta_k \mathbf{e}_k^{a\top} \rangle + \langle \eta_k \eta_k^\top \rangle
\end{aligned}$$

$$\begin{aligned}
\mathbf{R}_k &= \langle (\varepsilon_k)(\varepsilon_k)^\top \rangle \\
&= \langle (\mathbf{y}_k - \mathbf{H}_k \mathbf{x}_k^t)(\mathbf{y}_k - \mathbf{H}_k \mathbf{x}_k^t)^\top \rangle
\end{aligned}$$

Assuming that model errors and analysis errors are uncorrelated $\langle \mathbf{e}_k^a \eta_k^\top \rangle = \langle \eta_k \mathbf{e}_k^{a\top} \rangle = 0$, the forecast-error covariance matrix is simplified to:

$$\mathbf{P}_{k+1}^f = \phi_k \mathbf{P}_k^a \phi_k^\top + \mathbf{Q}_k \quad (5.19)$$

where $\mathbf{Q} = \langle \eta \eta^\top \rangle$ is the model-error covariance matrix.

In the derivations above, the gain $\tilde{\mathbf{K}}_k$ is general. In the specific case of the Kalman filter it is defined as being the matrix for which the analysis error variance is minimized. To do so we minimize the analysis cost-function \mathcal{J}^a with respect to $\tilde{\mathbf{K}}$:

$$\begin{aligned}
0 &= \frac{d}{d\tilde{\mathbf{K}}_k}(\mathcal{J}_k^a) \\
&= \frac{d}{d\tilde{\mathbf{K}}_k}(E(|\mathbf{e}_k^a|_{\mathbf{S}_k}^2)) \\
&= \frac{d}{d\tilde{\mathbf{K}}_k}(\langle (\mathbf{e}_k^a) \mathbf{S}_k (\mathbf{e}_k^a)^\top \rangle) \\
&= \frac{d}{d\tilde{\mathbf{K}}_k}(\langle \text{Tr}(\mathbf{S}_k (\mathbf{e}_k^a) (\mathbf{e}_k^a)^\top) \rangle) \\
&= \frac{d}{d\tilde{\mathbf{K}}_k}(\text{Tr}(\mathbf{S}_k \mathbf{P}_k^a))
\end{aligned}$$

$$= \mathbf{S}_k[-2\mathbf{H}_k\mathbf{P}_k^f(\mathbf{I} - \tilde{\mathbf{K}}_k\mathbf{H}_k)^T + 2\mathbf{R}_k\tilde{\mathbf{K}}_k^T]$$

where \mathbf{S}_k is any positive-definite scaling matrix.

This gives the formula for the Kalman Gain \mathbf{K}_k :

$$\mathbf{K}_k = \mathbf{P}_k^f\mathbf{H}_k^T(\mathbf{H}_k\mathbf{P}_k^f\mathbf{H}_k^T + \mathbf{R}_k)^{-1} \quad (5.20)$$

Simplifying the analysis error covariance matrix:

$$\begin{aligned} \mathbf{P}_k^a &= (\mathbf{I} - \tilde{\mathbf{K}}_k\mathbf{H}_k)\mathbf{P}_k^f(\mathbf{I} - \tilde{\mathbf{K}}_k\mathbf{H}_k)^T + \tilde{\mathbf{K}}_k\mathbf{R}_k\tilde{\mathbf{K}}_k^T \\ &= \mathbf{P}_k^f - \mathbf{P}_k^f\tilde{\mathbf{K}}_k^T\mathbf{H}_k^T - \tilde{\mathbf{K}}_k\mathbf{H}_k\mathbf{P}_k^f + \tilde{\mathbf{K}}_k\mathbf{H}_k\mathbf{P}_k^f\tilde{\mathbf{K}}_k^T\mathbf{H}_k^T + \tilde{\mathbf{K}}_k\mathbf{R}_k\tilde{\mathbf{K}}_k^T \\ &= \mathbf{P}_k^f - \mathbf{P}_k^f\tilde{\mathbf{K}}_k^T\mathbf{H}_k^T - \tilde{\mathbf{K}}_k\mathbf{H}_k\mathbf{P}_k^f + \tilde{\mathbf{K}}_k(\mathbf{H}_k\mathbf{P}_k^f\mathbf{H}_k^T + \mathbf{R}_k)\tilde{\mathbf{K}}_k^T \end{aligned}$$

Substituting the general gain $\tilde{\mathbf{K}}_k$ by the Kalman Gain \mathbf{K}_k (5.20) for , we obtain the simpler version of Eq. (5.18):

$$\mathbf{P}_k^a = (\mathbf{I} - \mathbf{K}_k\mathbf{H}_k)\mathbf{P}_k^f \quad (5.21)$$

Extended Kalman Filter Equations

The previous section looked at the case with a linear model operator ϕ . In the case of a nonlinear model \mathcal{M} , the changes are first in the true state and forecast state (compare with (Eq. 5.6)):

$$\mathbf{x}_{k+1}^t = \mathcal{M}_k(\mathbf{x}_k^t) + \eta_k \quad (5.22)$$

$$\mathbf{x}_{k+1}^f = \mathcal{M}_k(\mathbf{x}_k^a) \quad (5.23)$$

Subtracting them:

$$\mathbf{x}_{k+1}^f - \mathbf{x}_{k+1}^t = \mathcal{M}_k(\mathbf{x}_k^a) - \mathcal{M}_k(\mathbf{x}_k^t) - \eta_k \quad (5.24)$$

$$\mathbf{e}_{k+1}^f = \mathcal{M}_k(\mathbf{x}_k^t + \mathbf{e}_k^a) - \mathcal{M}_k(\mathbf{x}_k^t) - \eta_k \quad (5.25)$$

Since the model is not linear anymore, we need to make a Taylor expansion of the first model term:

$$\begin{aligned} \mathcal{M}_k(x + \delta x) &= \mathcal{M}_k(x) + \frac{\partial \mathcal{M}_k(x)}{\partial x} \delta x + \frac{1}{2} \frac{\partial^2 \mathcal{M}_k(x)}{\partial \mathbf{x}^2} \delta x \delta x + \frac{1}{6} \frac{\partial^3 \mathcal{M}_k(x)}{\partial \mathbf{x}^3} \delta x \delta x \delta x \quad (5.26) \\ &= \mathcal{M}_k(x) + \mathbf{M}_k(\delta x) + \frac{1}{2} \mathbf{S}_k(\delta x \delta x) + \frac{1}{6} \mathbf{T}_k(\delta x \delta x \delta x) + \dots \quad (5.27) \end{aligned}$$

where we have introduced the Tangent Linear Model (TLM) \mathbf{M} to our nonlinear model \mathcal{M} and its second-order \mathbf{S} and third-order \mathbf{T} derivatives. Assuming weakly nonlinear dynamics, only the first-order term is retained so that :

$$\mathbf{e}_{k+1}^f \approx \mathcal{M}_k(\mathbf{x}_k^t) + \mathbf{M}_k \mathbf{e}_k^a - \mathcal{M}_k(\mathbf{x}_k^t) - \eta_k \quad (5.28)$$

$$= \mathbf{M}_k \mathbf{e}_k^a - \eta_k \quad (5.29)$$

In this case, we can find the forecast-error covariance matrix:

$$\mathbf{P}_{k+1}^f = \langle (\mathbf{e}_{k+1}^f)(\mathbf{e}_{k+1}^f)^T \rangle \quad (5.30)$$

$$= \mathbf{M}_k \mathbf{P}_k^a \mathbf{M}_k^T + \mathbf{Q}_k \quad (5.31)$$

Comparing this to (5.19), the linear model ϕ is replaced by the TLM \mathbf{M} in the nonlinear case, to propagate the error covariance matrix from time k to time $k + 1$. It however requires a closure scheme to keep the similarity with the linear model.

If higher-order terms are retained in the Taylor expansion :

$$\mathbf{e}_{k+1}^f = \mathbf{M}_k(\mathbf{e}_k^a) + \frac{1}{2}\mathbf{S}_k((\mathbf{e}_k^a)(\mathbf{e}_k^a)^T) + \frac{1}{6}\mathbf{T}_k((\mathbf{e}_k^a)(\mathbf{e}_k^a)(\mathbf{e}_k^a)) - \eta_k \quad (5.32)$$

and one can show that:

$$\begin{aligned} \mathbf{P}_{k+1}^f &= \mathbf{M}_k\mathbf{P}_k^a\mathbf{M}_k^T + \mathbf{Q}_k + \mathbf{M}_k\mathbf{\Theta}_k\mathbf{S}_k^T \\ &+ \frac{1}{4}\mathbf{S}_k\mathbf{\Gamma}_k\mathbf{S}_k^T + \frac{1}{3}\mathbf{M}_k\mathbf{\Gamma}_k\mathbf{T}_k^T + \frac{1}{4}\mathbf{S}_k\mathbf{P}_k^a\mathbf{P}_k^{aT}\mathbf{S}_k^T \\ &- \frac{1}{6}\mathbf{S}_k\mathbf{P}_k^a\mathbf{\Theta}_k^T\mathbf{T}_k^T - \frac{1}{36}\mathbf{T}_k\mathbf{\Theta}_k\mathbf{\Theta}_k^T\mathbf{T}_k^T + \dots \end{aligned}$$

where, analogous to the second statistical moment \mathbf{P} , $\mathbf{\Theta}$ and $\mathbf{\Gamma}$ are the third and fourth statistical moments.

Appendix B: Sparse Matrix Treatment

Sparse Background-Error Covariance Matrix Treatment

The sequential treatment of observations reduces the size of the observation-space matrices and therefore speeds up the analysis computation. Another approach is used in Chapter 4 to reduce the computational cost without any additional approximation. The localization of the error covariance matrix $\mathbf{P}(t_k, t_{k'})\mathbf{H}_{k'}^T$ by Schur product nullifies a certain proportion of its elements, thereby increasing its sparseness. This motivates the utilization of a sparse-matrix numerical treatment. The background-error covariance matrix must simply be sparse enough to benefit from this method.

We use the method named “Compressed Row Storage” (CRS, sometimes called “Compressed Sparse Row” CSR; Dongarra, 2000) applied on the large matrix:

$$\mathbf{P}(t_k, t_{k'})\mathbf{H}_{k'}^T \in \mathbb{R}^{n \times p}$$

where n is the total number of model state vector elements and p is the number of observations. The CRS technique reduces this $\mathbb{R}^{n \times p}$ into three vectors, with lengths of \tilde{n} , \tilde{n} and $n + 1$, respectively, where \tilde{n} is the number of non-zero values in the matrix. We define the sparseness in $\mathbf{P}(t_k, t_{k'})\mathbf{H}_{k'}^T$ as $S = 1 - \tilde{n}/(n \times p)$. The main vector lists the successive non-zero row entries of $\mathbf{P}(t_k, t_{k'})\mathbf{H}_{k'}^T$. The second vector holds the column indices of each non-zero values. The third vector gives, for each row of $\mathbf{P}(t_k, t_{k'})\mathbf{H}_{k'}^T$, the index of the value of the main vector corresponding

to the first non-zero value on this row. The third vector takes a length of $n + 1$ as by convention we add the value $\tilde{n} + 1$ after the n -th element. The total number of elements needed to represent $\mathbf{P}(t_k, t_{k'})\mathbf{H}_{k'}^T$ decreases from $n \times p$ in the matrix treatment to $n + 1 + 2 \times (1 - S) \times n \times p$ with the CRS method. This technique becomes beneficial for a $\mathbf{P}(t_k, t_{k'})\mathbf{H}_{k'}^T$ matrix more than half-sparse ($S > 0.5$).

Besides the reduced storage need and smaller amount of arithmetic operations, the CRS method allows efficient parallel matrix-vector multiplications. In particular, it allows to efficiently parallelize the product between $\mathbf{P}(t_k, t_{k'})\mathbf{H}_{k'}^T$ and the scaled innovations $\tilde{\mathbf{d}}_{k'} = (\mathbf{H}_{k'}\mathbf{P}^f(t_{k'})\mathbf{H}_{k'}^T + \mathbf{R}_{k'})^{-1} \mathbf{d}_{k'}$ in Eq. (3.1). In our case, utilization of the CRS method reduces the computational cost by a factor 7 and 8 for typical temperature and ozone assimilation, respectively, when compared to a parallelized matrix product method. Our sparseness is $S = 0.527$ and $S = 0.827$ respectively for the matrix $\mathbf{P}(t_k, t_{k'})\mathbf{H}_{k'}^T$. Nevertheless, the sequential assimilation of batches of 100 observations is still faster than the assimilation of all observations at once with the CRS technique by about 40% for temperature assimilation and 10% for ozone assimilation.

Appendix C: Index of Vectors and Parameters

Vectors, matrices and operators

\mathbf{x}^t	True state vector
\mathbf{x}^f	Forecast state vector
\mathbf{y}	Observation vector
\mathbf{x}^a	Analysis state vector
\mathcal{M}	Model operator
\mathbf{M}	Linearized model operator
\mathcal{H}	Model-to-observation space operator
\mathbf{H}	Linearized model-to-observation space operator
\mathbf{d}	Innovation vector
\mathbf{e}^f	Forecast error vector
\mathbf{P}^f	Forecast-error covariance matrix
\mathbf{e}^a	Analysis error vector
\mathbf{P}^a	Analysis-error covariance matrix
η	Model error vector
\mathbf{Q}	Model-error covariance matrix
ε	Model error vector
\mathbf{R}	Observation-error covariance matrix

Parameters

n	State vector size
p	Observation vector size
m	Ensemble size
C_h	Horizontal localization decorrelation length
C_v	Vertical localization decorrelation length
p_{\max}	maximum number of observations per batch
r_0	observation batch radius

References

- Anderson, J. L., 2001: An Ensemble Adjustment Kalman Filter for Data Assimilation. *Monthly Weather Review*, **129**, 2884–2903, doi:10.1175/1520-0493(2001)129<2884:AEAKFF>2.0.CO;2.
- Anderson, J. L., 2007a: An adaptive covariance inflation error correction algorithm for ensemble filters. *Tellus A*, **59 (2)**, 210–224, doi:10.1111/j.1600-0870.2006.00216.x.
- Anderson, J. L., 2007b: Exploring the need for localization in ensemble data assimilation using a hierarchical ensemble filter. *Physica D*, **230 (1-2)**, 99–111, doi:10.1016/j.physd.2006.02.011.
- Anderson, J. L. and S. L. Anderson, 1999: A Monte-Carlo Implementation of the Nonlinear Filtering Problem to Produce Ensemble Assimilations and Forecasts. *Monthly Weather Review*, **127**, 2741–2758, doi:10.1175/1520-0493(1999)127<2741:AMCIOT>2.0.CO;2.
- Andrews, D. G., J. R. Holton, and C. B. Leovy, 1987: *Middle Atmosphere Dynamics*. Academic Press.
- Andrews, D. G. and M. E. McIntyre, 1976: Planetary Waves in Horizontal and Vertical Shear: The Generalized Eliassen–Palm Relation and the Mean Zonal Acceleration. *Journal of the Atmospheric Sciences*, **33 (11)**, 2031–2048, doi:10.1175/1520-0469(1976)033<2031:PWIHAV>2.0.CO;2.

- Arellano Jr., A. F., P. G. Hess, D. P. Edwards, and D. Baumgardner, 2010: Constraints on black carbon aerosol distribution from Measurements of Pollution in the Troposphere (MOPITT) CO. *Geophysical Research Letters*, **37**, L17801, doi:10.1029/2010GL044416.
- Austin, J., et al., 2003: Uncertainties and assessments of chemistry-climate models of the stratosphere. *Atmospheric Chemistry and Physics*, **3**, 1–27, doi:10.5194/acp-3-1-2003.
- Baek, S.-J., B. R. Hunt, E. Kalnay, E. Ott, and I. Szunyogh, 2006: Local ensemble Kalman filtering in the presence of model bias. *Tellus A*, **58 (3)**, 293–306, doi:10.1111/j.1600-0870.2006.00178.x.
- Baier, F., T. Erbertseder, O. Morgenstern, M. Bittner, and G. Brasseur, 2005: Assimilation of MIPAS observations using a three-dimensional global chemistry-transport model. *Quarterly Journal of the Royal Meteorological Society*, **131 (613, Part C)**, 3529–3542, doi:10.1256/qj.05.92.
- Baldwin, M. P. and T. J. Dunkerton, 1999: Propagation of the Arctic Oscillation from the stratosphere to the troposphere. *Journal of Geophysical Research*, **104 (D24)**, 30 937–30 946, doi:10.1029/1999JD900445.
- Baldwin, M. P. and T. J. Dunkerton, 2001: Stratospheric harbingers of anomalous weather regimes. *Science.*, **294 (5542)**, 581–584, doi:10.1126/science.1063315.
- Baldwin, M. P., et al., 2001: The quasi-biennial oscillation. *Rev. Geophys.*, **39 (2)**, 179–229, doi:10.1029/1999RG000073.

- Bernath, P., et al., 2005: Atmospheric Chemistry Experiment (ACE): Mission overview. *Geophysical Research Letters*, **32**, L15S01, doi:10.1029/2005GL022386.
- Bishop, C. H., B. Etherton, and S. J. Majumdar, 2001: Adaptive Sampling with the Ensemble Transform Kalman Filter. Part I: Theoretical Aspects. *Monthly Weather Review*, **129**, 420–436, doi:10.1175/1520-0493(2001)129<0420:ASWTET>2.0.CO;2.
- Bishop, C. H. and D. Hodyss, 2007: Flow-adaptive moderation of spurious ensemble correlations and its use in ensemble-based data assimilation. *Quarterly Journal of the Royal Meteorological Society*, **133 (629, Part B)**, 2029–2044, doi:10.1002/qj.169.
- Bishop, C. H. and D. Hodyss, 2009a: Ensemble covariances adaptively localized with ECO-RAP. Part 1: tests on simple error models. *Tellus A*, **61 (1)**, 84–96, doi:10.1111/j.1600-0870.2008.00371.x.
- Bishop, C. H. and D. Hodyss, 2009b: Ensemble covariances adaptively localized with ECO-RAP. Part 2: a strategy for the atmosphere. *Tellus A*, **61 (1)**, 97–111, doi:10.1111/j.1600-0870.2008.00372.x.
- Bourqui, M. S., C. P. Taylor, and K. P. Shine, 2005: A new fast stratospheric ozone chemistry scheme in an intermediate general-circulation model. II: Applications to effects of future increases in greenhouse gases. *Quarterly Journal of the Royal Meteorological Society*, **131 (610, Part B)**, 2243–2261, doi:10.1256/qj.04.19.

- Boville, B. A., 1984: The influence of the polar night jet on the tropospheric circulation in a GCM. *Journal of the Atmospheric Sciences*, **41**, 1132–1142, doi:10.1175/1520-0469(1984)041<1132:TIOTPN>2.0.CO;2.
- Bowler, N. E. and K. R. Mylne, 2009: Ensemble transform Kalman filter perturbations for a regional ensemble prediction system. *Quarterly Journal of the Royal Meteorological Society*, **135 (640, Part A)**, 757–766, doi:10.1002/qj.404.
- Brasseur, G. P., X. Tie, P. J. Rasch, and F. Lefèvre, 1997: A three-dimensional simulation of the Antarctic ozone hole: Impact of anthropogenic chlorine on the lower stratosphere and upper troposphere. *Journal of Geophysical Research*, **102 (D7)**, 8909–8930, doi:10.1029/96JD03398.
- Brewer, A. W., 1949: Evidence for a world circulation provided by the measurements of helium and water vapour distribution in the stratosphere. *Quarterly Journal of the Royal Meteorological Society*, **75 (326)**, 351–363, doi:10.1002/qj.49707532603.
- Buehner, M., P. L. Houtekamer, C. Charette, H. L. Mitchell, and B. He, 2010a: Intercomparison of Variational Data Assimilation and the Ensemble Kalman Filter for Global Deterministic NWP. Part I: Description and Single-Observation Experiments. *Monthly Weather Review*, **138**, 1550–1566, doi:10.1175/2009MWR3157.1.
- Buehner, M., P. L. Houtekamer, C. Charette, H. L. Mitchell, and B. He, 2010b: Intercomparison of Variational Data Assimilation and the Ensemble Kalman Filter for Global Deterministic NWP. Part II: One-Month Experiments

- with Real Observations. *Monthly Weather Review*, **138**, 1567–1586, doi: 10.1175/2009MWR3158.1.
- Burgers, G., P. J. Van Leeuwen, and G. Evensen, 1998: Analysis Scheme in the Ensemble Kalman Filter. *Monthly Weather Review*, **126**, 1719–1724, doi: 10.1175/1520-0493(1998)126<1719:ASITEK>2.0.CO;2.
- Butchart, N., et al., 2011: Multimodel climate and variability of the stratosphere. *Journal of Geophysical Research*, **116**, D05 102, doi:10.1029/2010JD014995.
- Cariolle, D. and H. Teyssède, 2007: A revised linear ozone photochemistry parameterization for use in transport and general circulation models: multi-annual simulations. *Atmospheric Chemistry and Physics*, **7**, 2183–2196, doi: 10.5194/acp-7-2183-2007.
- Charlton, A. J., A. O'Neill, W. A. Lahoz, and A. C. Massacand, 2004: Sensitivity of tropospheric forecasts to stratospheric initial conditions. *Quarterly Journal of the Royal Meteorological Society*, **130 (600, Part A)**, 1771–1792, doi: 10.1256/qj.03.167.
- Charlton, A. J., A. O'Neill, W. A. Lahoz, and A. C. Massacand, 2005: The impact of the stratosphere on the troposphere during the southern hemisphere stratospheric sudden warming, September 2002. *Quarterly Journal of the Royal Meteorological Society*, **131 (609, Part A)**, 2171–2188, doi:10.1256/qj.04.43.
- Charlton, A. J., A. O'Neill, D. B. Stephenson, W. A. Lahoz, and M. P. Baldwin, 2003: Can knowledge of the state of the stratosphere be used to improve statistical forecasts of the troposphere? *Quarterly Journal of the Royal Meteorological Society*, **129 (595, Part B)**, 3205–3224, doi:10.1256/qj.02.232.

- Charlton, A. J. and L. M. Polvani, 2007: A New Look at Stratospheric Sudden Warmings. Part I: Climatology and Modeling Benchmarks. *Journal of Climate*, **20**, 449, doi:10.1175/JCLI3996.1.
- Charlton, A. J., et al., 2007: A new look at stratospheric sudden warmings. Part II: Evaluation of numerical model simulations. *Journal of Climate*, **20**, 470–488, doi:10.1175/JCLI3994.1.
- Charney, J. G. and P. G. Drazin, 1961: Propagation of planetary-scale disturbances from the lower into the upper atmosphere. *Journal of Geophysical Research*, **66 (1)**, 83–109, doi:10.1029/JZ066i001p00083.
- Charron, M., et al., 2012: The stratospheric extension of the Canadian global deterministic medium range weather forecasting system and its impact on tropospheric forecasts. *Monthly Weather Review*, doi:10.1175/MWR-D-11-00097.1.
- Chipperfield, M. P., B. V. Khattatov, and D. J. Lary, 2002: Sequential assimilation of stratospheric chemical observations in a three-dimensional model. *Journal of Geophysical Research*, **107 (D21)**, 4585, doi:10.1029/2002JD002110.
- Compo, G. P., et al., 2011: The Twentieth Century Reanalysis Project. *Quarterly Journal of the Royal Meteorological Society*, **137 (654, Part A)**, 1–28, doi: 10.1002/qj.776.
- Constantinescu, E. M., A. Sandu, T. Chai, and G. R. Carmichael, 2007: Ensemble-based chemical data assimilation. II: Covariance localization. *Quarterly Journal of the Royal Meteorological Society*, **133 (626, Part A)**, 1245–1256, doi: 10.1002/qj.77.

- Cortesi, U., et al., 2007: Geophysical validation of MIPAS-ENVISAT operational ozone data. *Atmospheric Chemistry and Physics*, **7**, 4807–4867, doi:10.5194/acp-7-4807-2007.
- Cosme, E., J. Verron, P. Brasseur, J. Blum, and D. Auroux, 2011: Smoothing Problems in a Bayesian Framework and Their Linear Gaussian Solutions. *Monthly Weather Review*, **140**, 683–695, doi:10.1175/MWR-D-10-05025.1.
- Coy, L., S. Eckermann, and K. Hoppel, 2009: Planetary Wave Breaking and Tropospheric Forcing as Seen in the Stratospheric Sudden Warming of 2006. *Journal of the Atmospheric Sciences*, **66**, 495–507, doi:10.1175/2008JAS2784.1.
- Daley, R., 1991: *Atmospheric Data Analysis*. Cambridge University Press.
- Daley, R., 1995: Estimating the Wind Field from Chemical Constituent Observations: Experiments with a One-Dimensional Extended Kalman Filter. *Monthly Weather Review*, **123**, 181–198, doi:10.1175/1520-0493(1995)123<0181:ETWFFC>2.0.CO;2.
- de Grandpré, J., R. Menard, Y. J. Rochon, C. Charette, S. Chabrilat, and A. Robichaud, 2009: Radiative Impact of Ozone on Temperature Predictability in a Coupled Chemistry-Dynamics Data Assimilation System. *Monthly Weather Review*, **137**, 679–692, doi:10.1175/2008MWR2572.1.
- Dee, D. P., 2005: Bias and data assimilation. *Quarterly Journal of the Royal Meteorological Society*, **131 (613, Part C)**, 3323–3343, doi:10.1256/qj.05.137.
- Dee, D. P., et al., 2011: The ERA-Interim reanalysis: configuration and performance of the data assimilation system. *Quarterly Journal of the Royal Meteorological Society*, **137 (656, Part A)**, 553–597, doi:10.1002/qj.828.

- Derber, J. C. and W.-S. Wu, 1998: The Use of TOVS Cloud-Cleared Radiances in the NCEP SSI Analysis System. *Monthly Weather Review*, **126**, 2287–2299, doi:10.1175/1520-0493(1998)126<2287:TUOTCC>2.0.CO;2.
- Desroziers, G., L. Berre, B. Chapnik, and P. Poli, 2005: Diagnosis of observation, background and analysis-error statistics in observation space. *Quarterly Journal of the Royal Meteorological Society*, **131 (613, Part C)**, 3385–3396, doi:10.1256/qj.05.108.
- Dessler, A. E., 2000: *The chemistry and physics of stratospheric ozone*. Academic Press.
- Dobson, G. M. B., D. N. Harrison, and J. Lawrence, 1929: Measurements of the amount of ozone in the earth's atmosphere and its relation to other geophysical conditions. *Proceedings of the Royal Society of London, Series A*, **122**, 456–486.
- Dongarra, J., 2000: Sparse matrix storage formats. *Templates for the Solution of Algebraic Eigenvalue Problems: A Practical Guide*, SIAM.
- Dragani, R., 2011: On the quality of the ERA-Interim ozone reanalyses: comparisons with satellite data. *Quarterly Journal of the Royal Meteorological Society*, **137 (658, Part A)**, 1312–1326, doi:10.1002/qj.821.
- EC : Environment Canada, cited 2012: Changes to Operational Runs. [Available online at http://collaboration.cmc.ec.gc.ca/cmc/cmci/product_guide/docs/changes_e.html].
- ECMWF : European Centre for Medium-Range Weather Forecasts, cited 2012: Atmospheric model identification numbers. [Available online at http://www.ecmwf.int/products/data/technical/model_id/index.html].

- Ehrendorfer, M. and R. M. Errico, 1995: Mesoscale predictability and the spectrum of optimal perturbations. *Journal of the Atmospheric Sciences*, **52**, 3475–3500, doi:10.1175/1520-0469(1995)052<3475:MPATSO>2.0.CO;2.
- Errera, Q., F. Daerden, S. Chabrillat, J. C. Lambert, W. A. Lahoz, S. Viscardy, S. Bonjean, and D. Fonteyn, 2008: 4D-Var assimilation of MIPAS chemical observations: ozone and nitrogen dioxide analyses. *Atmospheric Chemistry and Physics*, **8**, 6169–6187, doi:10.5194/acp-8-6169-2008.
- Evensen, G., 1992: Using the Extended Kalman Filter With a Multilayer Quasi-Geostrophic Ocean Model. *Journal of Geophysical Research*, **97 (C11)**, 17 905–17 924, doi:10.1029/92JC01972.
- Evensen, G., 1994: Sequential data assimilation with a nonlinear quasi-geostrophic model using Monte Carlo methods to forecast error statistics. *Journal of Geophysical Research*, **99 (C5)**, 10 143–10 162, doi:10.1029/94JC00572.
- Evensen, G., 2003: The Ensemble Kalman Filter: theoretical formulation and practical implementation. *Ocean Dynamics*, **53 (4)**, 343–367, doi:10.1007/s10236-003-0036-9.
- Evensen, G. and P. J. van Leeuwen, 2000: An ensemble Kalman smoother for nonlinear dynamics. *Monthly Weather Review*, **128**, 1852–1867, doi:10.1175/1520-0493(2000)128<1852:AEKSFN>2.0.CO;2.
- Eyring, V., et al., 2005: A Strategy for Process-Oriented Validation of Coupled Chemistry–Climate Models. *Bulletin of the American Meteorological Society*, **86 (8)**, 1117–1133, doi:10.1175/BAMS-86-8-1117.

- Eyring, V., et al., 2006: Assessment of temperature, trace species, and ozone in chemistry-climate model simulations of the recent past. *Journal of Geophysical Research*, **111**, D22 308, doi:10.1029/2006JD007327.
- Fish, D. J. and M. R. Burton, 1997: The effect of uncertainties in kinetic and photochemical data on model predictions of stratospheric ozone depletions. *Journal of Geophysical Research*, **102 (D21)**, 25 537–25 542, doi:10.1029/97JD01971.
- Fisher, M. and D. J. Lary, 1995: Lagrangian four-dimensional variational data assimilation of chemical species. *Quarterly Journal of the Royal Meteorological Society*, **121 (527, Part A)**, 1681–1704, doi:10.1002/qj.49712152709.
- Forster, P. M. d. F., M. Blackburn, R. Glover, and K. P. Shine, 2000: An examination of climate sensitivity for idealised climate change experiments in an intermediate general circulation model. *Climate Dynamics*, **16 (10-11)**, 833–849, doi:10.1007/s003820000083.
- Garand, L., S. Heillette, and M. Buehner, 2007: Interchannel Error Correlation Associated with AIRS Radiance Observations: Inference and Impact in Data Assimilation. *Journal of Applied Meteorology and Climatology*, **46**, 714–725, doi:10.1175/JAM2496.1.
- Gaspari, G. and S. Cohn, 1999: Construction of correlation functions in two and three dimensions. *Quarterly Journal of the Royal Meteorological Society*, **125 (554, Part B)**, 723–757, doi:10.1002/qj.49712555417.
- Geer, A. J., W. A. Lahoz, D. R. Jackson, D. Cariolle, and J. P. McCormack, 2007: Evaluation of linear ozone photochemistry parametrizations in a stratosphere-troposphere data assimilation system. *Atmospheric Chemistry and Physics*, **7**,

- 939–959, doi:10.5194/acp-7-939-2007.
- Gerber, E. P., et al., 2012: Assessing and Understanding the Impact of Stratospheric Dynamics and Variability on the Earth System. *Bulletin of the American Meteorological Society*, doi:10.1175/BAMS-D-11-00145.1.
- Giorgetta, M. A., E. Manzini, and E. Roeckner, 2002: Forcing of the quasi-biennial oscillation from a broad spectrum of atmospheric waves. *Geophysical Research Letters*, **29** (8), doi:10.1029/2002GL014756.
- GMAO : Global Modeling and Assimilation Office, cited 2012: GEOS-5 Atmospheric Assimilation Product. [Available online at <http://gmao.gsfc.nasa.gov/products>].
- Gottwald, G. A., L. Mitchell, and S. Reich, 2011: Controlling overestimation of error covariance in ensemble Kalman filters with sparse observations: A variance limiting Kalman filter. *Monthly Weather Review*, **139**, 2650–2667, doi:10.1175/2011MWR3557.1.
- Hall, T. M. and A. R. Plumb, 1994: Age as a diagnostic of stratospheric transport. *Journal of Geophysical Research*, **99** (D1), 1059–1070, doi:10.1029/93JD03192.
- Hamill, T. M., J. S. Whitaker, and C. Snyder, 2001: Distance-Dependent Filtering of Background Error Covariance Estimates in an Ensemble Kalman Filter. *Monthly Weather Review*, **129**, 2776–2790, doi:10.1175/1520-0493(2001)129<2776:DDFOBE>2.0.CO;2.
- Harada, Y., A. Goto, H. Hasegawa, N. Fujikawa, H. Naoe, and T. Hirooka, 2010: A Major Stratospheric Sudden Warming Event in January 2009. *Journal of the Atmospheric Sciences*, **67**, 2052–2069, doi:10.1175/2009JAS3320.1.

- Hoppel, K. W., N. L. Baker, L. Coy, S. D. Eckermann, J. P. McCormack, G. E. Nedoluha, and E. Siskind, 2008: Assimilation of stratospheric and mesospheric temperatures from MLS and SABER into a global NWP model. *Atmospheric Chemistry and Physics*, **8**, 6103–6116, doi:10.5194/acp-8-6103-2008.
- Hoskins, B. J. and A. J. Simmons, 1975: A multi-layer spectral model and the semi-implicit method. *Quarterly Journal of the Royal Meteorological Society*, **101** (429), 637–655, doi:10.1002/qj.49710142918.
- Houtekamer, P. L. and H. L. Mitchell, 1998: Data Assimilation Using an Ensemble Kalman Filter Technique. *Monthly Weather Review*, **126**, 796–811, doi:10.1175/1520-0493(1998)126<0796:DAUAEK>2.0.CO;2.
- Houtekamer, P. L. and H. L. Mitchell, 2001: A Sequential Ensemble Kalman Filter for Atmospheric Data Assimilation. *Monthly Weather Review*, **129**, 123–137, doi:10.1175/1520-0493(2001)129<0123:ASEKFF>2.0.CO;2.
- Houtekamer, P. L., H. L. Mitchell, and X. Deng, 2009: Model Error Representation in an Operational Ensemble Kalman Filter. *Monthly Weather Review*, **137**, 2126–2143, doi:10.1175/2008MWR2737.1.
- Houtekamer, P. L., H. L. Mitchell, G. Pellerin, M. Buehner, M. Charron, L. Spacek, and B. Hansen, 2005: Atmospheric Data Assimilation with an Ensemble Kalman Filter: Results with Real Observations. *Monthly Weather Review*, **133**, 604–620, doi:10.1175/MWR-2864.1.
- Hunt, B. R., E. J. Kostelich, and I. Szunyogh, 2007: Efficient data assimilation for spatiotemporal chaos: A local ensemble transform Kalman filter. *Physica D*, **230** (1-2), 112–126, doi:10.1016/j.physd.2006.11.008.

- Ide, K., P. Courtier, M. Ghil, and A. Lorenc, 1997: Unified notation for data assimilation: Operational, sequential and variational. *Journal of the Meteorological Society of Japan*, **75 (1B)**, 181–189.
- Jacob, D. J., 1999: *Introduction to Atmospheric Chemistry*. Princeton University Press.
- JMA : Japanese Meteorological Agency, cited 2012: Numerical Weather Prediction Activities. [Available online at <http://www.jma.go.jp/jma/en/Activities/nwp.html>].
- Kalnay, E., 2006: *Atmospheric Modeling, Data Assimilation and Predictability*. Cambridge University Press.
- Kazutoshi, O., et al., 2007: The JRA-25 Reanalysis. *Journal of the Meteorological Society of Japan. Ser. II*, **85 (3)**, 369–432, doi:10.2151/jmsj.85.369.
- Kepert, J. D., 2009: Covariance Localisation and Balance in an Ensemble Kalman Filter. *Quarterly Journal of the Royal Meteorological Society*, **135 (642, Part A)**, 1157–1176, doi:10.1002/qj.443.
- Khattatov, B. V., J.-F. Lamarque, L. V. Lyjak, R. Menard, P. Levelt, X. Tie, G. P. Brasseur, and J. C. Gille, 2000: Assimilation of satellite observations of long-lived chemical species in global chemistry transport models. *Journal of Geophysical Research*, **105 (D23)**, 29 135–29 144, doi:10.1029/2000JD900466.
- KMA : Korean Meteorological Administration, cited 2012: Weather Forecast — Numerical Weather Prediction. [Available online at http://web.kma.go.kr/eng/biz/forecast_02.jsp].

- Kodera, K., K. Yamazaki, K. Chiba, and K. Shibata, 1990: Downward propagation of upper stratospheric mean zonal wind perturbation to the troposphere. *Geophysical Research Letters*, **17 (9)**, 1263–1266, doi:10.1029/GL017i009p01263.
- Labitzke, K. G. and H. v. Loon, 1999: *The Stratosphere : Phenomena, History and Relevance*. Springer.
- Lahoz, W., B. Khattatov, and R. Ménard, 2010: *Data Assimilation : Making Sense of Observations*. Springer.
- Lahoz, W. A., R. Brugge, D. R. Jackson, S. Migliorini, R. Swinbank, D. Lary, and A. Lee, 2005: An observing system simulation experiment to evaluate the scientific merit of wind and ozone measurements from the future swift instrument. *Quarterly Journal of the Royal Meteorological Society*, **131 (606, Part B)**, 503–523, doi:10.1256/qj.03.109.
- Lahoz, W. A., Q. Errera, R. Swinbank, and D. Fonteyn, 2007: Data assimilation of stratospheric constituents: a review. *Atmospheric Chemistry and Physics*, **7**, 5745–5773, doi:10.5194/acp-7-5745-2007.
- Lawson, W. G. and J. A. Hansen, 2004: Implications of Stochastic and Deterministic Filters as Ensemble-Based Data Assimilation Methods in Varying Regimes of Error Growth. *Monthly Weather Review*, **132**, 1966–1981, doi:10.1175/1520-0493(2004)132<1966:IOSADF>2.0.CO;2.
- Lewis, J. M., S. Lakshmivarahan, and S. K. Dhall, 2006: *Dynamic Data Assimilation: A Least Squares Approach*. Cambridge University Press.
- Li, H., E. Kalnay, and T. Miyoshi, 2009: Simultaneous estimation of covariance inflation and observation errors within an ensemble Kalman filter. *Quarterly*

- Journal of the Royal Meteorological Society*, **135 (639, Part B)**, 523–533, doi:10.1002/qj.371.
- Liu, G., D. W. Tarasick, V. E. Fioletov, C. E. Sioris, and Y. J. Rochon, 2009: Ozone correlation lengths and measurement uncertainties from analysis of historical ozonesonde data in North America and Europe. *Journal of Geophysical Research*, **114 (D04112)**, doi:10.1029/2008JD010576.
- Liu, J. and E. Kalnay, 2007: Simple Doppler Wind Lidar adaptive observation experiments with 3D-Var and an ensemble Kalman filter in a global primitive equations model. *Geophysical Research Letters*, **34 (L19808)**, doi:10.1029/2007GL030707.
- Lorenc, A. C., 2003: The potential of the ensemble Kalman filter for NWP a comparison with 4D-Var. *Quarterly Journal of the Royal Meteorological Society*, **129 (595, Part B)**, 3183–3203, doi:10.1256/qj.02.132.
- Lorenz, E. N., 1963: Deterministic Nonperiodic Flow. *Monthly Weather Review*, **20**, 130–141, doi:10.1175/1520-0469(1963)020<0130:DNF>2.0.CO;2.
- Lupu, C., P. Gauthier, and S. Laroche, 2011: Evaluation of the Impact of Observations on Analyses in 3D and 4D-VAR Based on Information Content. *Monthly Weather Review*, **139**, 726–737, doi:10.1175/2010MWR3404.1.
- Manney, G. L., et al., 2007: Solar occultation satellite data and derived meteorological products: Sampling issues and comparisons with Aura Microwave Limb Sounder. *Journal of Geophysical Research*, **112 (D24S50)**, doi:10.1029/2007JD008709.

- Manney, G. L., et al., 2008: The evolution of the stratopause during the 2006 major warming: Satellite data and assimilated meteorological analyses. *Journal of Geophysical Research*, **113** (D11115), doi:10.1029/2007JD009097.
- Manney, G. L., et al., 2009: Aura Microwave Limb Sounder observations of dynamics and transport during the record-breaking 2009 Arctic stratospheric major warming. *Geophysical Research Letters*, **36** (L12815), doi:10.1029/2009GL038586.
- Manney, G. L., et al., 2011: Unprecedented Arctic ozone loss in 2011. *Nature*, **478**, doi:10.1038/nature10556.
- Martineau, P. and S.-W. Son, 2010: Quality of reanalysis data during stratospheric vortex weakening and intensification events. *Geophysical Research Letters*, **37** (L22801), doi:10.1029/2010GL045237.
- Masutani, M., et al., 2010: Observing system simulation experiments at the National Centers for Environmental Prediction. *Journal of Geophysical Research*, **115** (D07101), doi:10.1029/2009JD012528.
- Matsuno, T., 1971: A Dynamical Model of the Stratospheric Sudden Warming. *Journal of Atmospheric Sciences*, **28**, 1479–1494, doi:10.1175/1520-0469(1971)028<1479:ADMOTS>2.0.CO;2.
- McCormack, J. P., S. D. Eckermann, D. E. Siskind, and T. J. McGee, 2006: CHEM2D-OPP: A new linearized gas-phase ozone photochemistry parameterization for high-altitude NWP and climate models. *Atmospheric Chemistry and Physics*, **6**, 4943–4972, doi:10.5194/acp-6-4943-2006.

- McIntyre, M. E. and T. N. Palmer, 1984: The ‘surf zone’ in the stratosphere. *Journal of Atmospheric and Terrestrial Physics*, **46 (9)**, 825–849, doi:10.1016/0021-9169(84)90063-1.
- McLinden, C. A., S. C. Olsen, B. Hannegan, O. Wild, M. J. Prather, and J. Sundet, 2000: Stratospheric ozone in 3-D models: A simple chemistry and the cross-tropopause flux. *Journal of Geophysical Research*, **105 (D11)**, 14 653–14 665, doi:10.1029/2000JD900124.
- Ménard, R., S. E. Cohn, L.-P. Chang, and P. M. Lyster, 2000: Assimilation of Stratospheric Chemical Tracer Observations Using a Kalman Filter. Part I: Formulation. *Monthly Weather Review*, **128**, 2654–2671, doi:10.1175/1520-0493(2000)128<2654:AOSCTO>2.0.CO;2.
- Met Office : United Kingdom Meteorological Office, cited 2012: Met Office Numerical Weather Prediction models. [Available online at <http://www.metoffice.gov.uk/research/modelling-systems/unified-model/weather-forecasting>].
- Milewski, T. and M. S. Bourqui, 2011: Assimilation of stratospheric temperature and ozone with an Ensemble Kalman Filter in a Chemistry-Climate Model. *Monthly Weather Review*, **139**, 3389–3404, doi:10.1175/2011MWR3540.1.
- Mitchell, H. L., P. L. Houtekamer, and G. Pellerin, 2002: Ensemble Size, Balance, and Model-Error Representation in an Ensemble Kalman Filter. *Monthly Weather Review*, **130**, 2791–2808, doi:10.1175/1520-0493(2002)130<2791:ESBAME>2.0.CO;2.

- Miyazaki, K., 2009: Performance of a local ensemble transform Kalman filter for the analysis of atmospheric circulation and distribution of long-lived tracers under idealized conditions. *Journal of Geophysical Research*, **114** (D19304), doi:10.1029/2009JD011892.
- Miyoshi, T., Y. Sato, and T. Kadowaki, 2010: Ensemble Kalman Filter and 4D-Var Intercomparison with the Japanese Operational Global Analysis and Prediction System. *Monthly Weather Review*, **138**, 2846–2866, doi: 10.1175/2010MWR3209.1.
- Morcrette, J.-J., 1991: Radiation and cloud radiative properties in the European Centre for Medium Range Weather Forecasts forecasting system. *Journal of Geophysical Research*, **96** (D5), 9121–9132, doi:10.1029/89JD01597.
- NCEP : National Center for Environmental Prediction, cited 2012a: Global Ensemble Forecast System. [Available online at <http://www.emc.ncep.noaa.gov/GEFS>].
- NCEP : National Center for Environmental Prediction, cited 2012b: Global Forecast System. [Available online at <http://www.emc.ncep.noaa.gov/GFS>].
- Neef, L. J., S. M. Polavarapu, and T. G. Shepherd, 2006: Four-Dimensional Data Assimilation and Balanced Dynamics. *Journal of the Atmospheric Sciences*, **63**, 1840–1858, doi:10.1175/JAS3714.1.
- Nerger, L., W. Hiller, and J. Schröter, 2005: A comparison of error subspace Kalman filters. *Tellus A*, **57** (5), 715–735, doi:10.1111/j.1600-0870.2005.00141.x.
- Oke, P. R., P. Sakov, and S. P. Corney, 2007: Impacts of localisation in the EnKF and EnOI: experiments with a small model. *Ocean Dynamics*, **57** (1), 32–45,

- doi:10.1007/s10236-006-0088-8.
- Ott, E., et al., 2004: A local ensemble Kalman filter for atmospheric data assimilation. *Tellus A*, **56** (5), 415–428, doi:10.1111/j.1600-0870.2004.00076.x.
- Parrish, D. and J. Derber, 1992: The National Meteorological Centers spectral statistical interpolation analysis system. *Monthly Weather Review*, **120**, 1747–1763, doi:10.1175/1520-0493(1992)120<1747:TNMCSS>2.0.CO;2.
- Pawson, S., et al., 2000: The GCM-Reality Intercomparison Project for SPARC (GRIPS): Scientific Issues and Initial Results. *Bulletin of the American Meteorological Society*, **81** (4), 781–796, doi:10.1175/1520-0477(2000)081<0781:TGIPFS>2.3.CO;2.
- Pham, D. T., 2001: Stochastic Methods for Sequential Data Assimilation Methods in Strongly Nonlinear Systems. *Monthly Weather Review*, **129**, 1194–1207, doi:10.1175/1520-0493(2001)129<1194:SMFSDA>2.0.CO;2.
- Plumb, A. R., 1996: A “tropical pipe” model of stratospheric transport. *Journal of Geophysical Research*, **101** (D2), 3957–3972, doi:10.1029/95JD03002.
- Plumb, A. R. and M. K. W. Ko, 1992: INTERRELATIONSHIPS BETWEEN MIXING RATIOS OF LONG-LIVED STRATOSPHERIC CONSTITUENTS. *Journal of Geophysical Research*, **97** (D9), 10 145–10 156, doi:10.1029/92JD00450.
- Polavarapu, S., S. Ren, Y. Rochon, D. Sankey, N. Ek, J. Koshyk, and D. Tarasick, 2005a: Data Assimilation with the Canadian Middle Atmosphere Model. *Atmosphere-Ocean*, **43** (1), 77–100, doi:10.3137/ao.430105.

- Polavarapu, S., T. G. Shepherd, Y. Rochon, and S. Ren, 2005b: Some challenges of middle atmosphere data assimilation. *Quarterly Journal of the Royal Meteorological Society*, **131 (613, Part C)**, 3513–3527, doi:10.1256/qj.05.87.
- Rabitz, H. and O. Alis, 1999: General Foundations of High Dimensional Model Representations. *Journal of Mathematical Chemistry*, **25 (2-3)**, 197–233, doi:10.1023/A:1019188517934.
- Raspollini, P., et al., 2006: MIPAS level 2 operational analysis. *Atmospheric Chemistry and Physics*, **6**, 5605–5630, doi:10.5194/acp-6-5605-2006.
- Ren, S., S. Polavarapu, S. R. Beagley, Y. Nezlin, and Y. J. Rochon, 2011: The impact of gravity wave drag on mesospheric analyses of the 2006 stratospheric major warming. *Journal of Geophysical Research*, **116 (D19116)**, doi:10.1029/2011JD015943.
- Ren, S., S. M. Polavarapu, and T. G. Shepherd, 2008: Vertical propagation of information in a middle atmosphere data assimilation system by gravity-wave drag feedbacks. *Geophysical Research Letters*, **35 (L06804)**, doi:10.1029/2007GL032699.
- Rienecker, M. M., et al., 2008: The GEOS-5 Data Assimilation System - Documentation of Versions 5.0.1, 5.1.0, and 5.2.0. Technical Report Series on Global Modeling and Data Assimilation 27, Global Modeling and Assimilation Office of the National Aeronautics and Space Administration Goddard Space Flight Center.
- Rienecker, M. M., et al., 2011: MERRA: NASA's Modern-Era Retrospective Analysis for Research and Applications. *Journal of Climate*, **24**, 3624–3648,

- doi:10.1175/JCLI-D-11-00015.1.
- Riishøjgaard, L., 1998: A direct way of specifying flow-dependent background error correlations for meteorological analysis systems. *Tellus A*, **50** (1), 42–57, doi:10.1034/j.1600-0870.1998.00004.x.
- Riishøjgaard, L. P., 1996: On four-dimensional variational assimilation of ozone data in weather-prediction models. *Quarterly Journal of the Royal Meteorological Society*, **122** (535, Part A), 1545–1571, doi:10.1002/qj.49712253505.
- Roscoe, H., J. Shanklin, and S. Colwell, 2005: Has the Antarctic vortex split before 2002? *Journal of the Atmospheric Sciences*, **62** (3), 581–588, doi:10.1175/JAS-3331.1.
- Rowland, F. S. and M. J. Molina, 1975: Chlorofluoromethanes in the Environment. *Reviews of Geophysics*, **13** (1), 1–35, doi:10.1029/RG013i001p00001.
- Sacher, W. and P. Bartello, 2009: Sampling Errors in Ensemble Kalman Filtering. Part II: Application to a Barotropic Model. *Monthly Weather Review*, **137**, 1640–1654, doi:10.1175/2008MWR2685.1.
- Saha, S., et al., 2010: The NCEP Climate Forecast System Reanalysis. *Bulletin of the American Meteorological Society*, **91**, 1015–1057, doi:10.1175/2010BAMS3001.1.
- Sakov, P. and L. Bertino, 2010: Relation between two common localisation methods for the EnKF. *Computational Geosciences*, **15** (2), 225–237, doi:10.1007/s10596-010-9202-6.
- Sakov, P., G. Evensen, and L. Bertino, 2010: Asynchronous data assimilation with the EnKF. *Tellus A*, **62** (1), 24–29, doi:10.1111/j.1600-0870.2009.00417.x.

- Semane, N., et al., 2009: On the extraction of wind information from the assimilation of ozone profiles in Météo-France 4-D-Var operational NWP suite. *Atmospheric Chemistry and Physics*, **9**, 4855–4867, doi:10.5194/acp-9-4855-2009.
- Shaw, T. A. and T. G. Shepherd, 2008: Atmospheric science: Raising the roof. *Nature Geoscience*, **1**, 12–13, doi:10.1038/ngeo.2007.53.
- Shepherd, T. G., 2000: The middle atmosphere. *Journal of Atmospheric and Solar-Terrestrial Physics*, **62 (17-18)**, 1587–1601, doi:10.1016/S1364-6826(00)00114-0.
- Stajner, I., L. P. Riishøjgaard, and R. B. Rood, 2001: The GEOS ozone data assimilation system: Specification of error statistics. *Quarterly Journal of the Royal Meteorological Society*, **127 (573, Part A)**, 1069–1094, doi:10.1002/qj.49712757320.
- Szunyogh, I., E. J. Kostelich, G. Gyamarti, D. J. Patil, B. R. Hunt, E. Kalnay, E. Ott, and J. A. Yorke, 2005: Assessing a local ensemble Kalman filter: perfect model experiments with the National Centers for Environmental Prediction global model. *Tellus A*, **57**, 528–545, doi:10.1111/j.1600-0870.2005.00136.x.
- Szunyogh, I., E. J. Kostelich, G. Gyarmati, E. Kalnay, B. R. Hunt, E. Ott, E. Satterfield, and J. A. Yorke, 2008: A local ensemble Kalman filter data assimilation system for the NCEP global model. *Tellus A*, **60 (1)**, 113–130, doi:10.1111/j.1600-0870.2007.00274.x.
- Takemasa, M., S. Yamane, and T. Enomoto, 2007: The AFES-LETKF Experimental Ensemble Reanalysis: ALERA. *SOLA*, **3**, 45–48, doi:10.2151/sola.2007-012.

- Tan, D., et al., 2008: The ADM-Aeolus wind retrieval algorithms. *Tellus A*, **60 (2)**, doi:10.1111/j.1600-0870.2007.00285.x.
- Taylor, C. P. and M. S. Bourqui, 2005: A new fast stratospheric ozone chemistry scheme in an intermediate general-circulation model. I: Description and evaluation. *Quarterly Journal of the Royal Meteorological Society*, **131 (610, Part B)**, 2225–2242, doi:10.1256/qj.04.18.
- Tippett, M. K., J. L. Anderson, C. H. Bishop, T. M. Hamill, and J. S. Whitaker, 2003: Ensemble Square Root Filters. *Monthly Weather Review*, **131**, 1485–1490, doi:10.1175/1520-0493(2003)131<1485:ESRF>2.0.CO;2.
- Uppala, S. M., et al., 2005: The ERA-40 re-analysis. *Quarterly Journal of the Royal Meteorological Society*, **131 (612, Part B)**, 2961–3012, doi: 10.1256/qj.04.176.
- van Leeuwen, P. J., 1999: Comment on “Data Assimilation Using an Ensemble Kalman Filter Technique”. *Monthly Weather Review*, **127**, 1374–1377, doi: 10.1175/1520-0493(1999)127<1374:CODAUA>2.0.CO;2.
- van Leeuwen, P. J. and G. Evensen, 1996: Data Assimilation and Inverse Methods in Terms of a Probabilistic Formulation. *Monthly Weather Review*, **124**, 2898–2913, doi:10.1175/1520-0493(1996)124<2898:DAAIMI>2.0.CO;2.
- van Loon, M., P. J. H. Builtjes, and A. J. Segers, 2000: Data assimilation of ozone in the atmospheric transport chemistry model LOTOS. *Environmental Modelling & Software*, **15 (6-7)**, 603–609, doi:10.1016/S1364-8152(00)00048-7.
- Wargan, K., I. Stajner, S. Pawson, R. Rood, and W. Tan, 2005: Assimilation of ozone data from the Michelson Interferometer for Passive Atmospheric Sounding.

- Quarterly Journal of the Royal Meteorological Society* , **131 (611, Part A)**, 2713–2734, doi:10.1256/qj.04.184.
- Waugh, D. and T. Hall, 2002: Age of stratospheric air: Theory, observations, and models. *Reviews of Geophysics*, **40 (4)**, doi:10.1029/2000RG000101.
- Whitaker, J. S., G. P. Compo, and J.-N. Thépaut, 2009: A Comparison of Variational and Ensemble-Based Data Assimilation Systems for Reanalysis of Sparse Observations. *Monthly Weather Review*, **137**, 1991–1999, doi: 10.1175/2008MWR2781.1.
- Whitaker, J. S. and T. M. Hamill, 2002: Ensemble Data Assimilation without Perturbed Observations. *Monthly Weather Review*, **130**, 1913–1924, doi: 10.1175/1520-0493(2002)130<1913:EDAWPO>2.0.CO;2.
- Whitaker, J. S., T. M. Hamill, X. Wei, Y. Song, and Z. Toth, 2008: Ensemble Data Assimilation with the NCEP Global Forecasting System. *Monthly Weather Review*, **136**, 463–482, doi:10.1175/2007MWR2018.1.
- Winter, B. and M. S. Bourqui, 2011: The impact of surface temperature variability on the climate change response in the Northern Hemisphere polar vortex. *Geophysical Research Letters*, **38 (L08808)**, doi:10.1029/2011GL047011.
- Zagar, N., N. Gustafsson, and E. Kallen, 2004: Variational data assimilation in the tropics: The impact of a background-error constraint. *Quarterly Journal of the Royal Meteorological Society*, **130 (596, Part A)**, 103–125, doi: 10.1256/qj.03.13.